In presenting this dissertation in partial fulfillment of the requirements for an advanced degree at Idaho State University, I agree that the Library shall make it freely available for inspection. I further state that permission to download and/or print my dissertation for scholarly purposes may be granted by the Dean of the Graduate School, Dean of my academic division, or by the University Librarian. It is understood that any copying or publication of this dissertation for financial gain shall not be allowed without my written permission.

Signature _____

Date _____

The Impact of Interferences on Fission Signals at Higher Bremsstrahlung Energies

A dissertation presented

by

E. S. Cárdenas

to

The Department of Physics

in partial fulfillment of the requirements

for the degree of

Doctorate of Philosophy

in the subject of

Applied Physics

Idaho State University

Fall 2016

To the Graduate Faculty:

The members of the committee appointed to examine the dissertation of E. S. Cárdenas find it satisfactory and recommend that it be accepted.

Dr. A. W. Hunt,
Major Advisor

Dr. D. Dale,
Committee Member

Dr. G. Imel,
Committee Member

Dr. E. Tatar,
Committee Member

Dr. K. L. Reedy,
Graduate Faculty Representative

To Isabella Monet ... the wheels on my bus, I mean train

Acknowledgments

I would like to express my deepest gratitude and appreciation to my advisor, Dr. Alan Hunt. Thank you for generously giving me your time, knowledge, support, and patience. I am lucky to have had you as my advisor. It has been not only one of the greatest learning experiences of my life, but also super fun. You're the best.

I would also like to thank my committee members, Dr. Dan Dale, Dr. George Imel, Dr. Eddie Tatar, and Dr. Katherine Reedy. Thank you for your time and suggestions.

I am also lucky to have worked with many talented people including Mathew Kinlaw, Heather Siepel, Edward Reedy, Anna Hoskins, Benjamin Satterwhite, Adrianne Spilker, Jenna Deaven, and the IAC engineers. Thank you for your support and help with many challenges throughout my research effort. Thank you mostly for your friendship.

From the depths of my heart thank you to my family whose support has been immense.

Contents

List of Figures

List of Tables

Dissertation advisor
Dr. A. W. Hunt

Author
E. S. Cárdenas

The Impact of Interferences on Fission Signals at Higher Bremsstrahlung Energies

Abstract

Distinctive fission signals, utilizing bremsstrahlung photons to induce fission, have been rigorously studied with beam energies below 20 MeV. These signals incorporated delayed γ-rays and delayed neutrons that were identified by their energy and temporal characteristics. Requirements to enhance the detectable signal for stand-off detection motivated an increase in the bremsstrahlung beam energy. Utilizing the techniques developed at lower bremsstrahlung energies to construct fission signals, this research studies the reliability of fission signals and the impact of interferences in higher bremsstrahlung endpoint energy environments. The bremsstrahlung endpoint energies were increased from 15 to 45 MeV with 13 fissionable and 32 non-fissionable targets irradiated. At 15 MeV the fissionable signals were clearly discriminated, consistent with prior research. However, as the beam energy increased interferences from non-fissionable materials became evident. By 37.5 MeV, all non-fissionable targets interfered with the fission signals compromising fission signal reliability. In addition, the limited availability of production cross sections led to an examination of bremsstrahlung integral yields. Utilizing discrete γ-rays resulting from the decay products of interfering reactions, 7 measured integral yields were compared to the simulated bremsstrahlung integral yields. These comparisons provided information on the accuracy of a simulated signal in relation to a measured signal.

Chapter 1

Introduction

1.1 Introduction

Interest in fission detection began shortly after the discovery of fission with research indicating that the energy released could be used for constructive and destructive applications. The field of fission detection has continued to grow as a need to inventory, track, and account for fissioning materials has increased. Fission energy is distributed kinetically and in the form of particle release including neutrons and γ-rays that are emitted promptly and delayed in time. These prompt and delayed neutrons and γ-rays are signatures of fission events and frequently serve as subjects in fission detection research efforts [1–18].

Active inspection techniques utilizing interrogating sources to induce the fission process have grown over recent decades [1–32]. Active inspections increases the quantity of fission events over those generated spontaneously, consequently, active inspections are critical in conditions where shielding is significant, the detection time window is short, or in stand-off fission detection configurations. Although several sources of probing radiation have been implemented, bremsstrahlung beams are commonly used as the photons are highly penetrating and can be produced relatively easily over a wide range of energies. Moreover, the generation of fission signals has been successfully demonstrated utilizing bremsstrahlung photons as the probing source of radiation [11, 15–18, 23–25, 33–38].

These experiments utilize techniques to define fission signatures that were developed in prior experiments. The techniques developed in prior experiments were accomplished in near range detection schemes ($\leq$ 1 m from detector to sample) that implemented 7 to 22 MeV endpoint energy pulsed bremsstrahlung beams as the interrogating source of radiation [15, 17–19]. The signatures were defined by a delayed region that included neutrons and γ-rays emitted as a result of β-decay processes following fission events. The delayed neutrons were characterized by their emission time and delayed γ-rays by their emission time and energy. The absence of delayed neutrons and delayed γ-rays emitted from non-fissionable materials irradiated with bremsstrahlung beams below endpoint energies of ~16 MeV, provided non-fission signals that were statistically equivalent to the natural passive background. As a result, the fission signals were clearly recognized.

Although fission signals were reliably produced in these prior experiments, the research demonstrated that non-fission neutron signals produced in targets containing oxygen and non-fission γ-ray signals produced in targets containing beryllium increased beyond the natural passive background when targets were irradiated with bremsstrahlung beams with an endpoint energy above ~16 MeV. The yield in the oxygen containing samples increased following the β^- decay of ^{17}N produced as a result of the ^{18}O(γ,p) reaction (15.9 MeV reaction threshold) [39–41]. The emission of a neutron following the β^- decay of ^{17}N (95.1% branching ratio) augments the sample signal [40, 41]. The yield in beryllium containing samples was increased following the β^- decay of ^{8}Li produced as a result of the ^{9}Be(γ,p) reaction which has a 16.9 MeV reaction threshold [39–41]. Lithium-8 does not release discrete γ-rays following β^- decay, however, a 13.0 MeV β-particle is emitted [40, 41]. Interactions between the β-particle and nuclei on its trajectory result in bremsstrahlung radiation that increases the γ-ray yield. While small, the increase in yields, due to these reactions, indicated the potential for interferences that would increase the likelihood of detecting false positives, thereby, decreasing the accuracy of identifying fissionable materials. These interferences could arise if larger masses were irradiated at ~16 MeV and/or higher bremsstrahlung endpoint energies employed.

This research seeks to investigate potential interferences arising from utilizing

higher endpoint energy bremsstrahlung beams (20 MeV and beyond). Motivation to raise the bremsstrahlung endpoint energy is driven by an effort to increase fission detection capabilities at distances of 10's of meters and beyond [42–44]. As mentioned, stand-off fission detection (large source to sample and sample to detector distances) necessitates increasing radiation from the target to levels well above background thereby requiring an increase in the bremsstrahlung endpoint energy [42, 43]. An increase in the bremsstrahlung endpoint energy comes with an increase in the photon flux intensity. More photons lead to a greater likelihood of photon interaction in the sample. Boosting the bremsstrahlung endpoint energy also broadens the range of energies that overlap the giant dipole resonance (GDR) region associated with the photofission cross sections yielding a greater probability of fission events. In addition, at higher energies bremsstrahlung photons are emitted in a forward direction in line with the propagation of source electrons [45–49]. This property is illustrated in the beam spots of Figure 1.1 simulated with MCNP6 [49].

The simulated beam spots generated by 15 and 45 MeV source electrons were calculated by normalizing the bremsstrahlung fluence per bin to the maximum fluence produced. Therefore, the area of the contour plots, displayed in Figures 1.1a and 1.1b, with the maximum fluence are equivalent to one and are indicated in black. The photon fluence that results in between and including 90% to 100% of the maximum fluence are indicated by the red area with those from 75% to 90% of the maximum are indicated by yellow. Specifically, the ratio of photon fluence in relation to the maximum fluence follows the color displayed in the bar on the right of the plots. The plots show a broad dispersion of the fluence at 15 MeV observed in Figure 1.1a in comparison to a narrower distribution at 45 MeV observed in Figure 1.1b. The fluence produced from 45 MeV electrons has its greatest intensity towards the center of the beam as indicated by an intensity of 90% or greater of the maximum. This area comprises 40% of the beam. This compares to only 0.16% of the beam, indicated by the red and black areas in the graph of Figure 1.1a, produced from 15 MeV source electrons. At 15 MeV, the photon fluence with an intensity of 90% or greater of the maximum is insignificant and therefore barely visible in the contour graph. In addition, towards the edges of the beam spot the plots show that 22% of the beam

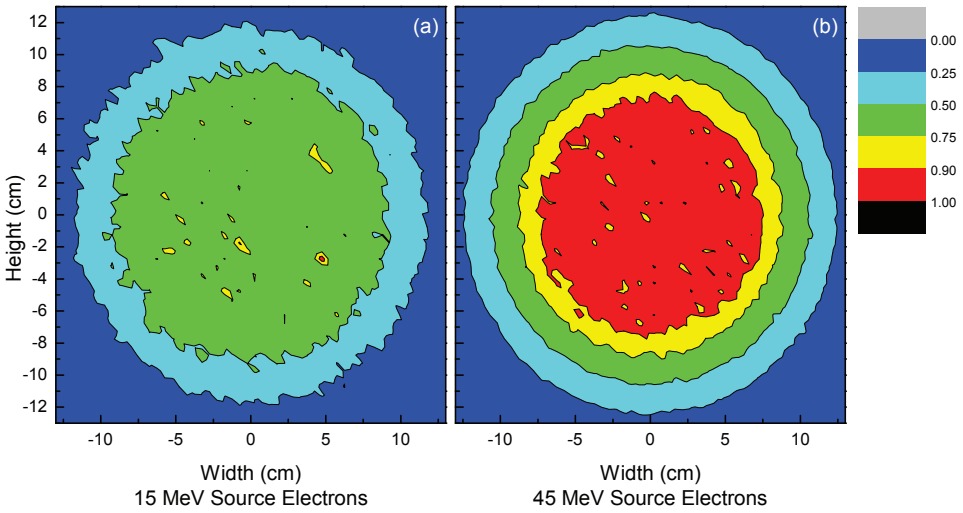

Figure 1.1: Contour plot of simulated bremsstrahlung beam spots located 50 m from tungsten radiator produced from 15 MeV (a) and 45 MeV (b) source electrons. Electrons emanating from a 5 mm diameter disk interact with a 0.22 cm thick tungsten (density of 19.3 g $\cdot$ cm^{-3}) radiator that sits 6.3 cm in front of and on axis to the source. Bremsstrahlung photons propagate 2.8 m towards a initial lead collimator (radius of 0.6 cm) and continue 1.8 m through a hole in a concrete and sand wall. The beam exits through a second lead collimator with a radius of 1.9 cm. Finally, bremsstrahlung photons are tallied over the surface of the target. Air fills the environment with all material specifications obtained from the Compendium of Material Composition Data for Radiation Transport Modeling. [49, 50]

has a fluence of 50% or less of the maximum for source electrons with an energy of 45 MeV as shown by the areas of blue, light blue, and gray; 45% make up the 50% or less of the maximum fluence at 15 MeV.

The gain in probability of photon interactions, fission events, and ultimate detection that comes with an elevated bremsstrahlung endpoint energy also results in a greater probability of producing interference reactions within a non-fissionable sample. As the bremsstrahlung endpoint energy increases beyond the GDR region associated with non-fissioning samples, multi-nucleon emissions within these samples are more probable and can lead to products far from the valley of stability. Reaction products

far from the valley of stability have more available energy for decay and an increased probability to produce neutrons and γ-rays within the delayed region mentioned previously. Regarding the reactions described above, $^{18}O(\gamma,p)^{17}N$ is unique in that the multi-nucleon producing reaction, (γ,2n), has a lower threshold energy than the (γ,p) reaction [51]. However, the $^{18}O(\gamma,2n)$ reaction leads to the stable ^{16}O isotope and therefore does not affect the magnitude of the signal. The GDR region for ^{18}O photonuclear reactions is ~17 MeV. Those photonuclear reactions falling below ~17 MeV are considered to be in the pygmy resonance region as indicated by J. G. Woodworth et al. [51]. Although $^{9}Be(\gamma,p)^{8}Li$ is not a multi-nucleon reaction, the threshold begins at the cusp of the GDR beginning at ~16 MeV [52]. The $^{9}Be(\gamma,n)$, $^{9}Be(\gamma,2n)$, and $^{9}Be(\gamma,np)$ reactions do not produce products with decay energies that increase the beryllium sample yield.

An increase in any particular sample yield, resulting from interfering reactions, is determined by multiple factors including the probability of reaction occurrence. The probability of reaction occurrence is measured through the production cross section. One approach to testing fission signature reliability at higher bremsstrahlung endpoint energies would be to simulate potential interfering reactions and measure the simulated signal against measured fission signals. Validation of the simulated signals could then be examined through experimentation. Another approach is to follow experiments with simulations. That approach was implemented here. In addition, the research found that production cross sections for many of the interfering reactions have not been measured experimentally. These findings ultimately led to measuring integral yields. Utilizing bremsstrahlung beams make calculating production cross sections difficult. However, measuring the integral yield is not as cumbersome. The measured integral yield is proportional to the integral of the production cross section weighted by the bremsstrahlung flux. Although a measured integral yield is not equivalent to a production cross section, it does give a good indication of the accuracy of a simulated signal. Simulations were conducted on a small set of samples to test the effectiveness of producing signals utilizing those production cross sections that were available in standard data libraries. As a result, the measured integral yields were compared with simulated bremsstrahlung integral yields. The bremsstrahlung

flux was simulated through a particular non-fissioning sample that was then used to calculate the bremsstrahlung integral yield. The measured integral yields were determined from counts composing γ-ray photopeaks that were generated from the decay of daughter products resulting from specific interfering reactions.

This dissertation discusses the physics, experimental techniques, and resulting analysis regarding fission detection in an active inspection environment employing high-energy pulsed bremsstrahlung beams. The effects of interferences on fission signal reliability is presented. Topics include:

- **The fission process in relation to signature development.** An explanation of the fission process as it pertains to prior fission signal development.
- **Increasing the bremsstrahlung endpoint energy and its importance in stand-off fission detection and potential interferences.** The effects of raising the electron energy to produce bremsstrahlung photons and the benefits to stand-off fission detection are discussed along with an explanation of how the energy push enhances the probability of producing fission signal interferences.
- **The process of choosing targets.** The process of target selection is detailed.
- **Uncertainty of detection.** A discussion on the critical decision level and the minimal detectable mass is provided including specifics pertaining to the passive and active components of the background. A description of detection limits in the dual γ-ray/neutron signal phase space is also presented.
- **Calculation of integral yields.** Measured and bremsstrahlung weighted integral yields are discussed.
- **The experimental setup.** A description of the experimental geometry and electronics is presented.
- **Data analysis.** This section goes through signature development, detection sensitivity, and results pertaining to the integral yields.

Chapter 2

Physics Considerations and Background Material

2.1 Fission Signal Development

Understanding the fundamental characteristics of the fission process is critical for the development of fission signatures. In an active inspection, the process is initiated as a nucleus absorbs energy beyond the fission barrier. Following absorption, there is a probability that the affected nucleus will split generating fragments along with the release of a significant amount of energy (~200 MeV) [19]. The probability of inducing photofission is greatest at the peak of the photonuclear giant dipole resonance (GDR). The GDR occurs in all nuclei across the periodic table and results in the oscillation of protons moving collectively against neutrons [53–60]. The collective motion is out-of-phase and can lead to splitting of the nucleus in fissioning isotopes. The energy from scission is distributed kinetically and in the form of particle emission; both prompt and delayed in time. The observation of all or a portion of this energy would serve as a signature to the fission event.

Within 10^{-12} s from the start of fission stimulation, an average of 2 to 3 prompt neutrons, totalling ~5 MeV, and 7 to 8 prompt γ-rays, totalling ~7 MeV, are emitted [10, 19, 61]. Excited fission fragments undergo an isomeric transition or stabilize through β^- decay. Neutrons and γ-rays that are preceded by the β-decay process are

emitted in time relative to the β half-life and are therefore termed "delayed". Delayed neutrons have half-lives that range from hundreds of milliseconds to 55.6 s while the range for delayed γ-rays continues from hundreds of milliseconds to years [62–66]. On average 7 delayed γ-rays are emitted per fission event with ~0.3%-5% of fission events emitting delayed neutrons [19, 61, 67, 68]. The emission yields vary with the fissioning compound, the resulting fission fragments, as well as with the type and magnitude of fission inducing energy. Nevertheless, the quantity of delayed γ-rays remains markedly larger than delayed neutrons per fission event [19, 61–65, 67, 69]. The techniques outlined here focus on detecting energy observed from delayed γ-rays and delayed neutrons.

Identifying delayed γ-rays and delayed neutrons from the vast number of γ-rays and neutrons detected was the primary challenge encountered in prior signal development [6, 15–18, 33–35, 37]. Following each bremsstrahlung pulse a large quantity of neutrons from both non-fissioning and fissioning materials was observed. After several milliseconds the initial burst of neutrons declined in both types of materials. However, in fissionable materials the decline was significantly less severe and was followed by a neutron rate that was much higher in magnitude than the rate observed in non-fissionable materials. Because the timescale of delayed neutron emission is essentially unique to the fission process, it was posited that the observed initial burst of neutrons was generated from (γ,n) reactions. The resulting neutrons scattered in the environment and were absorbed by the detectors. Graphs depicting neutron emission curves as a function of time are displayed in the results section and show a delayed neutron region that begins ~19 ms after the bremsstrahlung pulse. Therefore, the neutron fission signature is composed of neutrons emitted at and beyond 19 ms.

In contrast to delayed neutrons, various reactions can lead to γ-ray emissions on timescales similar to fission. However, active inspections yielded a significant number of γ-rays emitted with energies greater than ~3 MeV observed in the time frames examined. Furthermore, the γ-ray yield as a function of time from both non-fissioning and fissioning materials was initially large in a similar fashion to the neutron yield. The investigation revealed the production of (n,γ) reactions in the initial milliseconds after the bremsstrahlung pulse (as a result of the (γ,n) reactions discussed) [15, 17, 18].

In non-fissioning materials the (n,γ) reactions dominated the signal. Therefore, the delayed γ-ray region was defined as photons with energies $\geq$ 3 MeV and emitted in time following the initial die away from (n,γ) reactions. Evidence of the initial die away from alternative reactions is presented in the results section to follow and details the γ-ray delayed region starting ~29 ms after the bremsstrahlung pulse.

The fission signals were defined as the gross integrated yield, Y_g, constructed separately of delayed neutrons or delayed γ-rays. In the experiments presented here, typically the yields were composed of gross neutron or γ-ray counts, C_g, normalized to the average electron charge per pulse produced by the accelerator and the detector solid angle. With the normalization parameters combined and expressed as "N",

$$Y_g = \frac{C_g}{N}. \tag{2.1}$$

Furthermore, the gross yield included a portion of the signal produced from fission events, Y_s, and from background events, Y_{bck}, making

$$Y_g = Y_s + Y_{bck}. \tag{2.2}$$

In non-fissioning materials $Y_s \equiv 0$ leaving

$$Y_g = Y_{bck}. \tag{2.3}$$

2.2 Bremsstrahlung Energy Increase and Potential Interferences

The methods to construct the yields defined above and developed in prior near range experiments with bremsstrahlung beam energies that ranged from 7 to 22 MeV were utilized in the studies presented in these experiments [17, 18]. This research supports an initial investigation phase for stand-off fission detection that maintains the near range geometries (~1 m), but increases the spectrum of bremsstrahlung endpoint energies to include energies from 15 to 45 MeV. For stand-off detection, the bremsstrahlung energy is increased for three essential reasons: greater bremsstrahlung

photon production, larger overlap with the photofission cross sections, and photons that are peaked more in the forward direction.

An increase in bremsstrahlung photon production is obtained utilizing higher energy source electrons as demonstrated in the bremsstrahlung flux curves of Figure 2.1. Source electrons of 39 MeV produce an integrated photon flux (calculated to 19 MeV) that is ~7 times larger than the flux produced using 19 MeV source electrons. The simulated bremsstrahlung flux density was modeled with MCNPX version 2.7.0 and normalized to the average current produced in the measured data of 186 and 91μA for the 19 and 39 MeV electron energies respectively [70]. The reference equation for the bremsstrahlung cross section is found in the 1959 paper by Koch and Motz and is proportional to the square of the incident electron energy [45]. An increase in photon production enhances the probability of photon interaction within the target. In addition, the ^{235}U photofission cross section is overlaid on the graph. The figure shows that the larger endpoint energy bremsstrahlung beam produces more photons with energies in the range of the photofission cross section, thereby increasing the probability of generating fission.

Furthermore, higher energy bremsstrahlung beams produce photons that propagate closer inline with the direction of source electrons. Schiff describes this phenomena through the following equation which is proportional to the differential γ-ray intensity per unit solid angle,

$$\frac{d^3\Phi}{dEd\Omega dk} = \frac{16x^2E}{(x^2+1)^4E_o} - \frac{(E_o+E)^2}{(x^2+1)^2E_o^2} + \left(\frac{E_o^2+E^2}{(x^2+1)^2E_o^2} - \frac{4x^2E}{(x^2+1)^4E_o}\right)\ln M(x), \quad (2.4)$$

with

$$\frac{1}{M(x)} = \left(\frac{k\mu}{2E_oE}\right)^2 + \left(\frac{Z^{\frac{1}{3}}}{137(x^2+1)}\right)^2. \quad (2.5)$$

Both equations use the reduced angle defined as,

$$x = \frac{E_o\theta_o}{\mu}, \quad (2.6)$$

with E_o, E, μ, and k being the incident electron energy, the final electron energy, the electron rest energy, and the photon energy respectively [45,46]. The proton number is represented by Z. Using a reduced angle of 0.2 and a 14 MeV photon energy, the

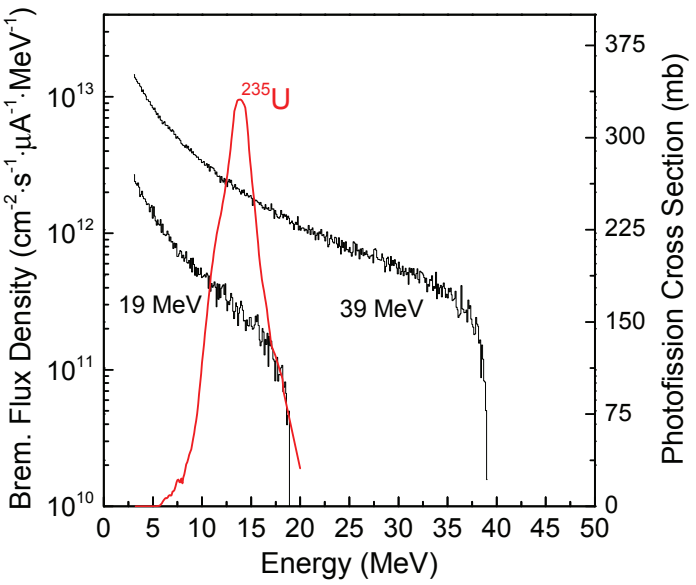

Figure 2.1: Bremsstrahlung flux density produced from 19 and 39 MeV (black) incident electron energies overlaid with the ^{235}U photofission cross section (red). Bremsstrahlung curves were simulated with MCNPX version 2.7.0. The photofission cross section was obtained from the ENDF/B-VII.1 database. [40, 41, 70]

γ-ray intensities are 6.246 and 4.407 for 39 and 19 MeV source electrons respectively. This reflects angles of 0.15° and 0.31° respectively for 39 and 19 MeV source electrons. In other words, a larger photon intensity is generated at a smaller angle from incidence for larger source electron energies. This corresponds to a narrower beam dispersion at higher bremsstrahlung endpoint energies providing a greater degree of accuracy on the target.

Although increasing the bremsstrahlung endpoint energy provides many benefits, it also pushes the range of photons with energy beyond the peak of the GDR. Energies absorbed beyond those associated with the peak of the GDR increase the probability of multi nucleon emissions. The resulting products may be farther from the valley of stability. The vast majority of products close to the valley of stability do not typically emit neutrons, high-energy γ-rays, or high-energy β-particles within the fission signature region. However, those far from the valley of stability may decay more energetically and are therefore more capable of producing γ-rays or neutrons

that have the potential to interfere with the fission signals. The exact magnitude of interrogating photon energy that produces potential interferences is not readily evident as the peak energy of the GDR in light nuclei is not consistent with mass number [56, 71]. As mentioned, two reactions produced decay emissions within the fission signature regions; ^{18}O(γ,p)^{17}N produced neutrons within the neutron fission signal range and ^{9}Be(γ,p)^{8}Li produced bremsstrahlung photons with energy and time characteristics defined by the γ-ray fission signals. These two reactions indicated a need for interference exploration.

2.3 Target Selection

The search for potential interfering reaction products was conducted by several researchers within the group. The Table of Isotopes and the Evaluated Nuclear Structure Data File (ENDF) databases were initially inspected to identify radioisotopes with decay products emitted on time scales and with energies that matched the γ-ray and neutron fission signature definitions [72, 73]. To satisfy the minimum delayed time window set by the fission signatures, radioisotopes that decay via neutron or γ-ray emissions and with half-lives greater than a value six times shorter than the time cutoff defining the regions were selected. This reflects half-lives of 3 and 5 ms for neutrons and γ-rays respectively. Radioisotopes decaying via β-particle emission were chosen in a similar fashion. Radioisotopes with half-lives $\geq$ 5 ms were selected satisfying the γ-ray fission signature definition as β-particles produce bremsstrahlung radiation through interactions with atomic nuclei. Although somewhat arbitrary, the cutoff for half-lives was chosen to ensure that radioisotopes with the potential to interfere were included, but those that would have little to no effect on the signatures were excluded. A value 6 times below the half-life reflects an activity of nearly an order of magnitude lower than the production at the onset of the bremsstrahlung pulse. The energy window was satisfied by selecting radioisotopes that decay via γ-ray or β-particle emission with energies $\geq$ 3 MeV.

The initial list included a large number of radioisotopes with many that could not be produced in naturally occurring non-fissioning isotopes through photonuclear

reactions. The list was reduced by selecting radioisotopes produced in naturally occurring non-fissionable materials and from the most probable reactions. The following 19 reactions were included:

- Products produced through a single particle type
  - ${}^{A}_{Z}\mathrm{X}(\gamma,\mathrm{n}){}^{A-1}_{Z}\mathrm{X}$
  - ${}^{A}_{Z}\mathrm{X}(\gamma,\mathrm{p}){}^{A-1}_{Z-1}\mathrm{X}$
  - ${}^{A}_{Z}\mathrm{X}(\gamma,2\mathrm{n}){}^{A-2}_{Z}\mathrm{X}$
  - ${}^{A}_{Z}\mathrm{X}(\gamma,2\mathrm{p}){}^{A-2}_{Z-2}\mathrm{X}$
  - ${}^{A}_{Z}\mathrm{X}(\gamma,3\mathrm{n}){}^{A-3}_{Z}\mathrm{X}$
- Product nuclei reduced by a neutron and a proton
  - ${}^{A}_{Z}\mathrm{X}(\gamma,\mathrm{d}){}^{A-2}_{Z-1}\mathrm{X}$ (lowest threshold reaction)
  - ${}^{A}_{Z}\mathrm{X}(\gamma,\mathrm{np}){}^{A-2}_{Z-1}\mathrm{X}$ (highest threshold reaction)
- Product nuclei reduced by 1 neutron and 2 protons
  - ${}^{A}_{Z}\mathrm{X}(\gamma,{}^{3}\mathrm{He}){}^{A-3}_{Z-2}\mathrm{X}$ (lowest threshold reaction)
  - ${}^{A}_{Z}\mathrm{X}(\gamma,\mathrm{dp}){}^{A-3}_{Z-2}\mathrm{X}$
  - ${}^{A}_{Z}\mathrm{X}(\gamma,\mathrm{n2p}){}^{A-3}_{Z-2}\mathrm{X}$ (highest threshold reaction)
- Product nuclei reduced by 2 neutrons and 1 proton
  - ${}^{A}_{Z}\mathrm{X}(\gamma,\mathrm{t}){}^{A-3}_{Z-1}\mathrm{X}$ (lowest threshold reaction)
  - ${}^{A}_{Z}\mathrm{X}(\gamma,\mathrm{dn}){}^{A-3}_{Z-1}\mathrm{X}$
  - ${}^{A}_{Z}\mathrm{X}(\gamma,\mathrm{p2n}){}^{A-3}_{Z-1}\mathrm{X}$ (highest threshold reaction)
- Product nuclei reduced by 2 neutrons and 2 protons (reactions are ordered from lowest to highest threshold energy)
  - ${}^{A}_{Z}\mathrm{X}(\gamma,{}^{4}\mathrm{He}){}^{A-4}_{Z-2}\mathrm{X}$ (lowest threshold reaction)
  - ${}^{A}_{Z}\mathrm{X}(\gamma,\mathrm{tp}){}^{A-4}_{Z-2}\mathrm{X}$

- ${}^{A}_{Z}\mathrm{X}(\gamma,\mathrm{n}^{3}\mathrm{He})^{A-4}_{Z-2}\mathrm{X}$
- ${}^{A}_{Z}\mathrm{X}(\gamma,2\mathrm{d})^{A-4}_{Z-2}\mathrm{X}$
- ${}^{A}_{Z}\mathrm{X}(\gamma,\mathrm{dpn})^{A-4}_{Z-2}\mathrm{X}$
- ${}^{A}_{Z}\mathrm{X}(\gamma,2\mathrm{p}2\mathrm{n})^{A-4}_{Z-2}\mathrm{X}$ (highest threshold reaction)

The list above shows several reaction categories that produce the same reaction product. The reaction itself is inconsequential apart from the parent and daughter isotope involved, however, the various reactions are noted to identify the threshold energies required to generate the reaction. Intersection of the initial radioisotope list with the reactions list was performed manually. The process produced three lists that included potential interferences generated by neutrons, γ-rays, and β-particles. While the lists that included neutron and γ-ray emissions contained reaction products with atomic mass numbers from 1 to 100, the list composed of radioisotopes that decay via β-particle emission was not fully constructed. The β-particle list was limited by incomplete decay information in available databases or by search functions that were not easy to perform.

The most concerning reactions were those that had the greatest likelihood to occur and those that had the potential to significantly affect the fission signatures. To easily identify the most concerning reactions, the final three lists included the following data:

- **Target isotope.** The naturally occurring parent isotope generating the reaction product.
- **Elemental abundance in the earth's crust.** The abundance is listed as a weight percentage.
- **Elemental abundance in the earth's atmosphere.** The abundance is listed as a volume percentage.
- **Isotopic abundance.** The abundance is listed as a number percentage.
- **Reaction** The induced reaction generating the concerning radioisotope.

- **Energy threshold.** The reaction threshold energy.
- **Reaction product.** The daughter product generated from the reaction.
- **Half-life.** The half-life is listed in seconds.
- **γ-ray Branch above 3 MeV.** The fraction of γ-rays that decay with energies above 3 MeV.
- **β-Particle branch above 3 MeV.** The fraction of β-particle emissions with decay energies above 3 MeV.
- **Neutron decay branch.** The fraction of decay via neutron emission.
- **β-decay branch.** The fraction of decay via β-particle emission.
- **Max β endpoint energy.** The maximum β-particle endpoint energy.
- **Tabulated cross section data.** The database listing the tabulated production cross section is indicated.
- **Experimental cross section data.** The list contains the name of the first author if the cross section was measured experimentally and available in the Experimental Nuclear Reaction Data (EXFOR) search tool.

Tables 2.1, 2.2, and 2.3 display the γ-ray, β-particle, and neutron compiled data respectively without the tabulated and experimental cross sections. Space requirements necessitated the division of tables, therefore, the tabulated and experimental cross sections are listed in Table 2.4. Only thirty of the reactions listed have production cross sections that were measured experimentally and listed in EXFOR. All of the reactions were listed in version 2014 of the TALYS-based Evaluated Nuclear Data Library (TENDL), however, if the cross section was available in the Evaluated Nuclear Data File version B-VII.1 (ENDF) the table reflects that inclusion. Approximately 54% of the reactions were evaluated and listed in ENDF/B-VII.1. The most concerning γ-ray potential interferences initially identified included the following 14 isotopes: ^{13}C, ^{14}N, ^{15}N, ^{18}O, ^{19}F, ^{28}Si, ^{35}Cl, ^{39}K, ^{40}Ar, ^{40}Ca, ^{58}Fe, ^{64}Ni, ^{64}Zn, and

^{96}Zr. Only 5 neutron reactions were identified with all target isotopes having the potential to interfere. The final list of reactions that decay via β-particle emission and shown here was compiled over the course of experiments performed throughout the study. Many of the reactions were revealed experimentally, as mentioned, the search was difficult to conduct. Therefore, beryllium was the only known target to decay via β-particle emission that was irradiated in the initial phase of high-energy experiments. In addition, a listing of parent isotope common uses is found in the appendix in Table B.1.

Table 2.1: Potential γ-Ray Reactions

Parent	**Reaction**	**Threshold**^{a} **(MeV)**	**Product**	**Half-life**^{*o} **(s)**	**Branch** $>$ **3 MeV**^{*o} **(%)**
^{27}Al	(γ,^{3}He)	23.72	^{24}Na	53989.2	7.484×10^{-2}
^{27}Al	(γ,3n)	41.40	^{24}Al	2.053	39.38
^{27}Al	(γ,3n)	41.79	^{24m}Al	0.130^{b,o}	0.6^{b,o}
^{36}Ar	(γ,t)	24.19	^{33}Cl	2.511	8.58×10^{-4}
^{36}Ar	(γ,n)	15.259	^{35}Ar	1.775	0.106
^{38}Ar	(γ,3n)	35.900	^{35}Ar	1.775	0.106
^{40}Ar	(γ,^{3}He)	23.07	^{37}S	303	94.36
^{75}As	(γ,3n)	29.02	^{72}As	93600	0.4863
^{79}Br	(γ,3n)	30.00	^{76}Br	58320	3.457
^{79}Br	(γ,n)	10.69	^{78}Br	387	4.488×10^{-4}
^{13}C	(γ,2p)	31.67	^{11}Be	13.81^{b,o}	10.85^{b,o}
^{13}C	(γ,p)	17.55	^{12}B	0.0202^{b,o}	100^{b,o}
^{40}Ca	(γ,np)	21.41	^{38}K	458.16	0.142
^{40}Ca	(γ,2n)	28.93	^{38}Ca	0.44	0.46431
^{46}Ca	(γ,^{3}He)	26.06	^{43}Ar	322.2	1.54
^{46}Ca	(γ,np)	22.72	^{44}K	1327.8	9.792
^{46}Ca	(γ,p)	13.81	^{45}K	1068.6	0.6714
^{48}Ca	(γ,^{3}He)	29.39	^{45}Ar	21.48	35.316
^{35}Cl	(γ,3n)	39.92	^{32}Cl	0.298^{b,o}	31.857^{b,o}
^{35}Cl	(γ,2n)	24.16	^{33}Cl	2.511	8.58×10^{-4}
^{35}Cl	(γ,n)	12.79	^{34m}Cl	1920	12.563
^{37}Cl	(γ,^{3}He)	22.15	^{34}P	12.43	0.249
^{53}Cr	(γ,p)	11.13	^{52}V	224.58	1.9×10^{-3}
^{54}Cr	(γ,np)	20.85	^{52}V	224.58	1.9×10^{-3}
^{63}Cu	(γ,n)	10.86	^{62}Cu	580.38	9.7×10^{-3}
^{19}F	(γ,^{3}He)	22.12	^{16}N	7.13	72.014
^{54}Fe	(γ,np)	20.91	^{52m}Mn	1266	0.02898
^{54}Fe	(γ,n)	13.38	^{53}Fe	510.6	0.0378
^{54}Fe	(γ,n)	16.42	^{53m}Fe	152.4	0.06
^{57}Fe	(γ,p)	10.56	^{56}Mn	9284.0	0.168079

Continued on next page. ^{o} [40],* [41],^{a} [39],^{b} [74]

Table 2.1 – Potential γ-Ray Reactions Continued

Parent	**Reaction**	**Threshold**[a] **(MeV)**	**Product**	**Half-life**[*o] **(s)**	**Branch > 3 MeV**[*o] **(%)**
^{58}Fe	(γ,np)	20.61	^{56}Mn	9284.0	0.168079
^{69}Ga	(γ,3n)	29.82	^{66}Ga	34164	13.36
^{70}Ge	(γ,3n)	32.13	^{67}Ge	1120.0[b,o]	0.69335[b,o]
^{73}Ge	(γ,p)	9.998	^{72}Ga	50760	0.03514
^{76}Ge	(γ,np)	20.53	^{74}Ga	487.2	3.640
^{39}K	(γ,3n)	40.63	^{36}K	0.342	21.917
^{39}K	(γ,2n)	25.16	^{37}K	1.226	0.019
^{39}K	(γ,n)	13.08	^{38}K	458.16	0.142
^{40}K	(γ,2n)	20.88	^{38}K	458.16	0.142
^{41}K	(γ,3n)	30.99	^{38}K	458.16	0.142
^{78}Kr	(γ,np)	19.25	^{76}Br	58320	3.457
^{80}Kr	(γ,np)	19.80	^{78}Br	387	4.488×10^{-4}
^{86}Kr	(γ,np)	20.85	^{84}Br	1906	14.67
^{24}Mg	(γ,3n)	49.11	^{21}Mg	0.122[b,o]	0.664[b,o]
^{25}Mg	(γ,p)	12.07	^{24}Na	53989	0.07484
^{26}Mg	(γ,np)	23.17	^{24}Na	53989	0.07484
^{92}Mo	(γ,n)	12.67	^{91}Mo	929.4	0.1540
^{94}Mo	(γ,3n)	30.42	^{91}Mo	929.4	0.1540
^{14}N	(γ,2p)	25.11	^{12}B	0.0202	1.229999
^{14}N	(γ,2n)	30.65	^{12}N	0.011	4.23
^{15}N	(γ,^{3}He)	28.23	^{12}B	0.0202	1.229999
^{15}N	(γ,2p)	31.07	^{13}B	0.0174[b,o]	7.78[b,o]
^{23}Na	(γ,^{3}He)	24.46	^{20}F	11.163	8.25×10^{-3}
^{23}Na	(γ,3n)	40.63	^{20}Na	0.446[b,o]	0.268[b,o]
^{23}Na	(γ,2p)	24.07	^{21}F	4.158	0.12376
^{21}Ne	(γ,2p)	23.66	^{19}O	26.88	0.08547
^{21}Ne	(γ,p)	13.01	^{20}F	11.163	8.25×10^{-3}
^{22}Ne	(γ,^{3}He)	26.31	^{19}O	26.88	0.08547
^{22}Ne	(γ,np)	23.38	^{20}F	11.163	8.25×10^{-3}
^{22}Ne	(γ,p)	15.27	^{21}F	4.158	0.12376
^{58}Ni	(γ,t)	21.15	^{55}Co	63108	5.25×10^{-3}
^{58}Ni	(γ,np)	19.55	^{56}Co	6698851	15.74
^{58}Ni	(γ,n)	12.22	^{57}Ni	128160	1.11E-2
^{64}Ni	(γ,^{3}He)	23.11	^{61}Fe	358.8	0.619
^{64}Ni	(γ,np)	21.03	^{62}Co	90	1.774
^{64}Ni	(γ,np)	21.06	^{62m}Co	834.6[b,o]	0.3[b,o]
^{16}O	(γ,2n)	28.92	^{14}O	70.6062	0.00211
^{16}O	(γ,3n)	52.16	^{13}O	0.00858	0.56
^{17}O	(γ,p)	13.79	^{16}N	7.13	72.014
^{17}O	(γ,2p)	25.28	^{15}C	2.449	63.3
^{18}O	(γ,np)	21.84	^{16}N	7.13	72.014
^{18}O	(γ,^{3}He)	25.61	^{15}C	2.449	63.3
^{18}O	(γ,^{3}He)	25.61	^{15}C	2.449	63.3

Continued on next page. [o] [40],[*] [41],[a] [39],[b] [74]

Table 2.1 – Potential γ-Ray Reactions Continued

Parent	**Reaction**	**Threshold**[a] **(MeV)**	**Product**	**Half-life**[*o] **(s)**	**Branch > 3 MeV**[*o] **(%)**
^{31}P	(γ,3n)	41.54	^{28}P	0.2703	31.6332
^{31}P	(γ,n)	12.31	^{30}P	149.88	8.3×10^{-3}
^{102}Pd	(γ,np)	17.70	^{100}Rh	74880	0.1371
^{85}Rb	(γ,3n)	30.20	^{82}Rb	75.45	2.184×10^{-3}
^{96}Ru	(γ,t)	17.43	^{93}Tc	9900	1.5888×10^{-2}
^{96}Ru	(γ,t)	17.82	^{93m}Tc	2610	1.4854
^{96}Ru	(γ,3n)	33.08	^{93}Ru	59.7	1.5181
^{96}Ru	(γ,np)	17.36	^{94m}Tc	3120	1.629
^{32}S	(γ,3n)	47.11	^{29}S	0.187[b,o]	35.4[b,o]
^{32}S	(γ,np)	21.18	^{30}P	149.88	8.3×10^{-4}
^{32}S	(γ,n)	15.05	^{31}S	2.572	0.042
^{33}S	(γ,2n)	23.70	^{31}S	2.572	0.042
^{34}S	(γ,3n)	35.12	^{31}S	2.572	0.042
^{36}S	(γ,np)	21.48	^{34}P	12.43	0.249
^{45}Sc	(γ,n)	11.33	^{44}Sc	14292	1.3986×10^{-3}
^{74}Se	(γ,3n)	33.29	^{71}Se	284.4	0.2375
^{74}Se	(γ,np)	19.35	^{72}As	93600	0.4863
^{80}Se	(γ,np)	20.31	^{78}As	5442	0.0648
^{82}Se	(γ,np)	20.74	^{80}As	15.2	0.126
^{82}Se	(γ,p)	12.35	^{81}As	33.3	0.036
^{29}Si	(γ,3n)	39.00	^{26}Si	2.234	4.9275×10^{-4}
^{84}Sr	(γ,np)	19.82	^{82}Rb	75.45	2.188×10^{-3}
^{46}Ti	(γ,3n)	39.04	^{43}Ti	0.509	0.0264
^{89}Y	(γ,3n)	32.65	^{86}Y	53064	0.33
^{64}Zn	(γ,np)	21.68	^{44}Sc	14292	1.3986×10^{-3}
^{64}Zn	(γ,np)	18.58	^{62}Cu	580.38	9.69×10^{-3}
^{64}Zn	(γ,n)	11.86	^{63}Zn	2308.2	5.494×10^{-3}
^{94}Zr	(γ,np)	17.82	^{92}Y	12744	4.17×10^{-3}
^{96}Zr	(γ,^{3}He)	20.29	^{93}Sr	445.38	0.187
^{96}Zr	(γ,np)	18.45	^{94}Y	1122	0.2615
^{96}Zr	(γ,p)	11.52	^{95}Y	618	8.646

Table 2.2: Potential β-Particle Reactions

Parent	**Reaction**	**Threshold**[a] **(MeV)**	**Product**	**Half-life**[*o] **(s)**	β **Branch**[*o] **(%)**	**Branch > 3 MeV**[*o] **(%)**	**Max** β **Endpoint**[*o] **(MeV)**
^{27}Al	(γ,^{3}He)	23.72	^{24}Na	53989.2	100	0.064	4.146778
^{27}Al	(γ,^{3}He)	24.18	^{24m}Na	0.02018	0.05	0.05	5.985807
^{27}Al	(γ,3n)	41.40	^{24}Al	2.053	100[b,o]	99.94[b,o]	9.755111[b,o]
^{27}Al	(γ,3n)	41.79	^{24m}Al	0.130	7	7.00	14.756

Continued on next page. [o] [40],[*] [41],[a] [39],[b] [74]

Table 2.2 Potential β-Particle Reactions Continued

Parent	**Reaction**	**Threshold**[a] **(MeV)**	**Product**	**Half-life**[*o] **(s)**	β **Branch**[*o] **(%)**	**Branch > 3 MeV**[*o] **(%)**	**Max** β **Endpoint**[*o] **(MeV)**
^{27}Al	(γ,2p)	22.43	^{25}Na	59.1	100	62.5	3.835
^{36}Ar	(γ,t)	24.19	^{33}Cl	2.511	100	99.555	5.5826
^{36}Ar	(γ,n)	15.259	^{35}Ar	1.775	100	99.749	5.9653
^{38}Ar	(γ,3n)	35.900	^{35}Ar	1.775	100	99.749	5.9653
^{40}Ar	(γ,p)	12.53	^{39}Cl	3336	100	100	6.1488
^{40}Ar	(γ,np)	20.61	^{38}Cl	2233.8	100	55.6	4.917
^{40}Ar	(γ,^{3}He)	23.07	^{37}S	303	100	5.6	4.86512
^{75}As	(γ,3n)	29.02	^{72}As	93600	100	85.7	4.356
^{10}B	(γ,2p)	23.50	^{8}Li	0.838	100	100	12.9650
^{11}B	(γ,^{3}He)	27.21	^{8}Li	0.838	100	100	12.9650
^{11}B	(γ,2p)	30.91	^{9}Li	0.1783	100	96	13.606
^{9}Be	(γ,p)	16.90	^{8}Li	0.838	100	100	12.9650
^{79}Br	(γ,3n)	22.15	^{76}Br	12.43	100	99.9	5.374
^{79}Br	(γ,n)	10.69	^{78}Br	387	100	86.4	3.574
^{13}C	(γ,2p)	31.67	^{11}Be	13.81[b,o]	100[b,o]	96.98[b,o]	11.5080[b,o]
^{13}C	(γ,p)	17.55	^{12}B	0.0202[b,o]	100[b,o]	100[b,o]	13.370[b,o]
^{40}Ca	(γ,n)	15.64	^{39}Ca	0.8596	100	100	6.5326
^{40}Ca	(γ,np)	21.41	^{38}K	458.16	100	99.899	5.91386
^{40}Ca	(γ,np)	21.54	^{38m}K	0.924	100	100	6.04426
^{40}Ca	(γ,2n)	28.93	^{38}Ca	0.44	100	100	99.3623
^{46}Ca	(γ,^{3}He)	26.06	^{43}Ar	322.2	100	50.56	4.565
^{46}Ca	(γ,np)	22.72	^{44}K	1327.8	100	37.8	5.6872
^{46}Ca	(γ,p)	13.81	^{45}K	1068.6	100	12.9	4.1965
^{48}Ca	(γ,^{3}He)	29.39	^{45}Ar	21.48	100	77.838	6.8448
^{35}Cl	(γ,3n)	39.92	^{32}Cl	0.298[b,o]	100[b,o]	100[b,o]	12.687[b,o]
^{35}Cl	(γ,2n)	24.16	^{33}Cl	2.511	100	99.56	5.5826
^{35}Cl	(γ,n)	12.79	^{34m}Cl	1920	44.6	28.49914	3.510076
^{37}Cl	(γ,^{3}He)	30.00	^{34}P	58320	100	39.25	4.963
^{63}Cu	(γ,n)	10.86	^{62}Cu	580.38	100	99.61	3.9589
^{19}F	(γ,^{3}He)	22.12	^{16}N	7.13	100	99.012	10.419
^{19}F	(γ,2p)	23.95	^{17}N	4.171	100	93.64	8.679
^{54}Fe	(γ,np)	20.91	^{52m}Mn	1266	98.25	96.285	3.655166
^{54}Fe	(γ,n)	13.38	^{53}Fe	510.6	100	98	3.7426
^{69}Ga	(γ,3n)	29.82	^{66}Ga	34164	100	51	5.175
^{70}Ge	(γ,3n)	32.13	^{67}Ge	1120[b,o]	100[b,o]	84.9[b,o]	4.223[b,o]
^{73}Ge	(γ,p)	9.998	^{72}Ga	50760	100	6.8	3.1631
^{76}Ge	(γ,np)	20.53	^{74}Ga	487.2	100	7.005	4.777
^{39}K	(γ,3n)	40.63	^{36}K	0.342	100	99.95	10.84381
^{39}K	(γ,2n)	25.16	^{37}K	1.226	100	100	6.1488
^{39}K	(γ,n)	13.08	^{38}K	458.16	100	99.90	5.91386
^{40}K	(γ,2n)	20.88	^{38}K	458.16	100	99.90	5.91386
^{41}K	(γ,3n)	30.99	^{38}K	458.16	100	99.90	5.91386

Continued on next page. [o] [40],* [41],[a] [39],[b] [74]

Table 2.2 Potential β-Particle Reactions Continued

Parent	**Reaction**	**Threshold**[a] **(MeV)**	**Product**	**Half-life**[*o] **(s)**	β **Branch**[*o] (%)	**Branch > 3 MeV**[*o] (%)	**Max** β **Endpoint**[*o] **(MeV)**
^{78}Kr	(γ,np)	19.25	^{76}Br	58320	100	39.25	4.963
^{80}Kr	(γ,np)	19.80	^{78}Br	387	100	86.4	3.574
^{86}Kr	(γ,np)	20.85	^{84}Br	1906	100	46.5	4.629
^{7}Li	(γ,p)	9.981	^{6}He	0.8067	100	100	3.5078
^{24}Mg	(γ,3n)	49.11	^{21}Mg	0.122[b,o]	100[b,o]	97.29[b,o]	13.098[b,o]
^{25}Mg	(γ,p)	12.07	^{24}Na	53989	100	0.064	4.1468
^{25}Mg	(γ,p)	12.54	^{24m}Na	0.02018	100	0.05	5.9858
^{26}Mg	(γ,np)	23.17	^{24}Na	53989	100	0.064	4.1468
^{26}Mg	(γ,np)	23.64	^{24m}Na	0.02018	100	0.05	5.9858
^{26}Mg	(γ,p)	14.15	^{25}Na	59.1	100	62.5	3.835
^{100}Mo	(γ,np)	18.11	^{98m}Nb	3078	100	4.4	3.1570
^{100}Mo	(γ,p)	11.23	^{99m}Nb	150	98	73.14	4.0042
^{92}Mo	(γ,n)	12.67	^{91}Mo	929.4	100	99.1405	4.4300
^{94}Mo	(γ,3n)	30.42	^{91}Mo	929.4	100	99.1405	4.4300
^{14}N	(γ,2p)	25.11	^{12}B	0.0202	100	100	13.3689
^{14}N	(γ,2n)	30.65	^{12}N	0.011	100	99.92	17.3381
^{15}N	(γ,^{3}He)	28.23	^{12}B	0.0202	100	99.92	17.3381
^{15}N	(γ,2p)	30.07	^{13}B	0.0174[b,o]	100[b,o]	100[b,o]	13.437[b,o]
^{23}Na	(γ,^{3}He)	24.46	^{20}F	11.163	100	99.9918	7.02453
^{23}Na	(γ,3n)	40.63	^{20}Na	0.446[b,o]	100[b,o]	100[b,o]	12.253[b,o]
^{23}Na	(γ,2p)	24.07	^{21}F	4.158	100	99.8	5.6842
^{21}Ne	(γ,2p)	23.66	^{19}O	26.88	100	99.89	4.8196
^{21}Ne	(γ,p)	13.01	^{20}F	11.163	100	99.9918	7.02453
^{22}Ne	(γ,^{3}He)	26.31	^{19}O	26.88	100	99.89	4.8196
^{22}Ne	(γ,np)	23.38	^{20}F	11.163	100	99.9918	7.02453
^{22}Ne	(γ,p)	15.27	^{21}F	4.158	100	99.8	5.6842
^{64}Ni	(γ,^{3}He)	23.11	^{61}Fe	358.8	100	4.688	3.978
^{64}Ni	(γ,np)	21.03	^{62}Co	90	100	93.85	5.315
^{16}O	(γ,2n)	28.92	^{14}O	70.6062	100	0.61	5.14304
^{17}O	(γ,p)	13.79	^{16}N	7.13	100	99.012	10.419
^{17}O	(γ,2p)	25.28	^{15}C	2.449	100	100	19.772
^{18}O	(γ,p)	15.95	^{17}N	4.171	100	93.64	8.679
^{18}O	(γ,np)	21.84	^{16}N	7.13	100	99.012	10.419
^{18}O	(γ,2p)	29.08	^{16}C	0.747[b,o]	100[b,o]	100[b,o]	7.887[b,o]
^{18}O	(γ,^{3}He)	25.61	^{15}C	2.449	100	100	12.451
^{31}P	(γ,3n)	41.54	^{28}P	0.2703	100	99.974	12.56472
^{31}P	(γ,n)	12.31	^{30}P	149.88	100	99.939	4.2324
^{102}Pd	(γ,np)	17.70	^{100}Rh	74880	100	1.2	3.6350
^{85}Rb	(γ,3n)	30.20	^{82}Rb	76.38	100	98.96	4.4020
^{96}Ru	(γ,3n)	33.08	^{93}Ru	59.7	100	98.24	6.391
^{96}Ru	(γ,np)	17.36	^{94m}Tc	2610	100	80.4	3.461
^{32}S	(γ,3n)	47.11	^{29}S	0.187[b,o]	100	99.96	5.3961

Continued on next page. [o] [40],[*] [41],[a] [39],[b] [74]

Table 2.2 Potential β-Particle Reactions Continued

Parent	**Reaction**	**Threshold**[a] **(MeV)**	**Product**	**Half-life**[*o] **(s)**	β **Branch**[*o] **(%)**	**Branch > 3 MeV**[*o] **(%)**	**Max** β **Endpoint**[*o] **(MeV)**
^{32}S	(γ,np)	21.18	^{30}P	149.88	100	99.939	4.2324
^{32}S	(γ,n)	15.05	^{31}S	2.572	100	99.96	5.3961
^{32}S	(γ,2n)	28.11	^{30}S	1.178	100	99.97	6.138
^{33}S	(γ,2n)	23.70	^{31}S	2.572	100	99.96	5.3961
^{33}S	(γ,3n)	36.76	^{30}S	1.178	100	99.97	6.138
^{34}S	(γ,3n)	35.12	^{31}S	2.572	100	99.96	5.3961
^{36}S	(γ,np)	21.48	^{34}P	12.43	100	99.9	5.374
^{74}Se	(γ,3n)	33.29	^{71}Se	284.4	100	95.23	4.749
^{74}Se	(γ,np)	19.35	^{72}As	93600	100	11.54	4.356
^{80}Se	(γ,np)	20.31	^{78}As	5442	100	50.5	4.2090
^{82}Se	(γ,np)	20.74	^{80}As	15.2	100	98.63	5.601
^{82}Se	(γ,p)	12.35	^{81}As	33.3	100	95.36	3.856
^{28}Si	(γ,2n)	30.51	^{26}Si	2.234	100	99.63	4.837695
^{28}Si	(γ,n)	17.19	^{27}Si	4.16	100	99.78	4.81236
^{29}Si	(γ,3n)	39.00	^{26}Si	2.234	100	99.63	4.837695
^{84}Sr	(γ,np)	19.82	^{82}Rb	75.45	100	98.96	4.402
^{46}Ti	(γ,3n)	39.04	^{43}Ti	0.509	100	100	6.867
^{89}Y	(γ,3n)	32.65	^{86}Y	53064	100	8	4.16324
^{64}Zn	(γ,3n)	33.88	^{61}Zn	89.1	100	94.06	5.638
^{64}Zn	(γ,np)	18.58	^{62}Cu	584.38	100	99.61	3.9589
^{64}Zn	(γ,n)	11.86	^{63}Zn	2308.2	100	84	3.3664
^{94}Zr	(γ,np)	17.82	^{92}Y	12744	100	85.7	3.642
^{96}Zr	(γ,^{3}He)	20.29	^{93}Sr	445.38	100	12.7	4.140
^{96}Zr	(γ,np)	18.45	^{94}Y	1122	100	89.83	4.919
^{96}Zr	(γ,p)	11.52	^{95}Y	618	100	66.8	4.450

Table 2.3: Potential Neutron Reactions

Parent	**Reaction**	**Threshold**[a] **(MeV)**	**Product**	**Half-life**[*o] **(s)**	**Neutron Branch**[*o] **(%)**
^{11}B	(γ,2p)	30.91	^{9}Li	0.1783	49.5
^{19}F	(γ,2p)	23.95	^{17}N	4.171	95.1
^{15}N	(γ,2p)	30.07	^{13}B	0.0174	0.28
^{18}O	(γ,p)	15.95	^{17}N	4.171	95.1
^{18}O	(γ,2p)	29.08	^{16}C	0.747[b,o]	98[b,o]

Table 2.4: Listed Cross Sections

Parent	**Reaction**	**Threshold**[a] **(MeV)**	**Product**	**Evaluated Cross Section**[o]	**Experimental Cross Section**[o],†	**Max Energy**[o] **(MeV)**
^{27}Al	(γ,^{3}He)	23.72	^{24}Na	ENDF/B-VII.1*		150
^{27}Al	(γ,3n)	41.40	^{24}Al	TENDL-2014+		200
^{27}Al	(γ,3n)	41.79	^{24}Al	TENDL-2014+		200
^{27}Al	(γ,2p)	22.43	^{25}Na	ENDF/B-VII.1*		150
^{36}Ar	(γ,t)	24.19	^{33}Cl	ENDF/B-VII.1*		140
^{36}Ar	(γ,n)	15.259	^{35}Ar	ENDF/B-VII.1*		140
^{38}Ar	(γ,3n)	35.900	^{35}Ar	ENDF/B-VII.1*		140
^{40}Ar	(γ,p)	12.53	^{39}Cl	ENDF/B-VII.1*		140
^{40}Ar	(γ,np)	20.61	^{38}Cl	ENDF/B-VII.1*	A. Veyssiere [71]	26.76
^{40}Ar	(γ,^{3}He)	23.07	^{37}S	TENDL-2014+		200
^{75}As	(γ,3n)	29.02	^{72}As	TENDL-2014+		200
^{10}B	(γ,2p)	23.50	^{8}Li	TENDL-2014+		200
^{11}B	(γ,^{3}He)	27.21	^{8}Li	TENDL-2014+		200
^{11}B	(γ,2p)	30.91	^{9}Li	TENDL-2014+		200
^{9}Be	(γ,p)	16.90	^{8}Li	ENDF/B-VII.1*	A. P. Komar [77]	30.5
^{79}Br	(γ,3n)	30.0	^{76}Br	TENDL-2014+		200
^{79}Br	(γ,n)	10.69	^{78}Br	TENDL-2014+	V. S. Bohinyuk [78]	20.0
^{13}C	(γ,2p)	31.67	^{11}Be	TENDL-2014+		200
^{13}C	(γ,p)	17.55	^{12}B	ENDF/B-VII.1*	D. Zubanov [79]	21.6
^{40}Ca	(γ,np)	21.41	^{38}K	ENDF/B-VII.1*	A. Veyssiere [71]	29.47
^{40}Ca	(γ,np)	21.54	^{38m}K	TENDL-2014+		200
^{40}Ca	(γ,2n)	28.93	^{38}Ca	ENDF/B-VII.1*		150
^{46}Ca	(γ,^{3}He)	26.06	^{43}Ar	TENDL-2014+		200
^{46}Ca	(γ,np)	22.72	^{44}K	ENDF/B-VII.1*		140
^{46}Ca	(γ,p)	13.81	^{45}K	ENDF/B-VII.1*		140
^{48}Ca	(γ,^{3}He)	29.39	^{45}Ar	TENDL-2014+		200
^{35}Cl	(γ,3n)	39.92	^{32}Cl	ENDF/B-VII.1*		140
^{35}Cl	(γ,2n)	24.16	^{33}Cl	ENDF/B-VII.1*		140
^{35}Cl	(γ,n)	12.79	^{34m}Cl	TENDL-2014+		200
^{37}Cl	(γ,^{3}He)	22.15	^{34}P	ENDF/B-VII.1*		140
^{53}Cr	(γ,p)	11.13	^{52}V	ENDF/B-VII.1*		140
^{54}Cr	(γ,np)	20.85	^{52}V	ENDF/B-VII.1*		140
^{63}Cu	(γ,n)	10.86	^{62}Cu	ENDF/B-VII.1*	C. Plaisir [80]	19.0
^{19}F	(γ,^{3}He)	22.12	^{16}N	TENDL-2014+		200
^{19}F	(γ,2p)	23.95	^{17}N	TENDL-2014+		200
^{54}Fe	(γ,np)	20.91	^{52m}Mn	TENDL-2014+	O. A. Bezshyyko [81]	43.6
^{54}Fe	(γ,n)	13.38	^{53}Fe	ENDF/B-VII.1*	S. S. Borodina [82]	40
^{54}Fe	(γ,n)	16.42	^{53m}Fe	TENDL-2014+		200
^{57}Fe	(γ,p)	10.56	^{56}Mn	ENDF/B-VII.1*		140
^{58}Fe	(γ,np)	20.61	^{56}Mn	ENDF/B-VII.1*		140
^{69}Ga	(γ,3n)	29.82	^{66}Ga	TENDL-2014+		200

Continued on next page. [o] [40],* [41],+ [75],† [76],[a] [39]

Table 2.4 Listed Cross Sections Continued

Parent	**Reaction**	**Threshold**[a] **(MeV)**	**Product**	**Evaluated Cross Section**[o]	**Experimental Cross Section**[o],†	**Max Energy**[o] **(MeV)**
^{70}Ge	(γ,3n)	32.13	^{67}Ge	ENDF/B-VII.1*		140
^{73}Ge	(γ,p)	9.998	^{72}Ga	ENDF/B-VII.1*		140
^{76}Ge	(γ,np)	20.53	^{74}Ga	ENDF/B-VII.1*	P. Carlos [83]	26.46
^{39}K	(γ,3n)	40.63	^{36}K	TENDL-2014+		200
^{39}K	(γ,2n)	25.16	^{37}K	TENDL-2014+		200
^{39}K	(γ,n)	13.08	^{38}K	TENDL-2014+	D. V. Webb [84]	30.5
^{40}K	(γ,2n)	20.88	^{38}K	TENDL-2014+		200
^{41}K	(γ,3n)	30.99	^{38}K	TENDL-2014+		200
^{78}Kr	(γ,np)	19.25	^{76}Br	TENDL-2014+		200
^{80}Kr	(γ,np)	19.80	^{78}Br	TENDL-2014+		200
^{86}Kr	(γ,np)	20.85	^{84}Br	TENDL-2014+		200
^{7}Li	(γ,p)	9.981	^{6}He	TENDL-2014+	L. A. Kul'Chitskiy [85]	29.3
^{24}Mg	(γ,3n)	49.11	^{21}Mg	ENDF/B-VII.1*		140
^{25}Mg	(γ,p)	12.07	^{24}Na	ENDF/B-VII.1*		140
^{26}Mg	(γ,np)	23.17	^{24}Na	ENDF/B-VII.1*	S. C. Fultz [86]	28.621
^{26}Mg	(γ,p)	14.15	^{25}Na	ENDF/B-VII.1*	B. S. Ishkhanov [87]	26.8
^{100}Mo	(γ,np)	18.11	^{98m}Nb	TENDL-2014+		200
^{100}M	(γ,p)	11.23	^{99m}Nb	TENDL-2014+		200
^{92}Mo	(γ,n)	12.67	^{91}Mo	ENDF/B-VII.1*	M. G. Davydov [88]	29.470
^{94}Mo	(γ,3n)	30.42	^{91}Mo	ENDF/B-VII.1*		140
^{14}N	(γ,2p)	25.11	^{12}B	ENDF/B-VII.1*		1.4×10^8
^{14}N	(γ,2n)	30.65	^{12}N	ENDF/B-VII.1*		1.4×10^8
^{15}N	(γ,^{3}He)	28.23	^{12}B	ENDF/B-VII.1*		140
^{15}N	(γ,2p)	30.07	^{13}B	ENDF/B-VII.1*		140
^{23}Na	(γ,^{3}He)	24.46	^{20}F	ENDF/B-VII.1*		140
^{23}Na	(γ,3n)	40.46	^{20}Na	ENDF/B-VII.1*		140
^{23}Na	(γ,2p)	24.07	^{21}F	ENDF/B-VII.1*		140
^{21}Ne	(γ,2p)	23.66	^{19}O	TENDL-2014+		200
^{21}Ne	(γ,p)	13.01	^{20}F	TENDL-2014+		200
^{22}Ne	(γ,^{3}He)	26.31	^{19}O	TENDL-2014+		200
^{22}Ne	(γ,np)	23.38	^{20}F	TENDL-2014+		200
^{22}Ne	(γ,p)	15.27	^{21}F	TENDL-2014+	V. V. Varlamov [59]	29.93
^{58}Ni	(γ,t)	21.15	^{55}Co	ENDF/B-VII.1*	S. C. Fultz [89]	33.517
^{58}Ni	(γ,np)	19.55	^{56}Co	ENDF/B-VII.1*	S. S. Borodina [82]	40
^{58}Ni	(γ,n)	12.22	^{57}Ni	ENDF/B-VII.1*	S. S. Borodina [82]	40
^{64}Ni	(γ,^{3}He)	23.11	^{61}Fe	TENDL-2014+		200
^{64}Ni	(γ,np)	21.03	^{62}Co	ENDF/B-VII.1*		140
^{64}Ni	(γ,np)	21.06	^{62m}Co	TENDL-2014+		200
^{16}O	(γ,2n)	28.92	^{14}O	ENDF/B-VII.1*	P. Carlos [90]	89
^{16}O	(γ,3n)	52.16	^{13}O	TENDL-2014+		200
^{17}O	(γ,p)	13.79	^{16}N	ENDF/B-VII.1*		140
^{17}O	(γ,2p)	25.28	^{15}C	ENDF/B-VII.1*		140

Continued on next page. [o] [40],* [41],+ [75],† [76],[a] [39]

Table 2.4 Listed Cross Sections Continued

Parent	**Reaction**	**Threshold**[a] **(MeV)**	**Product**	**Evaluated Cross Section**[o]	**Experimental Cross Section**[o],†	**Max Energy**[o] **(MeV)**
^{18}O	(γ,p)	15.95	^{17}N	ENDF/B-VII.1*	J.G.Woodworth [51]	41.834
^{18}O	(γ,np)	21.84	^{16}N	ENDF/B-VII.1*	K. G. McNeill [91]	43.5
^{18}O	(γ,2p)	29.08	^{16}C	TENDL-2014+		200
^{18}O	(γ,^{3}He)	25.61	^{15}C	TENDL-2014+		200
^{18}O	(γ,^{3}He)	25.61	^{15}C	TENDL-2014+		200
^{31}P	(γ,3n)	41.54	^{28}P	TENDL-2014+		200
^{31}P	(γ,n)	12.31	^{30}P	TENDL-2014+	A. Veyssiere [71]	28.65
^{102}Pd	(γ,np)	17.70	^{100}Rh	ENDF/B-VII.1*		140
^{85}Rb	(γ,3n)	30.20	^{82}Rb	TENDL-2014+		200
^{96}Ru	(γ,t)	17.43	^{93}Tc	TENDL-2014+		200
^{96}Ru	(γ,t)	17.82	^{93m}Tc	TENDL-2014+		200
^{96}Ru	(γ,3n)	33.08	^{93}Ru	TENDL-2014+		200
^{96}Ru	(γ,np)	17.36	^{94m}Tc	TENDL-2014+		200
^{32}S	(γ,3n)	47.11	^{29}S	ENDF/B-VII.1*		140
^{32}S	(γ,pn)	21.18	^{30}P	ENDF/B-VII.1*	A. Veyssiere [71]	32.18
^{32}S	(γ,2n)	28.11	^{30}S	ENDF/B-VII.1*	D. W. Anderson [92]	66.094
^{32}S	(γ,n)	15.05	^{31}S	ENDF/B-VII.1*	A. Veyssiere [71]	32.18
^{33}S	(γ,3n)	36.76	^{30}S	ENDF/B-VII.1*		140
^{33}S	(γ,2n)	23.70	^{31}S	ENDF/B-VII.1*		140
^{34}S	(γ,3n)	35.12	^{31}S	ENDF/B-VII.1*		140
^{36}S	(γ,np)	21.48	^{34}P	ENDF/B-VII.1*		140
^{45}Sc	(γ,n)	11.33	^{44}Sc	TENDL-2014+	A. Veyssiere [71]	28.11
^{74}Se	(γ,3n)	33.29	^{71}Se	TENDL-2014+		200
^{74}Se	(γ,np)	19.35	^{72}As	TENDL-2014+		200
^{80}Se	(γ,np)	20.31	^{78}As	TENDL-2014+		200
^{82}Se	(γ,np)	20.74	^{80}As	TENDL-2014+		200
^{82}Se	(γ,p)	12.35	^{81}As	TENDL-2014+		200
^{28}Si	(γ,n)	17.19	^{27}Si	ENDF/B-VII.1*	R. E. Pywell [93]	33.103
^{29}Si	(γ,3n)	39.00	^{26}Si	ENDF/B-VII.1*		140
^{84}Sr	(γ,np)	19.82	^{82}Rb	ENDF/B-VII.1*		140
^{46}Ti	(γ,3n)	39.04	^{43}Ti	ENDF/B-VII.1*		140
^{46}Ti	(γ,np)	21.68	^{44}Sc	ENDF/B-VII.1*		140
^{89}Y	(γ,3n)	32.65	^{86}Y	TENDL-2014+		200
^{64}Zn	(γ,3n)	33.88	^{61}Zn	ENDF/B-VII.1*		140
^{64}Zn	(γ,np)	18.58	^{62}Cu	ENDF/B-VII.1*	T. E. Rodrigues [94]	60
^{64}Zn	(γ,n)	11.86	^{63}Zn	ENDF/B-VII.1*	T. E. Rodrigues [94]	30
^{94}Zr	(γ,np)	17.82	^{92}Y	ENDF/B-VII.1*	V. V. Varlamov [95]	31
^{96}Zr	(γ,^{3}He)	20.29	^{93}Sr	TENDL-2014+		200
^{96}Zr	(γ,np)	18.45	^{94}Y	ENDF/B-VII.1*		140
^{96}Zr	(γ,p)	11.52	^{95}Y	ENDF/B-VII.1*		140

2.4 Signal Uncertainty and Detection Limits

Predicting the efficacy of a signal to indicate the presence of fissioning isotopes, in the absence of potential interferences, is essential. In this step, the probability that a signal is observed from a fissionable material is measured against a reference yield determined by the background signal. Restating the fission signatures, a neutron signal is composed of neutrons emitted at and beyond 19 ms from the end of each bremsstrahlung pulse until the next pulse. A γ-ray signature includes γ-rays with energies $\geq$ 3 MeV and emitted 29 ms and beyond each bremsstrahlung pulse until the next pulse. A single inspection produces the yield, displayed in equation 2.2, composed of neutrons or γ-rays characterized by the signature definitions and observed over the total irradiation time that encompasses a multitude of accelerator pulses. Figure 2.2a depicts the yield from a single inspection comparing a fission signal defined by $Y_s > 0$ to a signal without fissioning isotopes where $Y_s = 0$.

Due to the random nature of radioactive decay, the total number of counts associated with the yield fluctuates under multiple inspections performed with identical parameters. Assuming that the decaying nucleus is a constituent in a large population of nuclei that have a low probability of decaying, the distribution of the yield can be predicted by a Poisson distribution. A Poisson distribution can be estimated by a Gaussian distribution assuming the number of events counted is large, as is the case in these experiments. Figure 2.2b portrays a Gaussian and also shows the limiting mean, ψ_g, of the distribution. For yields solely representing the background, the uncertainty in the limiting mean can be lower in magnitude as multiple measurements can be performed with identical parameters or the observation time can be extended. The Greek letter, ψ, indicates that the limiting mean is found from a large number of measurements. Utilization of Greek letters to symbolize limiting means determined from a large number of measurements or from long observation times is continued throughout the remainder of this dissertation.

The net signal more clearly reflects the yields that are associated with fission. Subtracting out the background portion of the signal reduces the gross yield to the net yield, Y_n. Customarily, multiple observations or an extended observation of a

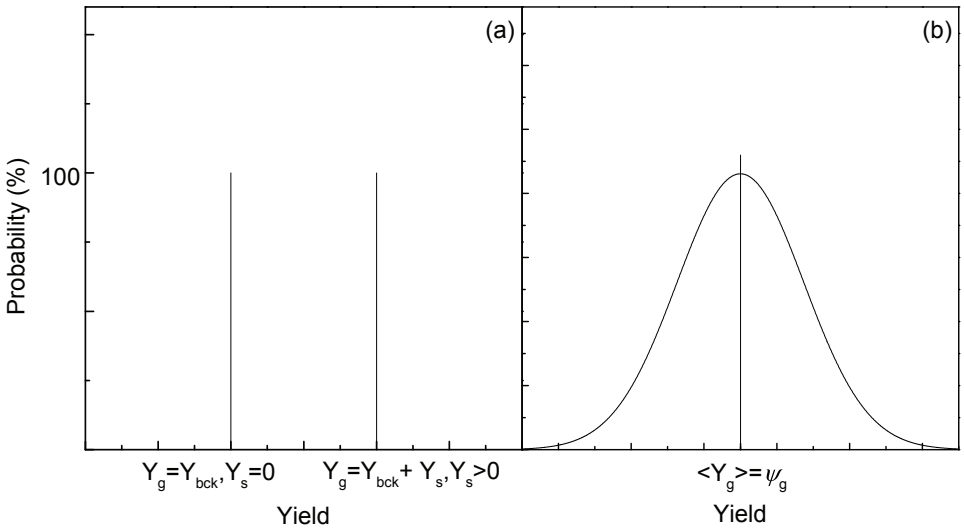

Figure 2.2: Probability distribution for a single inspection without uncertainty (a) and an inspection showing a distribution associated with uncertainty in measurement (b). The uncertainty produces a Gaussian distribution and the yields limiting mean, ψ_n.

no-target (blank) inspection represents the background yield. Therefore,

$$Y_n = Y_g - \psi_{bck}, \tag{2.7}$$

where ψ_{bck} is the limiting mean of the background yield.

Moreover, the background portion of the yield, Y_{bck}, can be divided further to reflect the portion associated with passive events, Y_{pbk}, and those that are induced by an active inspection, Y_{abk}. Therefore equation 2.7 becomes,

$$Y_n = Y_g - (\psi_{pbk} + \psi_{abk}). \tag{2.8}$$

The distinction between the active and passive background components is important because the relationship of the passive and active counts to the normalization parameters differs. The normalization parameters affect production of fission events. In other words, fission counts are proportional to the individual normalization parameters. For example, as the charge increases the number of photons goes up generating a probability of more fission events; as the irradiation time is lengthened, the number of fission events increases. Similarly, the active background is proportional to

the normalization parameters. In contrast, the passive background may or may not be proportional to the normalization parameters. For example, as the irradiation time increases the passive background increases, however, as the charge increases the passive background remains constant in the absence of statistical fluctuations. The active and passive components are vital in construction of the critical decision level.

2.4.1 Critical Decision Level

The critical decision level, L_c, is the magnitude of yield required to discern an inspection signal from a background signal. An inspection signal below L_c is obscured by the background and therefore undetectable. The critical decision level is determined from uncertainty properties related to the background distribution. Utilizing a Gaussian distribution, Figure 2.3 illustrates the relationship of L_c to the net background limiting mean, ψ_{bck}. The figure identifies the α region of the distribution that defines the false positive probability. The false positive probability incorrectly identifies a signal as detected. In other words, a non-fissionable material is incorrectly identified as containing fissioning isotopes. Therefore, $1-\alpha$ is the confidence level associated with predicting a signal as undetectable i.e. a background signal. The critical decision level is defined such that the probability of a single inspection $Y_n \geq L_c$ is $\leq \alpha$.

Using properties of the Gaussian integral and requiring its equality to α gives,

$$\int_{L_c}^{\infty} \frac{1}{s_{nc}\sqrt{2\pi}} e^{\frac{-Y_n^2}{2s_{nc}^2}} dY_n = \alpha, \tag{2.9}$$

where the standard deviation of the net single inspection yield is s_{nc}. Solving for L_c and using properties of error functions resolves,

$$L_c = \sqrt{2}\,\mathrm{erf}^{-1}(1-2\alpha)\; s_{nc}. \tag{2.10}$$

Going forward, the abscissa, $\sqrt{2}\,\mathrm{erf}^{-1}(1-2\alpha)$, is defined as k_α. The distribution width reflects uncertainty in the passive and active components. Utilizing the definition for the net yield defined in Equation 2.7 and standard error propagation rules the net variance becomes,

$$s_{nc}^2 = s_{gc}^2 + \sigma_{bck}^2, \tag{2.11}$$

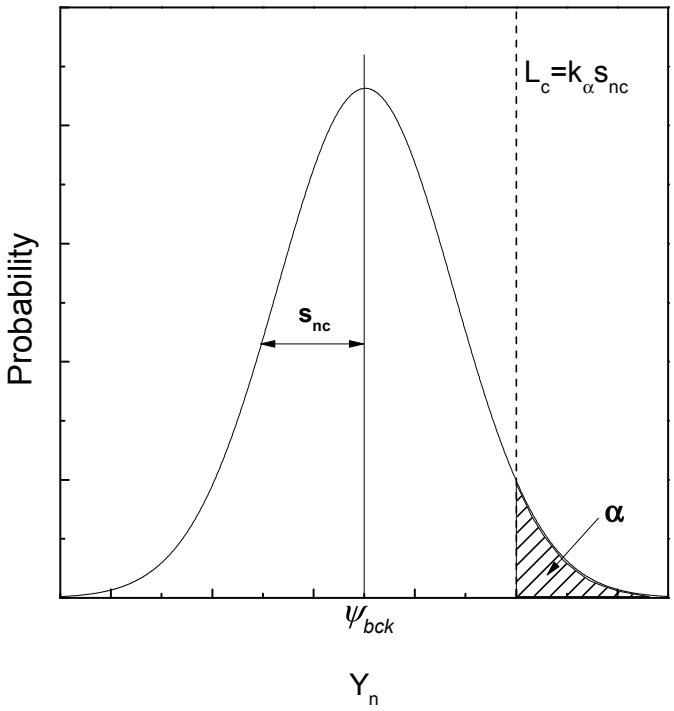

Figure 2.3: Gaussian probability distribution illustrating the net background limiting mean, ψ_{bck}. The detectable region requires the magnitude of a single inspection, Y_n, to lie above the critical decision level, L_c. The area of false positive probability (shaded), α, begins at the abscissa, k_α, defined as $\sqrt{2}\ \mathrm{erf}^{-1}(1-2\alpha)$.

which includes the variances in the gross yield, s^2_{gc}, and the limiting mean associated with the background signal, σ^2_{bck}. The variance for the gross yield is determined from Equation 2.1, noting that L_c is calculated from signals without fissioning isotopes. Utilizing properties of Poisson counting with the standard deviation determined from the square root of the counts,

$$s^2_{gc} = \frac{C_{bck}}{N^2}, \tag{2.12}$$

where C_{bck} is the expected mean of the total background counts in a single inspection. Expanding the total background into passive and active components s^2_{gc} becomes,

$$s^2_{gc} = \frac{C_{abk} + C_{pbk}}{N^2} = \frac{\Psi_{abk} N + C_{pbk}}{N^2} = \frac{\Psi_{abk}}{N} + \frac{C_{pbk}}{N^2}. \tag{2.13}$$

The active background yield, Ψ_{abk}, is introduced so that the normalization parameter can be divided between active and passive parts. Division of the normalization de-

nominator allows parameters to be associated with the active and passive inspections. The passive counts are reflected as C_{pbk}. Plugging in the variances broken into passive and active components yields a critical decision level of,

$$L_c = k_\alpha \sqrt{\frac{\Psi_{abk}}{N} + \frac{C_{pbk}}{N^2} + \sigma_{abk}^2 + \left(\frac{\Delta C_{pbk}}{N}\right)^2}. \tag{2.14}$$

Equation 2.14 reflects error propagation rules where uncertainties are added in quadrature. A complete description of detection limits, including detailed equations and various examples, is discussed in the 1968 paper by Currie [96].

2.4.2 Minimal Detection Limit

The critical decision level shows the relationship of a signal to the background and is an a posteriori detection decision, however, the minimal detectable level, L_d, is an a priori estimate because it assumes parameters that may be implemented in a detection system or technique. The minimal detectable level, in these experiments, identifies the magnitude of a yield required for a fissionable material to be distinguished from the background signal. Assuming the inspection is observed from a fissionable material, the probability of the net yield is increased above L_c. Therefore L_d is required to equal the limiting mean of the net inspection yield, Ψ_n, so that the probability for a false negative is set at β for the given L_c. The β probability incorrectly identifies a yield observed from a fissionable material as non-fissionable or "not detected". Conversely, $1-\beta$ is the confidence in predicting that a yield observed from a fissionable material is detectable. Figure 2.4 depicts the relationship of L_d to ψ_n and L_c within the related Gaussian distributions. The figure also shows the region in the distribution associated with β.

Utilizing the Gaussian integral equivalent to β as follows,

$$\int_{-\infty}^{L_c} \frac{1}{s_{nd}\sqrt{2\pi}} e^{\frac{-(Y_n - L_d)^2}{2s_{nd}^2}} dY_n = \beta, \tag{2.15}$$

and solving for L_d gives,

$$L_d = L_c + \sqrt{2}\,\mathrm{erf}^{-1}(1-2\beta)\; s_{nd} = L_c + k_\beta s_{nd}, \tag{2.16}$$

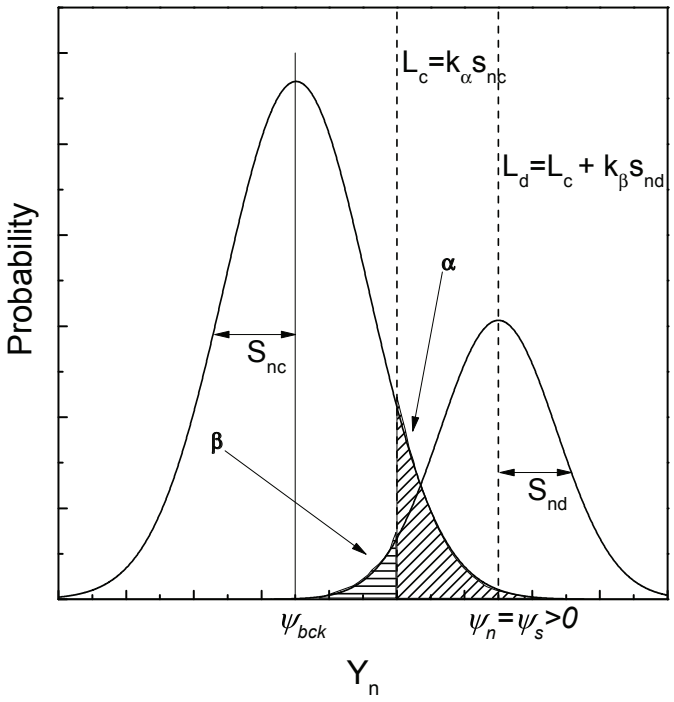

Figure 2.4: Gaussian probability distributions illustrating the net background limiting mean, ψ_{bck}, and the net yield with the corresponding limiting mean, ψ_n, that assumes measurement from a fissionable material. The minimal detectable level is defined such that $L_d = \psi_n$ with β equal to the false negative probability. The standard deviation of the net fission yield is s_{nd} with the abscissa of L_d equal to k_β. All other parameters match those mentioned in Figure 2.3

where s_{nd} is the standard deviation of the yield, assuming fissioning isotopes are present, with the limiting mean equal to L_d and k_β representing $\sqrt{2}\ \mathrm{erf}^{-1}(1-2\beta)$.

Constructing the variance of the distribution resembles the method described for L_c. As such, determining s^2_{nd} starts with Equation 2.7, hence

$$s^2_{nd} = s^2_{gd} + \sigma^2_{bck}, \tag{2.17}$$

where s^2_{gd} is the variance in the gross yield provided the limiting mean is equivalent to L_d. Expanding the variance in the gross yield gives,

$$s^2_{gd} = \frac{C_{gd}}{N^2}. \tag{2.18}$$

Since the expected counts are from a planned detection system the normalization set may be different from the known set of parameters included in the calculation for L_c. To distinguish the known normalization set, N_k, the planned set will be denoted as N_p. Therefore,

$$s_{gd}^2 = \frac{C_{gd}}{N^2} = \frac{C_{nd}}{N_p^2} + \frac{C_{bck}}{N_k^2} = \frac{Y_n N_p}{N_p^2} + \frac{\Psi_{abk} N_k + C_{pbk}}{N_k^2}, \tag{2.19}$$

where the counts, C_{nd}, are observed from a net single inspection and C_{bck} are the inherent background counts. Expanding further gives,

$$s_{gd}^2 = \frac{L_d N_p}{N_p^2} + \frac{\Psi_{abk} N_k + C_{pbk}}{N_k^2} = \frac{L_d}{N_p} + \frac{\Psi_{abk}}{N_k} + \frac{C_{pbk}}{N_k^2}. \tag{2.20}$$

Plugging the solution for s_{gd}^2 into the net variance and noting that σ_{bck}^2 is the same for L_c and L_d gives,

$$s_{nd}^2 = \frac{L_d}{N_p} + \frac{\Psi_{abk}}{N_k} + \frac{C_{pbk}}{N_k^2} + \sigma_{abk}^2 + \left(\frac{\Delta C_{pbk}}{N_k}\right)^2. \tag{2.21}$$

Observing that the last four terms in the above equation match those under the square root of L_c, the net variance for L_d can be written as,

$$s_{nd}^2 = \frac{L_d}{N_p} + \frac{L_c^2}{k_a^2}. \tag{2.22}$$

Plugging s_{nd}^2 into Equation 2.16 and using the quadratic formula to solve for L_d gives,

$$L_d = L_c + \frac{k_\beta^2}{2N_p} + k_\beta^2 \sqrt{\frac{1}{4N_p^2} + \frac{L_c}{k_\beta^2 N_p} + \frac{L_c^2}{k_\alpha^2 k_\beta^2}}. \tag{2.23}$$

Note that the smaller root of the quadratic gives zero, therefore, the larger root is utilized to solve for L_d. In the case where both the false positive and negative probabilities are equal ($\alpha = \beta$) then $k_\alpha = k_\beta$. Using this equality and factoring the terms in the square root allows,

$$L_d = \frac{k^2}{N_p} + 2L_c. \tag{2.24}$$

Similar to L_c, L_d incorporates uncertainties in the background distribution. The difference lies in the parameters defining a planned detection system or technique as

opposed to known parameters. Adjustments in the yield's limiting mean are found by assuming the signal contains fissioning isotopes. This assumption boosts the magnitude of the limiting mean to equal L_d. This allows the accuracy of a yield to be detected to within the specified confidence level. Although L_d is calculated assuming the yield includes events produced by fissioning isotopes, it does not directly consider what the signal strength would be from an actual measurement. The minimal detectable mass (M_{min}) provides a relationship between L_d and the quantity of fissionable mass required to satisfy Equation 2.24. Because the M_{min} uses direct measurements, comparisons between γ-ray and neutron signals can be made easily and indicate the sensitivity of the detection system in relation to either signal.

The connection of the M_{min} to L_d is determined through a calibration parameter. The M_{min} is therefore constructed by applying the definition of the net yield in relation to a fissionable material where $\psi_n = \psi_s$. Observing that the fission yield changes as a function of the fissionable mass, m_f, the M_{min} becomes,

$$\psi_n = \frac{d\psi_s}{dm_f} \cdot M_{min}, \tag{2.25}$$

where $d\psi_s/dm_f$ is the differential change in the fission yield per unit fissionable mass. Plugging in L_d for ψ_n and solving for M_{min} gives,

$$M_{min} = \left(\frac{d\psi_s}{dm_f}\right)^{-1} \cdot L_d. \tag{2.26}$$

In this way, the efficacy of the detection system can be determined for delayed γ-rays and neutrons by calibrating the system with low mass targets to calculate $d\psi_s/dm_f$.

2.5 Detection Limits Defined in a Two-Dimensional Detection System

Many advantages are available when utilizing a detection system that simultaneously incorporates γ-ray and neutron signals. A dual γ-ray/neutron detection system allows for a greater probability to overcome shielding and minimizes interference concerns as a measurement will not typically interfere with both γ-ray and neutron fission

signals at lower bremsstrahlung energies. Furthermore, an increase in the number of counts and therefore a decrease in uncertainty that comes from having a dual signal detection system simultaneously brings an increase in detection sensitivity. This sensitivity increase is achieved by calculating the γ-ray and neutron L_c levels concurrently which in turn increases the "detectable" region over those determined in independent calculations. The method employed for concurrent calculations is primarily the same as discussed in the previous section, however, two dimensions require a bivariate Gaussian. Similar to an ordinary one-dimensional Gaussian, a bivariate Gaussian is parameterized by the mean and variance describing the distribution, however, the form changes to a vector of limiting means, $\mathbf{Y_n}$, and a variance-covariance matrix, $\mathbf{S_{no}}$. The distribution is described by

$$\iint_{detection\ volume} \frac{1}{2\pi\sqrt{|\mathbf{S_{no}}|}} e^{\frac{-(\mathbf{Y_n}^\top \mathbf{S_{no}^{-1}} \mathbf{Y_n})}{2}} d\mathbf{Y_n} = \alpha. \tag{2.27}$$

The vector consists of the net limiting means defined by the dual phase space of neutrons, Y_{nN}, and γ-rays, $Y_{n\gamma}$. Hence $\mathbf{Y_n}$ becomes,

$$\mathbf{Y_n} = \begin{pmatrix} Y_{nN} \\ Y_{n\gamma} \end{pmatrix} = \begin{pmatrix} Y_{gN} - \psi_{bckN} \\ Y_{g\gamma} - \psi_{bck\gamma} \end{pmatrix}. \tag{2.28}$$

The use of the "N" and "γ" subscripts to represent neutrons and γ-rays respectively continues for the remainder of this discussion. The variance-covariance matrix is defined as,

$$\mathbf{S_{no}} = \begin{pmatrix} s_{noN}^2 & s_{noN}s_{no\gamma} \\ s_{no\gamma}s_{noN} & s_{no\gamma}^2 \end{pmatrix}. \tag{2.29}$$

As indicated previously, the variance is a measure of variability of an individual data set. The covariance defines how multiple sets of data move in relation to one another. In a two-dimensional set, the off-axis values for the covariances are identical. While the limiting means of fission observations may be correlated to target mass and distance from the detectors, the random nature inherent in a single inspection allows the data to be considered uncorrelated. For uncorrelated data the covariance is zero,

therefore, the variant-covariant matrix becomes,

$$\mathbf{S_{no}} = \begin{pmatrix} s_{noN}^2 & 0 \\ 0 & s_{no\gamma}^2 \end{pmatrix}, \tag{2.30}$$

where s_{noN}^2 is the variance for delayed neutron signals and $s_{no\gamma}^2$ is the variance for delayed γ-ray signals. Thus the determinant of the variant-covariant matrix is,

$$|\mathbf{S_{no}}| = s_{noN}^2 s_{no\gamma}^2. \tag{2.31}$$

The inverse matrix is defined as,

$$\mathbf{S_{no}^{-1}} = \frac{1}{s_{noN}^2 s_{no\gamma}^2} \begin{pmatrix} s_{noN}^2 & 0 \\ 0 & s_{no\gamma}^2 \end{pmatrix} = \begin{pmatrix} \frac{1}{s_{noN}^2} & 0 \\ 0 & \frac{1}{s_{no\gamma}^2} \end{pmatrix}. \tag{2.32}$$

Plugging in the results simplifies the Gaussian integral as follows,

$$\iint\limits_{detection\ volume} \frac{1}{2\pi s_{noN} s_{no\gamma}} e^{-\frac{1}{2}\left(\frac{Y_{nN}^2}{s_{noN}^2} + \frac{Y_{n\gamma}^2}{s_{no\gamma}^2}\right)} dY_{nN} dY_{n\gamma} = \alpha. \tag{2.33}$$

For these experiment, the detection volume combines the two surface boundaries defined by the critical decision levels from the dual phase space consisting of γ-rays and neutrons defined as $L_{c\gamma}$ and L_{cN} respectively. This combined single boundary defines the limits of detection and generates the "not detected" volume. Using the union and intersection of the two sets allows both signatures to be treated equally. The union corresponds to the logical "AND" and defines the "detectable" region as that above both the γ-ray and the neutron L_c. The intersection corresponds to the logical "OR" and defines the "detectable" region as above $L_{c\gamma}$ or above L_{cN}. Consequently, if the signal is "not detectable" in terms of γ-rays it is "detectable" for neutrons and vice versa. A pictograph with logical "AND" and logical "OR" volumes is displayed in Figure 2.5.

The limits of integration are determined from the surface boundaries with the logical "AND" condition defined as,

$$\int_{L_{cN}}^{\infty} \int_{L_{c\gamma}}^{\infty} \frac{1}{2\pi s_{noN} s_{no\gamma}} e^{-\frac{1}{2}\left(\frac{Y_{nN}^2}{s_{noN}^2} + \frac{Y_{n\gamma}^2}{s_{no\gamma}^2}\right)} dY_{nN} dY_{n\gamma} = \alpha. \tag{2.34}$$

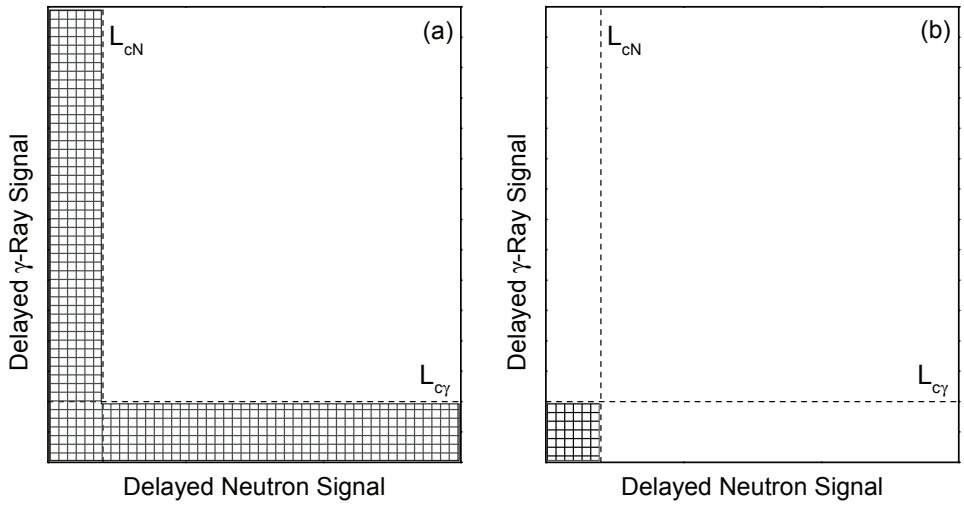

Figure 2.5: Logical "AND" (a) and logical "OR" (b) volumes depicting the "not detected" regions (shaded).

The area containing the "detectable" region that includes α is the unshaded portion of the graph of Figure 2.5b. The Gaussian integral that includes the logical "OR" condition then becomes,

$$1 - \int_{-\infty}^{L_{cN}} \int_{-\infty}^{L_{c\gamma}} \frac{1}{2\pi s_{noN} s_{no\gamma}} \, e^{-\frac{1}{2}\left(\frac{Y_{nN}^2}{s_{noN}^2} + \frac{Y_{n\gamma}^2}{s_{no\gamma}^2}\right)} dY_{nN} dY_{n\gamma} = \alpha. \tag{2.35}$$

Solving for the critical decision level and using properties of error functions, the logical "AND" L_c is defined as,

$$L_{cN} = s_{noN}\sqrt{2}\,\mathrm{erf}^{-1}\left(1 - \frac{4\alpha}{1 - \mathrm{erf}\left(\frac{L_{c\gamma}}{s_{no\gamma}\sqrt{2}}\right)}\right), \tag{2.36}$$

and the logical "OR" result is defined as

$$L_{cN} = s_{noN}\sqrt{2}\,\mathrm{erf}^{-1}\left(\frac{4(1-\alpha)}{1 + \mathrm{erf}\left(\frac{L_{c\gamma}}{s_{no\gamma}\sqrt{2}}\right)} - 1\right). \tag{2.37}$$

The result for L_{cN} is calculated by setting a value for $L_{c\gamma}$. The relationship between L_{cN} and $L_{c\gamma}$ would be reversed had the equation been solved for $L_{c\gamma}$. The critical

decision levels within the error functions of Equations 2.36 and 2.37 were chosen by normalizing the yields to their expected variances reflecting the importance of the measured uncertainty to each signal. The normalized vector becomes,

$$\mathbf{y_n} = \begin{pmatrix} y_{nN} \\ y_{n\gamma} \end{pmatrix} = \begin{pmatrix} \frac{Y_{nN}}{s_{nN}} \\ \frac{Y_{n\gamma}}{s_{n\gamma}} \end{pmatrix}.$$

Utilizing the normalized vector changes the surface boundaries to

$$\frac{L_N}{s_{noN}} \quad \text{and} \quad \frac{L_\gamma}{s_{no\gamma}}. \tag{2.38}$$

There is no clear way to choose a value for the independent L_c in Equations 2.36 and 2.37, however, intersecting the surface boundaries allows calculation of the dependent L_c to be based only on the expected variances and the required false positive rate. Intersection of boundaries simplifies the two dimensional logical "AND" critical decision level to

$$L_{cN,\gamma} = s_{ncN,\gamma}\sqrt{2}\,\mathrm{erf}^{-1}(1 - 2\sqrt{\alpha}), \tag{2.39}$$

with the logical "OR" becoming,

$$L_{cN,\gamma} = s_{ncN,\gamma}\sqrt{2}\,\mathrm{erf}^{-1}(2\sqrt{1-\alpha} - 1). \tag{2.40}$$

Plugging in the standard deviation gives,

$$L_{cN,\gamma} = \sqrt{\frac{\psi_{abkN,\gamma}}{N_k} + \frac{C_{pbkN,\gamma}}{N_k^2} + \sigma^2_{abkN,\gamma} + \left(\frac{\Delta C_{pbkN,\gamma}}{N_k}\right)^2}\sqrt{2}\,\mathrm{erf}^{-1}(1 - 2\sqrt{\alpha}) \tag{2.41}$$

for logical "AND" and

$$L_{cN,\gamma} = \sqrt{\frac{\psi_{abkN,\gamma}}{N_k} + \frac{C_{pbkN,\gamma}}{N_k^2} + \sigma^2_{abkN,\gamma} + \left(\frac{\Delta C_{pbkN,\gamma}}{N_k}\right)^2}\sqrt{2}\,\mathrm{erf}^{-1}(2\sqrt{1-\alpha} - 1) \tag{2.42}$$

for logical "OR".

2.5.1 Two-Dimensional Minimal Detection Limit

As described in the one-dimensional case the minimal detection limit, L_d, a priori defines the magnitude of yields required to detect the presence of fissionable isotopes.

Assuming fissionable isotopes are present, the probability for the net yield to increase over L_c and lie within the "detected" region is improved. As such L_d is required to equal the limiting mean, ψ_s, when the probability equals β, for a given L_c. In the two-dimensional case, $L_d = L_{dN}$ therefore $L_{dN} = \psi_{sN}$ for a given L_{cN} for delayed neutrons and $L_d = L_{d\gamma}$ therefore $L_{d\gamma} = \psi_{s\gamma}$ for a given $L_{c\gamma}$ for delayed γ-rays. Accordingly, the bivariate Gaussian for the minimal detection limit is defined as,

$$\iint\limits_{detection\ volume} \frac{1}{2\pi s_{ndN} s_{nd\gamma}} e^{\frac{-(Y_{nN}-L_{dN})^2}{2s^2_{ndN}}} e^{\frac{-(Y_{n\gamma}-L_{d\gamma})^2}{2s^2_{nd\gamma}}} dY_{nN} dY_{n\gamma} = \beta. \tag{2.43}$$

The two-dimensional logical "OR" becomes,

$$\int\limits_{-\infty}^{L_{cN}} \int\limits_{-\infty}^{L_{c\gamma}} \frac{1}{2\pi s_{ndN} s_{nd\gamma}} e^{\frac{-(Y_{nN}-L_{dN})^2}{2s^2_{ndN}}} e^{\frac{-(Y_{n\gamma}-L_{d\gamma})^2}{2s^2_{nd\gamma}}} dY_{nN} dY_{n\gamma} = \beta, \tag{2.44}$$

resulting in

$$\frac{1}{4}\left[\operatorname{erf}\left(\frac{L_{cN}-L_{dN}}{\sqrt{2}s_{ndN}}\right)+1\right]\left[\operatorname{erf}\left(\frac{L_{c\gamma}-L_{d\gamma}}{\sqrt{2}s_{nd\gamma}}\right)+1\right] = \beta. \tag{2.45}$$

The two dimensional logical "AND" is therefore defined as,

$$1 - \int\limits_{L_{cN}}^{\infty} \int\limits_{L_{c\gamma}}^{\infty} \frac{1}{2\pi s_{ndN} s_{nd\gamma}} e^{\frac{-(Y_{nN}-L_{dN})^2}{2s^2_{ndN}}} e^{\frac{-(Y_{n\gamma}-L_{d\gamma})^2}{2s^2_{nd\gamma}}} dY_{nN}\, dY_{n\gamma} = \beta, \tag{2.46}$$

resulting in

$$1 - \frac{1}{4}\left[1-\operatorname{erf}\left(\frac{L_{cN}-L_{dN}}{\sqrt{2}s_{ndN}}\right)\right]\left[1-\operatorname{erf}\left(\frac{L_{c\gamma}-L_{d\gamma}}{\sqrt{2}s_{nd\gamma}}\right)\right] = \beta. \tag{2.47}$$

Solving for the minimal detection level for one signature in both the logical "AND" and "OR" gives similar results where,

$$L_{dN,\gamma} = L_{cN,\gamma} + \frac{k^2_{\beta N,\gamma}}{2N_p} + k^2_{\beta N,\gamma}\sqrt{\frac{1}{4N_p^2} + \frac{L_{cN,\gamma}}{k^2_{\beta N,\gamma}N_p} + \frac{L^2_{cN,\gamma}}{k^2_{\alpha N,\gamma}k^2_{\beta N,\gamma}}}. \tag{2.48}$$

However, definitions for k_α and k_β differ. The logical "AND" results in,

$$k_{\alpha N,\gamma} = \sqrt{2}\,\operatorname{erf}^{-1}\left[1 - \frac{4\alpha}{1-\operatorname{erf}\left(\frac{L_{c\gamma,N}}{s_{nc\gamma,N}\sqrt{2}}\right)}\right], \tag{2.49}$$

and

$$k_{\beta N,\gamma} = \sqrt{2}\,\mathrm{erf}^{-1}\left[1 - \frac{4(1-\beta)}{1-\mathrm{erf}\left(\frac{L_{c\gamma,N}-L_{d\gamma,N}}{s_{nd\gamma,N}\sqrt{2}}\right)}\right]. \tag{2.50}$$

Results for logical "OR" become,

$$k_{\alpha N,\gamma} = \sqrt{2}\,\mathrm{erf}^{-1}\left[\frac{4(1-\alpha)}{1+\mathrm{erf}\left(\frac{L_{c\gamma,N}}{s_{nc\gamma,N}\sqrt{2}}\right)} - 1\right], \tag{2.51}$$

and

$$k_{\beta N,\gamma} = \sqrt{2}\,\mathrm{erf}^{-1}\left[1 - \frac{4\beta}{1+\mathrm{erf}\left(\frac{L_{c\gamma,N}-L_{d\gamma,N}}{s_{nd\gamma,N}\sqrt{2}}\right)}\right]. \tag{2.52}$$

The expected variances and critical decision levels are determined through equations 2.13 , 2.19, 2.41, and 2.42. Notice that k_β includes the detection level for the alternate fission signal. Therefore, when solving for the detection level of one fission signal a value must be set for the alternate fission signal. This is accomplished by using the detection level found in the one-dimensional case as the limit and increasing (or decreasing) in steps until the boundary is met. This method was utilized in the analysis to follow.

Calibrating the detection system with targets of known fissionable masses allows the minimal detectable mass to be determined in a similar fashion as described in the one-dimensional case. Similar to the one-dimensional case and requiring the vector representation,

$$M_{min} = \left(\frac{d\mathbf{\Psi_s}}{dm_f}\right)^{-1} \cdot \mathbf{L_d}. \tag{2.53}$$

The neutron and γ-ray fission signals, $\mathbf{\Psi_s}$, separately use the fission mass as a parameter to form a line extending from the background yields into the detectable volume. The intersection of this line with the L_d curve determined from logical "AND" or "OR" gives the minimal detectable mass.

2.6 Integral Yields

The critical decision levels defined in the previous section give the boundary for the detectable region. At bremsstrahlung endpoint energies below ~16 MeV, the

boundary provides a clear division between fissionable and non-fissionable materials. However, as interferences begin to emerge, the boundary can no longer be used as a reliable indicator of fissioning materials. The likelihood that a non-fissionable material will cross the boundary into the detectable region can be estimated by the production cross section. Production cross sections are listed in Table 2.4 of section 2.3 for the potential interference reactions. The production cross sections listed Table 2.4 were available in the TENDL-2014 and/or ENDF/B-VII.1 libraries or measured experimentally and listed in EXFOR. However, discrepancies between listed cross sections makes simulating interferences challenging. In an attempt to show how a simulated signal would compare to a measured signal, the bremsstrahlung weighted integral yields and measured integral yields for a few interferences were calculated. The bremsstrahlung weighted integral yields were calculated in lieu of production cross sections because the broad distribution of photon energies comprising the beam compounds the cross section measurements.

Integral yields are linked to the experimental calculations through the production rate defined as,

$$P = N_T \int_{E_i}^{E_f} \frac{d\Phi}{dE_\gamma} \sigma_p(E_\gamma)\, dE_\gamma, \tag{2.54}$$

where P is proportional to the photon flux,Φ, the production cross section, σ_p, and the number of target isotopes, N_T, in the material. The reaction products are produced during a given bremsstrahlung pulse and then begin to decay. The reaction products that are produced during the initial photon pulse are determined by,

$$\frac{dN_{op}}{dt} = P - \lambda N_{op}, \tag{2.55}$$

where N_{op} is the population of reaction products present during the initial pulse, λ is the decay constant, and P is the production rate defined in equation 2.54. To account for the occurrence of a series of pulses and the corresponding summations that are ultimately utilized, notation for the initial pulse begins at k=0. By solving for N_{op} and assuming it's equivalence to zero at t=0,

$$N_{op} = \frac{P}{\lambda}(1 - e^{-\lambda t_p}). \tag{2.56}$$

The irradiation time, t_p, is used to calculate the number of reaction products generated within the pulse.

Following the initial pulse and during the detection period, the population decays in time governed by the radioactive decay law, therefore, the subscript in the reaction products N changes to "*od*", requiring

$$N_{od} = \frac{P}{\lambda}(1 - e^{-\lambda t_p})e^{-\lambda(t-t_p)}, \tag{2.57}$$

where t-t_p is the time elapsed after the initial pulse and t is always greater than t_p. By utilizing the rate of change of N_{od}

$$\frac{dN_{od}}{dt} = -P(1 - e^{-\lambda t_p})e^{-\lambda(t-t_p)}, \tag{2.58}$$

the detection rate for a discrete γ-ray is determined as

$$R_{od} = \epsilon\beta P(1 - e^{-\lambda t_p})e^{-\lambda(t-t_p)}. \tag{2.59}$$

The branching ratio, β, gives the decay intensity of a specific discrete γ-ray emitted with an absolute photopeak efficiency of ϵ.

The number of γ-rays detected beginning at time t_o and ending at the final detection time, t_f, becomes,

$$C_{0d} = \int_{t_o}^{t_f} R_{od}\,dt = \epsilon\beta P(1 - e^{-\lambda t_p}) \int_{t_o}^{t_f} e^{-\lambda(t-t_p)}\,dt = \frac{\epsilon\beta P}{\lambda}(1 - e^{-\lambda t_p})\left[e^{-\lambda(t_o-t_p)} - e^{-\lambda(t_f-t_p)}\right]. \tag{2.60}$$

Equation 2.60 gives the counts detected after the initial pulse, however, the data measured contains contributions arising from a series of bremsstrahlung pulses. Setting $\frac{\epsilon\beta P}{\lambda}(1 - e^{-\lambda t_p})$ equal to C_p in the equation directly above, the counts after the second pulse with k=1 becomes,

$$C_{1d} = C_p\left\{\left[e^{-\lambda(t_o-t_p)} - e^{-\lambda(t_f-t_p)}\right] + \left[e^{-\lambda((t_o+\Delta t)-t_p)} - e^{-\lambda((t_f+\Delta t)-t_p)}\right]\right\}. \tag{2.61}$$

The measure of time starting at the beginning of a pulse and continuing to the start of the next pulse is Δt. Continuing to the third pulse gives,

$$\begin{aligned} C_{2d} = {} & C_p\left\{\left[e^{-\lambda(t_o-t_p)} - e^{-\lambda(t_f-t_p)}\right] + \left[e^{-\lambda((t_o+\Delta t)-t_p)} - e^{-\lambda((t_f+\Delta t)-t_p)}\right]\right\} \\ & + C_p\left\{\left[e^{-\lambda((t_o+2\Delta t)-t_p)} - e^{-\lambda((t_f+2\Delta t)-t_p)}\right]\right\}. \end{aligned} \tag{2.62}$$

The pattern continues for an arbitrary number of pulses with

$$\begin{aligned} C_{nd} &= C_p \sum_{k=0}^{n} e^{-\lambda(t_o+k\Delta t-t_p)} - e^{-\lambda(t_f+k\Delta t-t_p)} \\ &= C_p \left(e^{-\lambda(t_o-t_p)} - e^{-\lambda(t_f-t_p)}\right) \sum_{k=0}^{n} e^{-\lambda k\Delta t}. \end{aligned} \tag{2.63}$$

The final summation in Equation 2.63 can be written in the form of a geometric series where,

$$\sum_{k=0}^{n-1} (ar)^k = a\frac{1-r^n}{1-r} \tag{2.64}$$

By using the solution for the geometric series the number of counts becomes,

$$C_{nd} = C_p \left[e^{-\lambda(t_o-t_f)} - e^{-\lambda(t_f-t_p)}\right] \frac{1-e^{-\lambda(n+1)\Delta t}}{1-e^{-\lambda\Delta t}}. \tag{2.65}$$

The photons detected in Equation 2.65 are counted following an arbitrary pulse in a series of pulses, however, detection occurs between every pulse with the total counts reflecting this summation. Therefore, the number of detected photons becomes,

$$C_{nd} = C_p \left[\frac{e^{-\lambda(t_o-t_p)} - e^{-\lambda(t_f-t_p)}}{1-e^{-\lambda\Delta t}}\right] \sum_{n=0}^{n_p-1} (1-e^{-\lambda(n+1)\Delta t}). \tag{2.66}$$

Where n_p in the summation notation is the total number of bremsstrahlung pulses. Note that,

$$\sum_{n=1}^{n} 1 - a^{nr} = n - \sum_{n=1}^{n} a^{nr}. \tag{2.67}$$

Incorporating these results with the number of pulses from n=1 to n_p gives,

$$C_{nd} = \frac{\epsilon\beta P}{\lambda}(1-e^{-\lambda t_p}) \left[\frac{e^{-\lambda(t_o-t_p)} - e^{-\lambda(t_f-t_p)}}{1-e^{-\lambda\Delta t}}\right] \left[n_p - e^{-\lambda\Delta t}\frac{1-e^{-\lambda n_p\Delta t}}{1-e^{-\lambda\Delta t}}\right]. \tag{2.68}$$

Setting the two equations within square brackets equal to the number of modified pulses, N_{mp}, and solving for the production rate yields,

$$P = \frac{C_{nd}\lambda}{\epsilon\beta(1-e^{-\lambda t_p})N_{mp}}. \tag{2.69}$$

The bremsstrahlung integral yield, defined in equation 2.54, equals,

$$\int_{E_i}^{E_f} \frac{d\Phi}{dE_\gamma}\sigma(E_\gamma)\, dE_\gamma = \frac{C_{nd}\lambda t_p}{\epsilon\beta(1-e^{-\lambda t_p})N_{mp}N_T}, \tag{2.70}$$

The bremsstrahlung flux, $\frac{d\Phi}{dE_\gamma}$, included on the left side of Equation 2.70, was simulated with MCNPX [70]. MCNPX provides a fluence, therefore the equation above is modified with the addition of the pulse time. Target and experimental geometries were modeled with source electrons incident on a tungsten radiator. The fluence was simulated using a track length estimate through a cell. The cell was modeled to match the physical dimensions of the specific targets utilized to measure the integral yields. The output tally was divided by the energy bin width with the ratio multiplied by the production cross section, $\sigma_p(E_\gamma)$, obtained from either TENDL-2014, ENDF/B-VII.1, or EXFOR. The average number of measured electrons per pulse incident on the radiator during the experiment was multiplied by the integral for each energy simulated. The energy of source electrons in the simulation increased in steps to match the experiment.

The measured integral yield makes up the right side of equality 2.70 and is comprised of the counts, C_{nd}, within the γ-ray signature region measured from a specific photopeak produced by the decaying reaction product generated through an interfering reaction. Along with C_{nd}, the pulse width, t_p, was determined from the experiment. Both λ and β were found in the ENDF/B-VII.1 reaction library. Absolute photopeak efficiencies, ϵ, were simulated with MCNP and provided by M. T. Kinlaw of Idaho National Laboratory. The number of parent isotopes in the target was derived from the density (d), isotopic molecular weight (m_w), the volume of material in the beam (V), and the estimated void fraction (f_v). Therefore, N_T is,

$$N_T = (1 - f_v)\frac{Vd}{m_w(1/A)},$$

where A is Avagadro's number. Division of the volume with the density gave a calculated mass which was compared to the measured mass to determine the void fraction. The density was obtained from the material's safety data sheet for all materials with measured integral yields.

Equation 2.70 defines the integral yields that result from a single reaction, however, if multiple reactions from the same element (i.e. ^{35}Cl and ^{37}Cl) produce the same reaction product, then the bremsstrahlung integral yield is weighted by the isotopic

abundance, I_{abund} as follows,

$$\Sigma_{brem} = \sum_{i=1}^{n} (I_{abund})_i \cdot \int_{E_i}^{E_f} \frac{d\Phi}{dE} \cdot \sigma_i dE. \tag{2.71}$$

If the photopeak utilized to calculate the measured integral yield was comprised of multiple reactions with the same parent isotope and different reaction products (i.e. ^{23}Na(γ,^{3}He/3n)^{20}F/^{20}Na), the measured integral yield becomes,

$$\Sigma_{measured} = \sum_{i=1}^{n} w_i \cdot \frac{C_{nd}\lambda t_p}{\epsilon\beta(1-e^{-\lambda t_p})N_{mp}N_T}, \tag{2.72}$$

where w_i is a weight factor corresponding to the reaction. The weight factor includes the production cross section listed in ENDF, TENDL, or EXFOR, therefore, multiple measured integral yields may result. The weight factor was determined by integrating the production cross section for each reaction and then calculating the ratio.

Simulated and measured integral yields were compared for five targets: Ca, KBr, $H_2^{18}O$, LiF, and NaCl. Target selection was based on significance of the interference in addition to the observation of a photopeak with measurements that provided acceptable counting statistics. Table 2.5 lists the five targets along with their density, in-beam volume, void fraction, and the number of parent isotopes within the sample before irradiation. Standard error propagation rules were utilized to determine the

Table 2.5: Parameters to calculate the number of parent isotopes in the sample.

Target	Density (g cm^{-3})	In-beam Volume (cm^3)	Void Fraction	Number of Atoms
Ar	0.00166	531	0	$1.33 \times 10^{22} \pm 2.05 \times 10^{21}$
Ca	1.54	82	0.50	$9.34 \times 10^{23} \pm 9.58 \times 10^{21}$
KBr	2.75	102	0.49	$7.28 \times 10^{23} \pm 7.28 \times 10^{22}$
$H_2^{18}O$	1.11	42	0	$1.26 \times 10^{24} \pm 1.26 \times 10^{23}$
LiF	2.635	82	0.70	$1.53 \times 10^{24} \pm 1.64 \times 10^{22}$
NaCl	2.17	73	0.28	$1.30 \times 10^{24} \pm 1.64 \times 10^{23}$

listed errors with uncertainty considered in mass, volume, and void fraction. Isotopic molecular weights were found in publications by G. Audi and A. H. Wapstra [97,98]. In addition, in-beam non-fissionable target masses are listed in Table 3.2.

Chapter 3

Experimental Program

The experiments ran a total of five weeks performed in non-consecutive one-week increments over the course of two years. In the first week, the goal was to irradiate 19 non-fissionable targets chosen for their potential to undergo reactions that would produce interfering signals. All targets were irradiated at a bremsstrahlung endpoint energy of 38 MeV including 3 fissionable targets that were utilized as reference signals. Due to beam stability concerns, the highest energy initially achievable was 38 MeV. As the experiment progressed, the energy was pushed to 42 MeV with time allowed for the irradiation of 9 total targets. The accelerator operation time for each target was from 15 minutes to 3.5 hours with the duration depende....nt on the observation of relevant photopeaks with statistical errors below 5%. Targets with bremsstrahlung radiation as the dominant signature interference were observed for an average of 30 minutes to allow for minimal statistical errors (~1%) on the total gross yield.

In the second week of the experimental progam, the highest accelerator energy achievable was 44.75 MeV with targets displaying observable peaks from the first week irradiated along with several additional targets that were initially not included. The accelerator operation times were similar to those conducted in the first week of the experiment. Some of the samples were irradiated at 37 and 29 MeV bremsstrahlung endpoint energies depending on relevant reaction threshold energies. The goal in this week was to observe the magnitude of interferences from additional targets and to reproduce interferences in targets that were repeated from the first week of the

experiment.

In the third week, irradiation of targets occurred at bremsstrahlung endpoint energies of 19, 24, 29, 34, 39 and 45 MeV with signals from 1 fissionable and 12 non-fissionable samples observed. Targets were irradiated at energies above relevant interference reaction thresholds, therefore, not all samples were irradiated at every energy. Similar to the first two weeks, the accelerator operated for ~10 minutes to ~1.3 hours on samples with time allowed for minimal statistical errors on relevant photopeaks or total gross yields. Targets were irradiated based on signal observations in the prior two weeks of experimentation. The goal was to observe the progression of interference magnitudes at increasing incident energies.

The forth week consisted of irradiating 44 targets including a blank (i.e. no target irradiated) and 11 with fissioning isotopes. Targets from the previous weeks were irradiated along with several additional samples. The accelerator operated at energies of 15, 22.5, 30, 37.5, and 43 MeV for a duration of ~10 minutes per target, however, time constraints allowed for irradiation of only ^{18}O at 43 MeV. The signal observation time was reduced, in relation to previous weeks, to more closely match those conducted in real-world detection scenarios. Data obtained from the forth week was predominately used in the dual signal phase space graphs displayed in the Results section to follow.

The last week of experiments were performed predominately to obtain data relevant to calculating the measured integral yields. Nine targets, including 8 non-fissionable, were irradiated at bremsstrahlung endpoint energies ranging from 19 to 43 MeV with energy increasing in 5 MeV increments with the exception of the final energy. The highest electron energy achievable was 43 MeV. Targets were irradiated at energies above relevant interference reaction energy thresholds. The duration of accelerator operation per target was such that minimal statistical errors (~1%) were obtained for applicable photopeaks indicating interference reactions.

The fissionable masses used throughout the experiment in varying weeks are listed in Table 3.1. Concentrations are listed for aqueous solutions and mixtures in SiO_2. Thorium nitrate ($Th(NO_3)_4(H_2O)_4$) or uranyl nitrate ($UO_2(NO_3)_2(H_2O)_6$) were dissolved in 1 L of deionized water to produce the aqueous solutions, while mixtures were produced from SiO_2 and either thorium dioxide (ThO_2) or uranium oxide (U_3O_8).

Non-fissionable targets utilized throughout the experiment in varying weeks are listed in Table 3.2 along with their in-beam compound masses. The bar delineates commercial products from chemical compounds. All non-fissionable targets were conditioned after irradiation by allowing a cooling period for radiation die-away. Cooling was maintained until the activity of measured photopeaks, produced from interfering reactions, reached a rate that provided an uncertainty of 1% or less.

Table 3.1: Fissionable masses, concentrations in solutions of H_2O and mixtures of SiO_2, and in-beam masses.

Target	Type	Mass (g)	Concentration (%)	In-Beam Mass (g)
^{238}U	metal	2600	-	410
^{238}U	metal	1300	-	205
^{232}Th	metal	691	-	691
^{239}Pu	metal	9	-	9
^{238}U	H_2O solution	10.0	1.0%	0.9
^{238}U	H_2O solution	52.3	4.7%	4.7
^{238}U	H_2O solution	94.1	7.8%	8.5
^{232}Th	H_2O solution	84.0	7.0%	7.6
^{232}Th	H_2O solution	110.5	8.8%	10
^{238}U	SiO_2 mixture	8.25	0.5%	0.7
^{238}U	SiO_2 mixture	109.74	6.0%	9.9
^{238}U	SiO_2 mixture	150.14	8.0%	13.5
^{232}Th	SiO_2 mixture	105.61	6.0%	9.5

3.1 Geometry

Data were obtained utilizing the 45 MeV linear electron accelerator at the Idaho Accelerator Center. Beam energies were generated from electrons pulsed in ~2 μs increments at a 15 Hz repetition rate over all weeks that the experiment was conducted. The average electron charge per pulse ranged from 53 to 227 nC for energies from 15 to 45 MeV. Care was taken to setup a consistent geometry throughout the five non-consecutive weeks of experimentation. The schematic of Figure 3.1 displays measurement details beginning with electrons incident on a 4.2 g cm^{-2} tungsten radiator. Bremsstrahlung photons traversed 53 cm through a 30 cm thick Pb wall with

Table 3.2: In-beam non-fissionable sample compound masses.

Target	Mass (g)
Al	128.0
Ar	0.883
Be	560.7
BN	67.6
C (graphite)	598.5
C_2F_4	553.4
$C_6H_{11}KO_7$	72.9
Ca	62.5
Cu	766.6
Fe	396.2
KBr	176.0
KF	59.1
LiF	65.7
Na	5.9
$Na_2B_4O_7 \cdot 10H_2O$	105.2
NaCl	127.3
Ni	95.5
H_2O	757.2
$H_2^{18}O$	40.5
H_2O - NaCl (2.9%)	782.8
Pb	487.0
PbBe (12% Be)	347.1
S	88.0
SiN	63.3
SiO_2	148.0
Zn	316.4
Zr	164.9
Beef	409.2
Concrete	337.7
Diesel Fuel	234.8
Watermelon	217.4
Wood	151.8

2.9 cm diameter entrance and 5.08 cm diameter exit collimators. The beam continued 1.9 m to a 15.24 cm thick Pb collimator with a diameter of 1.3 cm and on through a penetration in a 1.8 m thick wall. Exiting a 3.8 cm diameter Pb collimator the beam propagated 1.5 m to the target location producing a beam spot ~4.0 cm in diameter. The total distance from radiator to target measured 6.3 m. Signals were observed

from three types of detectors; $Bi_4Ge_3O_{12}$ (BGO), ^3He, and high-purity germanium (HPGe).

A 2×3 array of 5.1 cm diameter by 5.1 cm thick $Bi_4Ge_3O_{12}$ (BGO) scintillators was utilized to observe γ-ray signals. The center and front face of the array was placed 1 m from and perpendicular to the axis of the target location. Each BGO detector and coupled photomultiplier tube was shielded with 5.1 cm of Pb on the cylindrical sides to minimize energy deposition during the beam pulse. The structure of the array was fabricated from borated polyethylene to minimize neutron absorption in the BGO crystals. A 15.24 cm thick Pb brick wall was constructed on the beam side of the array to provide additional shielding from the intense pulse of bremsstrahlung radiation. A photo of the BGO array and shielding is shown in Figure 3.2 with the left hand side of the structure facing the upstream direction of the beam. In addition, each BGO detector was offset from the planar face of the structure 2.54 cm providing additional collimation for target emitted γ-rays thus minimizing background signals. Pb shot shielded the rear of each detector minimizing γ-ray detection from all angles excluding the direction of the target.

A linear array of five 10-atm ^3He proportional counters was utilized to observe neutron signals. The array center was placed 1 m and at a 137^o angle counter clockwise beginning from the opposite wall of beam entry. Each proportional counter was surrounded by a 2.54 cm thick polyethylene cylinder, 110 μm thick sheet of Cd, and a 6.34 mm thick sheet of borated elastomer to moderate fission neutrons and minimize the capture of thermal neutrons. Neutrons produced during the accelerator pulse lose energy to thermal energies through interactions with matter in the environment. Pulse processing electronics were incorporated into each detector providing a logic pulse at the onset of neutron detection. A detailed description of detector geometry, moderation, and shielding can be found in the dissertation of M. T. Kinlaw [24].

An 80% relative efficiency HPGe detector with an active volume of ~435 cm^3 was utilized to measure discrete γ-rays. The detector structure was positioned ~0.4 m from the target location with the detector front face inset 2.58 cm. The cylindrical sides were shielded with 5.08 cm of Pb followed by at least 20 cm of borated polyethylene. The detector position allowed room for a 2.54 cm thick disk of borated polyethylene

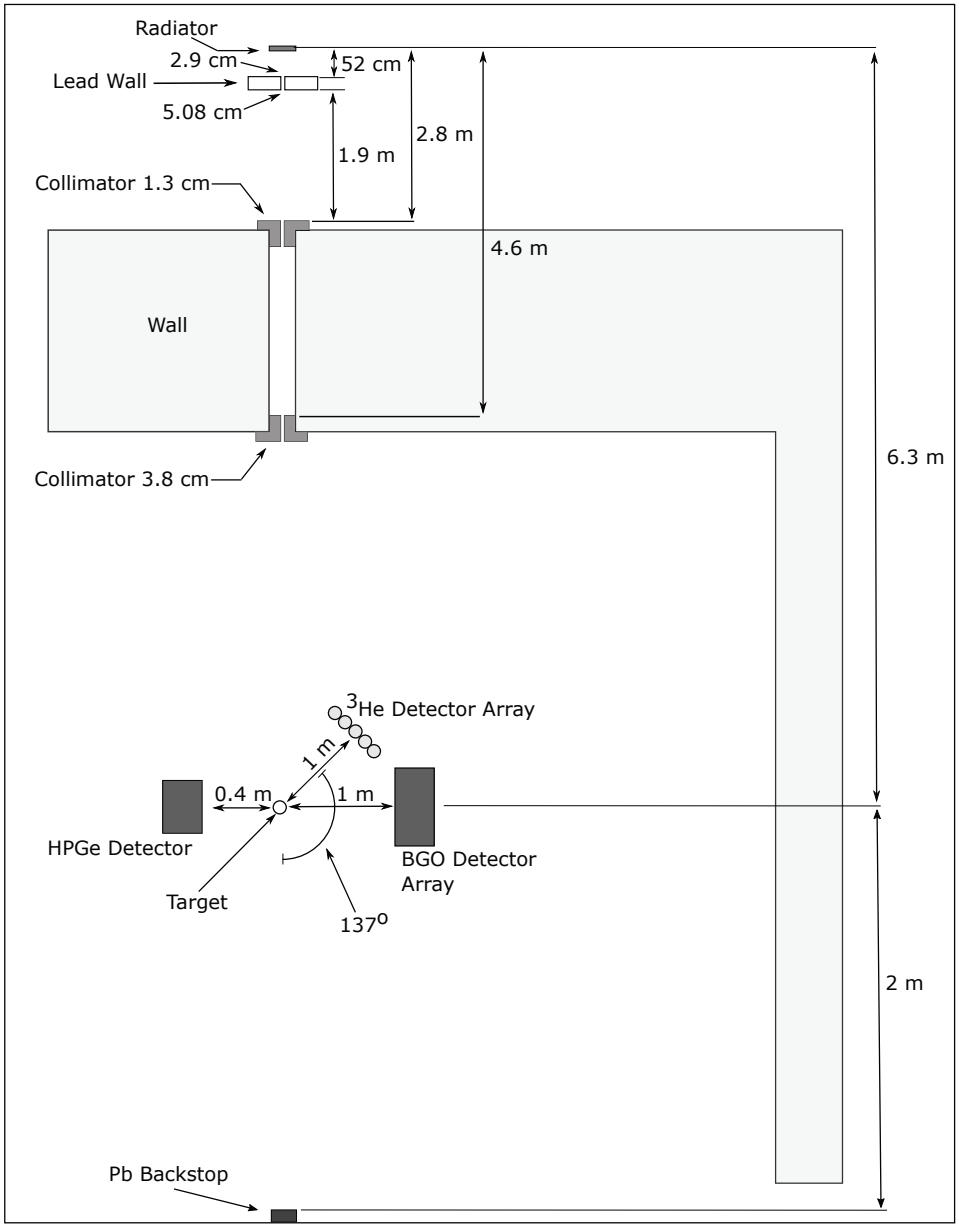

Figure 3.1: Schematic diagraming measurement details utilized for all five weeks of experimentation.

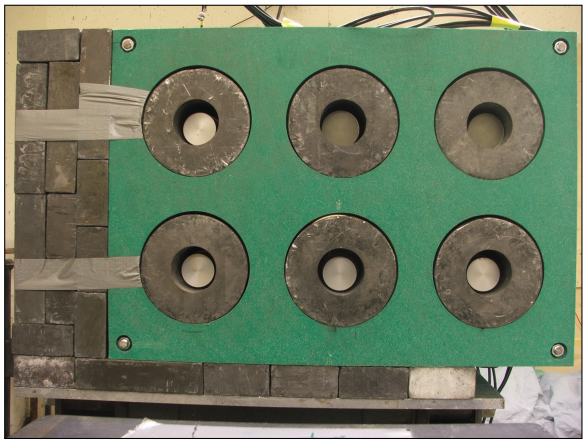

Figure 3.2: Photo of BGO array with left hand side facing the upstream direction of the bremsstrahlung beam.

to lie flush with the structure. The borated polyethylene was utilized to minimize neutron background contributions and prevent neutron damage. In addition, a 0.6 cm thick Pb filter covered the front face providing shielding from low energy γ-rays thus minimizing detector dead time. Similar to the BGO array, a 15.24 cm Pb shielding wall was positioned on the side of the detector structure facing the upstream of the beam to minimize energy deposited in the detector during the bremsstrahlung pulse. In addition, Pb shot shielded the rear of the detector.

A Pb backstop was positioned 2 m from and on axis to the target location directly in front of the wall at the far end of the bremsstrahlung beam. The Pb absorbed or attenuated energy of bremsstrahlung photons minimizing their scatter off the wall and their return to the detectors. The backstop measured $20.32 \times 20.32 \times 35.56$ cm; height being the largest dimension.

3.2 Timing and Electronics

Targets were irradiated at a 15 Hz repetition rate allowing for a detection interval between pulses of ~66.6 ms. Signals were conditioned through preamplifiers and amplifiers followed by analog conversion in preparation for data acquisition. A visual summary of electronics and instrumentation is detailed in Figure 3.3.

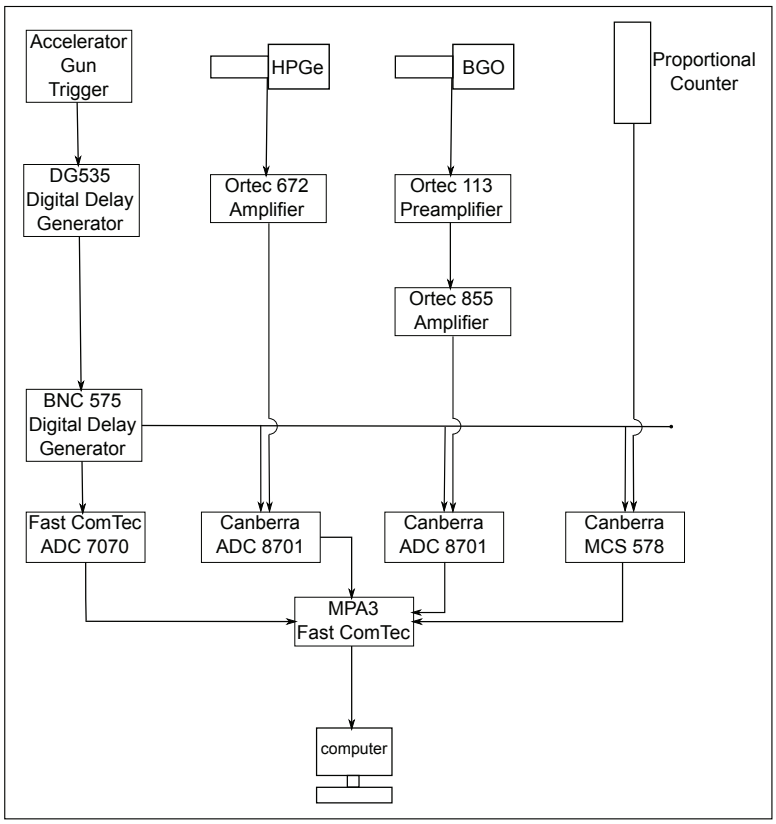

Figure 3.3: Electronics diagram including instrumentation and data acquisition system.

The accelerator pulse initiates the timing cycle referenced in the γ-ray and neutron signature definitions. The function of the Stanford Research Systems DG535 Digital Delay/Pulse Generator was to convert the electron pulse into a positive signal for input to the BNC 575 Digital Delay/Pulse Generator which only supports positive signals [99]. The BNC was employed because it offers eight output channels that were utilized to configure multiple timing events.

Signals from the HPGe detector were amplified through the Ortec 672, ideally suited for germanium detectors [100]. Signals from the BGO detectors were converted from a charge to a voltage pulse in the Ortec 113 preamplifier [101]. The signal continued to the Ortec 855 amplifier. A 93 Ω terminator was used at signal input of the Ortec 855 to reduce reflection to the amplifier which was designed with an impedance of ~1000 Ω [101, 102]. The 855 amplifier offers dual amplification in a

single width NIM module saving space for multiple detectors [102]. The analog signals from both detector types are converted to digital in the Canberra 8701 Analog to Digital Converter (ADC). The BNC 575 Digital Delay/Pulse Generator triggers the 8701 ADCs after a 1 ms gate allowing time for detector recovery after the intense accelerator pulse. Events from the proportional counters are recorded as a function of time in the Canberra 578 Multichannel Scaler (MCS) with neutron counting initiated following a 4μs pulse generated in the BNC 575. The 4μs programmed pulse was designed to mimic the gun trigger from the accelerator. An additional 4μs pulse was used to initiate analog to digital conversion in the Fast ComTec 7070 ADC which processed the pulses produced by the accelerator during target irradiation. All events were recorded in an event-by-event list mode by the Fast ComTec Multiparameter Multichannel Analyzer (MPA3). The MPA3 interfaced with the computer through a PCI-bus with MPANT software from Fast ComTec utilized for spectroscopy.

3.3 Beam Stability

A 2.54×2.54 cm^2 0.032 mm thick 99.95% metal basis gold foil with an average mass of 608 mg was fastened to each target to monitor the photon flux. The ^{197}Au(γ,n) reaction was utilized to monitor the photon flux by observing the activity of the 355.7 keV γ-ray from the decay of ^{196}Au [40,41]. The reaction was utilized because of the long decay half-life of ^{196}Au (6.17 d) and the reaction threshold energy (8.1 MeV) [39–41]. Following target irradiation, the Au foil was transported to a room outside the radiation zone and placed on a shelf 20 cm from an Ortec GEM series Coaxial 40% relative efficiency HPGe detector for counting. The HPGe detector was utilized for various applications during the experiment, therefore, cooling of the Au foils was inevitable and dictated by detector availability. While inevitable, the cooling times only accounted for minor adjustments in the photon flux calculations because the half-life of ^{196}Au was substantially longer. The area of the 355.7 keV photopeak, A_{cnts}, was determined through the MPANT software using a Gaussian fit with automatic linear background subtraction for each foil.

The photon flux is proportional to A_{cnts} through the following formula adjusted

from the work presented by Zaman et al and Naik et al [103, 104],

$$\Phi(E_\gamma) = \frac{Q_{pulse}}{e^-} \frac{A_{cnts}\lambda}{N_T \langle \sigma_r(E_\gamma) \rangle \beta\epsilon(1-e^{-\lambda t_p})P_{decay}e^{-\lambda t_{cool}}(1-e^{-\lambda t_{foil}})}. \tag{3.1}$$

The equation parameters correspond to the Au foils including the number of target atoms, N_T, the ^{196}Au decay constant, λ (1.3×10^{-6} s^{-1}), the branching ratio of the 355.7 keV γ-ray, β (86.96%), and the 40% relative efficiency HPGe detector photopeak efficiency, ϵ, at ~356 keV ($6.94{\times}10^{-3}$) [40, 41]. The efficiency was calculated using the activity of the following button sources: ^{22}Na, ^{54}Mn, ^{60}Co, ^{133}Ba, and ^{137}Cs. The number of decay pulses, P_{decay}, is equivalent to Equation 2.65 and contains energy contributions from isotopes produced in pulses leading up to and including the final pulse. The pulse width, the cooling time, and the foil detection time are t_p, t_{cool}, and t_{foil} respectively. Counts were observed until statistical errors of 1% were reached for the 355.7 keV γ-ray. The electron charge, e^-, was divided by the average charge per pulse, Q_{pulse}, to give the photon flux per number of source electrons generated by the accelerator in the experiment.

The denominator of the photon flux includes the average reaction cross section, $\langle \sigma_r(E_\gamma) \rangle$. The bremsstrahlung photon flux, $\phi(E_\gamma)$, and the ^{197}Au(γ,n)^{196}Au reaction cross section, $\sigma(E_\gamma)$, are integrated to form $\langle \sigma_r(E_\gamma) \rangle$ through the following equation,

$$\langle \sigma_r(E_\gamma) \rangle = \frac{\int_{E_\gamma=E_r}^{E_\gamma=E_b} \phi(E_\gamma)\sigma(E_\gamma)dE_\gamma}{\int_{E_\gamma=E_r}^{E_\gamma=E_b} \phi(E_\gamma)dE_\gamma}. \tag{3.2}$$

The simulated bremsstrahlung photon flux was modeled with MCNP6 using the Au target geometry along with geometrical components of the experimental setup similar to that described in Theory section 2.6. The reaction cross section, $\sigma(E_\gamma)$, was obtained from TENDL-2014 [40, 49, 75]. The energy limits in the integral start from the reaction threshold, E_r, and continue to the endpoint energy of the bremsstrahlung beam, E_b.

The photon flux for the ^{18}O, LiF, NaCl, Ca, and KBr targets is displayed in Figures 3.4, 3.5, 3.6, 3.7, and 3.8 respectively. Discussion of beam stability in relation to the measured integral yields is presented in the Results chapter, section 4.3.

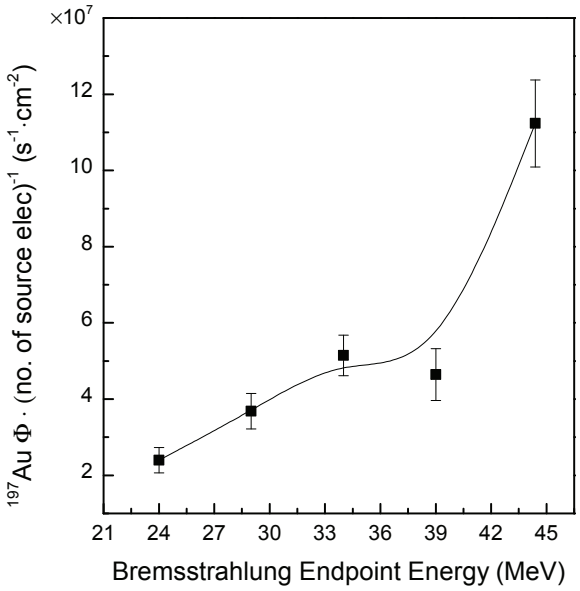

Figure 3.4: Photon flux though gold foil fastened to ^{18}O target.

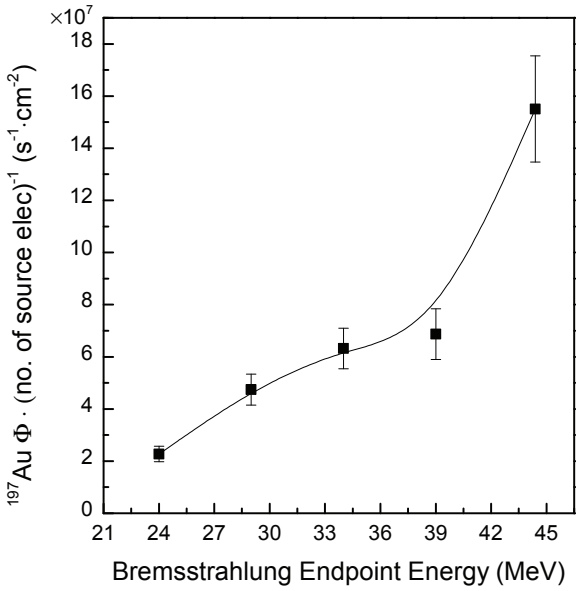

Figure 3.5: Photon flux though gold foil fastened to LiF target.

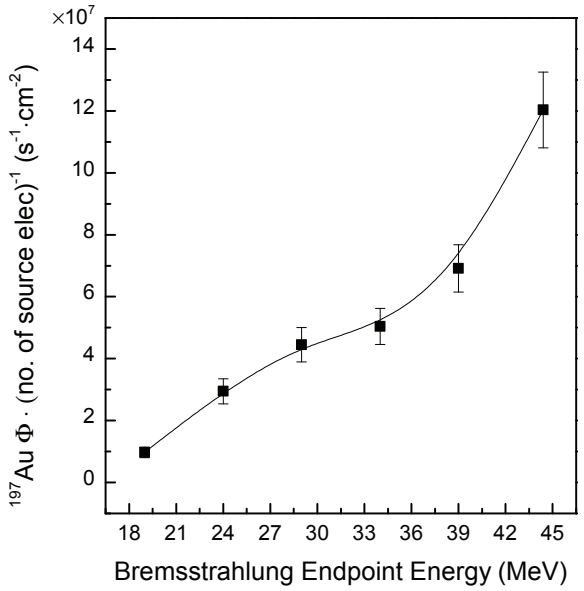

Figure 3.6: Photon flux though gold foil fastened to NaCl target.

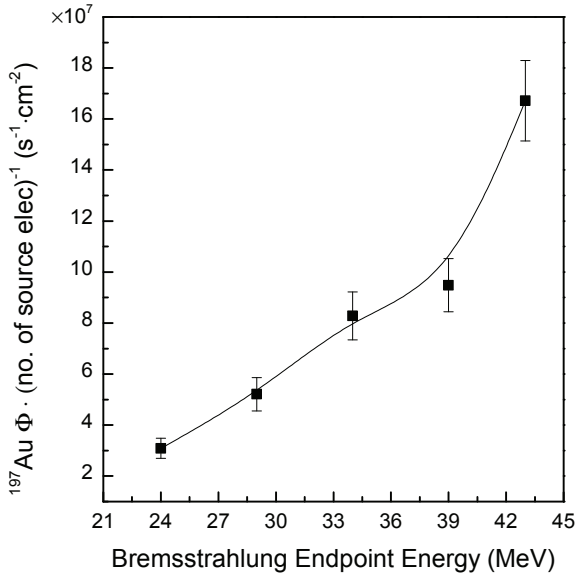

Figure 3.7: Photon flux though gold foil fastened to Ca target.

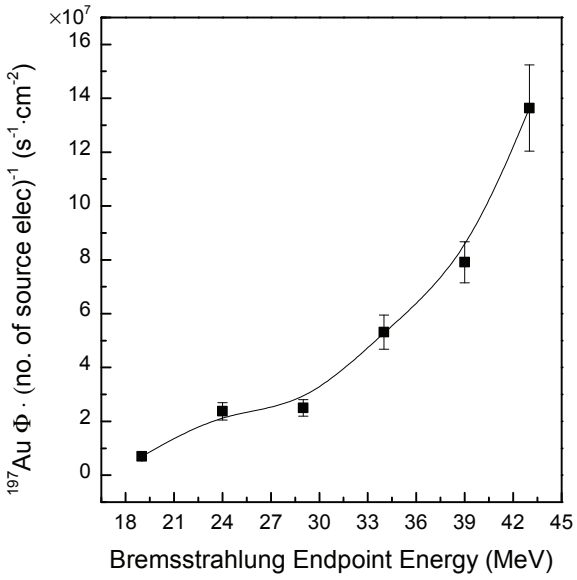

Figure 3.8: Photon flux though gold foil fastened to KBr target.

Chapter 4

Results

4.1 Signature Development

The methodology of defining fission signals was accomplished prior to the research agenda presented here. As mentioned, this work was initiated to investigate the effects of various interferences on fission signals as the bremsstrahlung endpoint energies increased upwards towards 60 MeV. This investigation also offered a means to test the accuracy of fission signals at larger bremsstrahlung energies. The following summary of fission signal development is presented for completeness and to provide clarity on adjustments that were made to account for larger irradiation energies.

Initially, fissionable targets were examined in both passive and active inspection environments with bremsstrahlung photons as the interrogating source of radiation in the active inspections. Figure 4.1a compares the γ-ray energy spectra of a ^{238}U metallic target produced passively and actively. The active spectrum utilized a 15 MeV endpoint energy bremsstrahlung beam and was recorded between bremsstrahlung pulses. The most prominent feature was the low rate of γ-ray emission in the passive inspection at energies greater than ~3 MeV. In contrast, a significant number of high-energy γ-rays (≥ 3 MeV) were observed in the active inspection. These results were consistent for a variety of fission targets when comparing passive to active inspections at differing accelerator energies including those at the maximum operating energy conducted of 45 MeV, although, the rate correspondingly increased with

increasing energy.

The high-energy γ-rays emitted in active inspections are not typically emitted by naturally occurring radioactive materials or from reaction products generated in non-fissionable materials at inducing energies near the giant dipole resonance region typical of fissionable materials. The passive ^{238}U target shown in Figure 4.1a along with a passive no-target (blank) inspection are presented in Figure 4.1b. Similarities in the shape of the ^{238}U and no-target curves illustrate that the ^{238}U passive rate was dominated by γ-rays produced in the environment. The increase in the ^{238}U passive rate over the no-target results from γ-rays generated from fission production that was not deposited in photopeaks via the photoelectric effect (or pair production), but from γ-rays that undergo Compton scattering and dissipate energy in fragments creating a continuum. The continuum is seen most significantly at the low energy end of the spectrum.

Timing information was next examined for both neutrons and γ-rays as illustrated in Figures 4.2a and 4.2b respectively. The Figures show the rate of γ-ray emissions from both the ^{238}U target, constructed from the same data measured and shown in Figure 4.1, and a Pb target. The γ-ray yield, in Figure 4.2b, was integrated over the high-energy γ-rays from 3 to 7.2 MeV. Both graphs show an initial and rapid decrease in the γ-ray yields, however, the Pb signal continues to fall while the ^{238}U yield remains elevated. Elevation of the ^{238}U signal is due to the continual contribution of β delayed γ-rays and neutrons resulting from the de-excitation of fission fragments. After the initial decline, the Pb signal evens out reaching a yield equal to the natural passive background. The time period of this initial decline occurs in ~22 and ~14 ms for γ-rays and neutrons respectively. In the region of the curve just before the decline to the natural passive background, the contribution to the neutron yield is due to neutrons created by the bremsstrahlung pulse, scattering in the environment, and returning to the detectors [19]. A fraction of the neutrons that do not arrive at detectors are absorbed in the target and surrounding environment producing (n,γ) reactions that thereby contribute to the γ-ray yield. At a 45 MeV bremsstrahlung endpoint energy, the rate of decline is extended to ~29 ms and ~19 ms for γ-rays and neutrons respectively. The time extension can be attributed to a larger number of neutrons

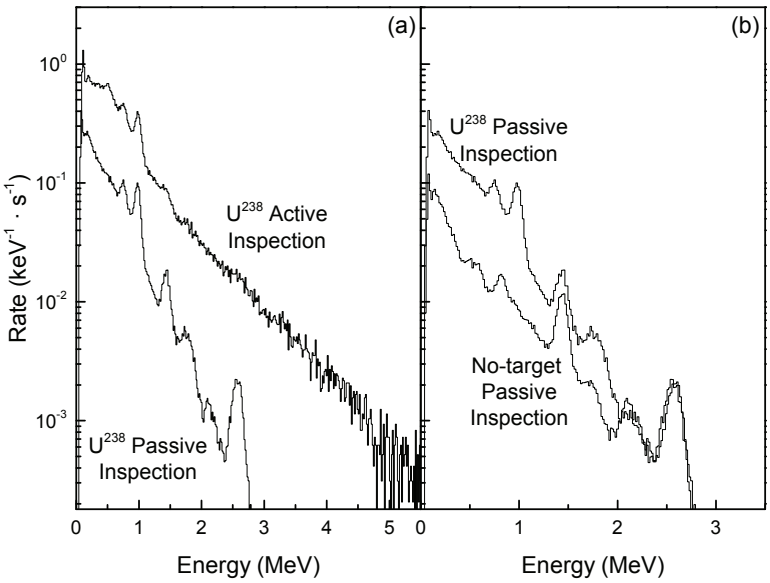

Figure 4.1: Energy spectra of a 205 g ^{238}U metallic target (in-beam mass) detected from passive and active inspection environments (a). The passive ^{238}U spectrum is compared with a passive no-target inspection (b). The 603 s active inspection utilized a 15 Hz pulsed bremsstrahlung beam with an endpoint energy of 15 MeV and an average charge per pulse of 213 nC. Observation times of 5401 and 18009 s were recorded with BGO detectors for the ^{238}U and no-target passive spectra respectively.

and γ-rays produced as a result of the higher accelerator energy utilized. The shape of the time series for targets irradiated at energies beyond 15 MeV is similar to those observed at 15 MeV and below, however, the magnitude of the yield increases with increasing energy and is therefore larger than the natural passive background. The increase in the yield can be attributed to activity within the targets. This activity was minor in the no-target inspections, but more noticeable in targets where interferences were observed. Nevertheless, restricting the signatures to the nearly flat time region would remove the initial burst of neutrons and (n,γ) contributions from the signal; the impact to the yield would be similar to those implemented at energies of 15 MeV and below.

Timing and energy information, determined from Figures 4.1 and 4.2 as well as similar data obtained from various fissionable and non-fissionable materials, provided

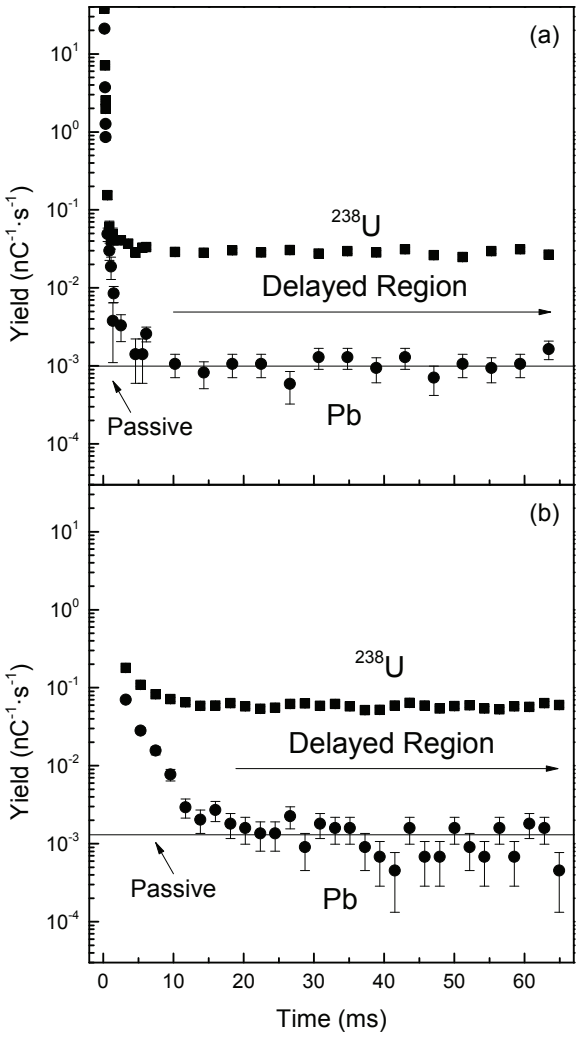

Figure 4.2: Time spectra for neutrons (a) and γ-rays (b) showing 487 g Pb (•) and 205 g ^{238}U (■) targets (in-beam masses) irradiated with a 15 Hz pulsed and 15 MeV endpoint energy bremsstrahlung beam that operated for ~603 s with an average charge per pulse of 222 nC. The Pb yield decreased to the natural passive background (solid) in ~22 and ~14 ms for γ-rays and neutrons respectively. The delayed region (arrow) specifies the energy range dominated by β-decay processes.

a way to differentiate signals from non-fissionable and fissionable materials and thus were used to define the signatures. Energy restrictions limited the range of energy within the γ-ray signature region to encompass events that originate typically from

actively induced fission processes. Time restrictions limit the neutron and γ-ray emission times within the signature region, thereby reducing the signals. The signals decrease by removing the majority of neutrons detected during the accelerator pulse and the resulting γ-rays emitted from (n,γ) reactions. Therefore, the signatures included γ-rays emitted with energies from 3 to 7.2 MeV and detected at times starting 29 ms after the bremsstrahlung pulse and continuing to the next pulse as measured by the BGO detectors. Energy information was not directly provided by the neutron detectors, therefore, timing characteristics comprised the neutron signatures, which were defined as neutrons emitted 19 ms after the pulse and to the next pulse. Note that the HPGe detector provided similar timing spectra, however, the decline from the initial γ-ray contributions created in the non-fissionable materials remains evident until ~20 ms in contrast to the ~29 ms time generated in the BGO detectors. The reduced time span can be attributed to the lower efficiency of the HPGe (80% relative to NaI at 1.33 MeV) detector compared to the BGO (233% relative to NaI at 1.33 MeV for 1.5"×1.5" crystals) detector. The higher Z value and density in the BGO compared to the HPGe detector increases the interaction probability, thereby, extending the time of detection.

4.2 Interferences

4.2.1 15 MeV Dual Phase Space

A clear observance of signal interferences is most effective when first examining detection environments with distinct fission signals free of obstructions. Previous work with targets irradiated at an operating energy of 15 MeV resulted in discernable fission signals, however, only a small number of targets were irradiated. The dual signal phase space of Figure 4.3 shows results of irradiating 42 targets at a 15 MeV bremsstrahlung endpoint energy using a 15 Hz pulsed beam. The dual signal phase space allows for ease in identifying differences between γ-ray and neutron signals. The gross signals are comprised of delayed counts normalized to the electron charge incident on the radiator and the solid angle subtended by the separate detector ar-

rays. Excluding the smallest fission target, consisting of 0.7 g of ^{238}U, a clear division is apparent between fissionable and non-fissionable signals. The division is magnified by the narrow distribution of non-fissionable and no-target inspections that are clustered in the lower left hand corner of the graph. A passive no-target inspection is displayed and lies within one standard deviation of the mean of both the γ-ray and neutron non-fissionable and no-target inspection signals. The narrow distribution of non-fissionable signals clustered around the passive no-target yield reflects their equivalence to the natural passive background. The no-target (blank) inspections were observed at the start and end of each accelerator energy prior to and after irradiating all targets. This allowed for the observance of activity that may have built up during each bremsstrahlung energy cycle. The fission yields begin within the cluster of signals from non-fissionable targets and extend with increasing magnitude fairly linearly in order of increasing mass relative to equivalent isotope with slight deviations likely produced from self absorption.

The regions on the graph that delineate background yields and their associated uncertainty and consequently the undetectable regions are outlined on the graph by the two-dimensional "And" and "Or" critical decision levels, L_c. The "And" and "Or" L_cs are determined by Equations 2.41 and 2.42 respectively. The passive component of L_c was calculated using not only the passive no-target, but also includes the non-fissionable and active no-target samples. The equivalence of the non-fissionable and active no-target signals to the natural passive background warrants their inclusion into the passive component. At 15 MeV, the active component was zero. The false positive confidence level, α, is set at 1% for the curves shown. The "Or" L_c encloses the region at the lower left hand corner of the graph. The smallest fission target with 0.7 g of ^{238}U lies within the "Or" L_c region and therefore can not be discriminated from the background. The remaining 11 fission targets lie within the detectable region. The "And" L_c outlines a larger region where fissionable materials can not be detected. The region is similar to the "Or" region but is extended to include the upper left hand and lower right hand corners producing an "L" shape in the graph. The "And" L_c region encloses an additional fission target leaving 10 targets in the detectable region. At the 15 MeV bremsstrahlung endpoint energy, the "Or" L_c

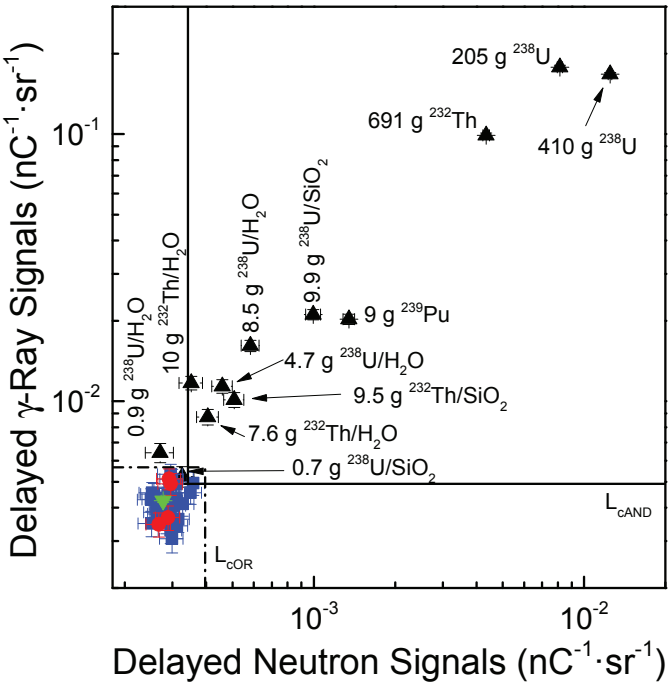

Figure 4.3: Dual signal phase space with fission (▲), non-fission (■), no-target active (●) and passive (▼) inspections. Active inspections utilized a 15 MeV endpoint energy bremsstrahlung beam operating at a 15 Hz repetition rate. An average charge per pulse of 227 nC was recorded over 9102 pulses averaged from all active inspections. The two-dimensional "And" (solid) and "Or" (dot-dashed) critical decision levels define the detectable region. In-beam masses are listed.

allows for the detection of more fissionable materials and is therefore the appropriate detection algorithm.

Along with the "Or" L_c shown in Figure 4.3, Figure 4.4 displays the two-dimensional "Or" minimal detection level, L_d, where equation 2.48 is applied. A charge of 150 nC averaged over 9000 pulses and a detector solid angle of 0.159 sr (neutrons) or 0.012 sr (γ-rays) was assumed for the planned detection system and calculation of L_d along with a false negative probability, β, of 1%. Within the "Or" L_d curve, and beyond the "Or" L_c, lies the second smallest ^{238}U target. The 0.902 g ^{238}U target contains insufficient fissioning material for its mean yield to equal or surpass L_d. In other words, while the target is in the detectable region it will be detected less than 99% of the time

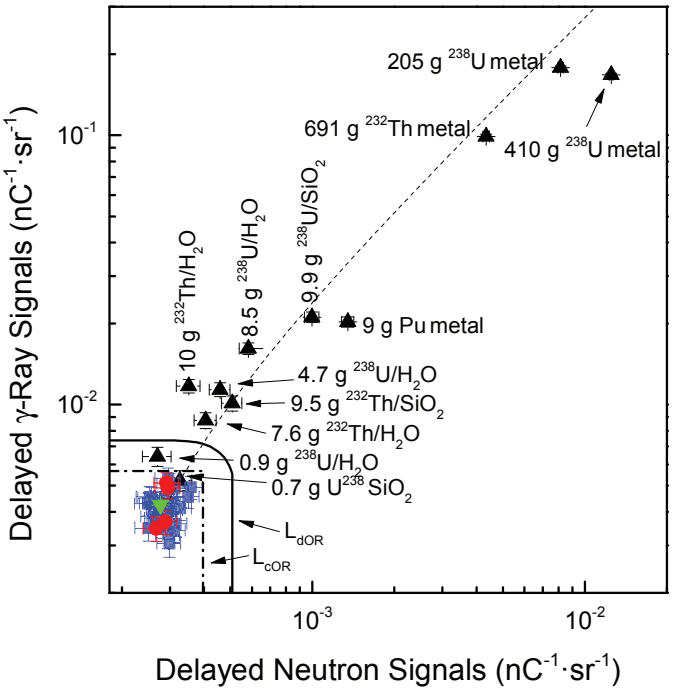

Figure 4.4: Dual signal phase space with fission (▲), non-fission (■), no-target active (●) and passive (▼) samples displayed. Experimental parameters match those described in Figure 4.3. The two-dimensional "Or" critical decision level (dot-dashed) is displayed along with the "Or" minimal detection limit (solid). A mass parameter (dashed) line aids in determining the minimum detectable mass. In-beam masses are listed.

under the confidence level specified. The minimal detection level is used to calculate the minimal detectable mass, M_{min}. As described in section 2.5, the intersection of L_d with a line that parameterizes the fission signals to relative fission mass specifies the M_{min}. The line can be seen on the graph emerging from the non-fissionable materials and extending towards the fissionable targets. The parametric equation was constructed from the low mass γ-ray and neutron fission signals separately as a function of fission mass. A linear fit on the data was applied, however, the intercept was manually set to the zero fission mass point determined from the mean yield of the non-fissionable and no-target inspections. Intersection of the parametric line with "Or" L_d gives an M_{min} of $3.14 \pm 1.31 \times 10^{-2}$ g. In comparison, a one-dimensional L_d algorithm

yields M_{min} values of $3.19 \pm 1.36 \times 10^{-2}$ and $6.41 \pm 1.28 \times 10^{-4}$ g for γ-rays and neutrons respectively. The two-dimensional L_d is 1.6% lower than the one-dimensional γ-ray L_d and differs by 68% over the neutron L_d. Differences between the two-dimensional and one-dimensional L_ds show that the γ-ray signals independently provide more to the sensitivity of the detection system than the neutrons. These differences stem from the larger yield that results from a greater quantity of delayed γ-rays emitted and detected per fission fragment relative to the number of delayed neutrons. One way to overcome this difference would be to augment the neutron detection surface area by increasing the number and/or size of neutron detectors relative to γ-ray detectors.

4.2.2 22.5 MeV Dual Phase Space

The picture changes considerably when examining the fission signals at 22.5 MeV as shown in Figure 4.5. The emergence of interferences, evident by the non-fission signals that exceed numerous fission yields, is readily observed at the larger bremsstrahlung endpoint energy. Similarly to the 15 MeV data, the fission signals increase fairly linearly in order of increasing mass albeit with a larger yield, however, the non-fission signals begin to diverge from and many are no longer statistically equivalent to the natural passive background. The no-target inspections are statistically equal to within one standard deviation of the passive background for γ-rays, however, the neutron signals deviate somewhat indicating activity in the background. The mean of the no-target inspections is 1.1 times larger than the passive yield with this activity included in the active component of the neutron L_c calculation. All fission targets lie in the detectable region when utilizing either "And" or "Or" L_cs, however, 17 non-fission targets are also in the "Or" detectable region and 7 are in the "And" detectable region. The non-fissionable materials in the detectable regions would present as false positives and therefore interfere with the fission signals.

Of the 7 non-fissionable targets lying in the "And" detection region, 5 (beef, concrete, ^{18}O, salt water tube, and deionized water tube) contain oxygen. The largest interference was observed in the ^{18}O-enriched water target, therefore the decay from ^{18}O products were assumed to have the largest contribution. Figure 4.6a shows dis-

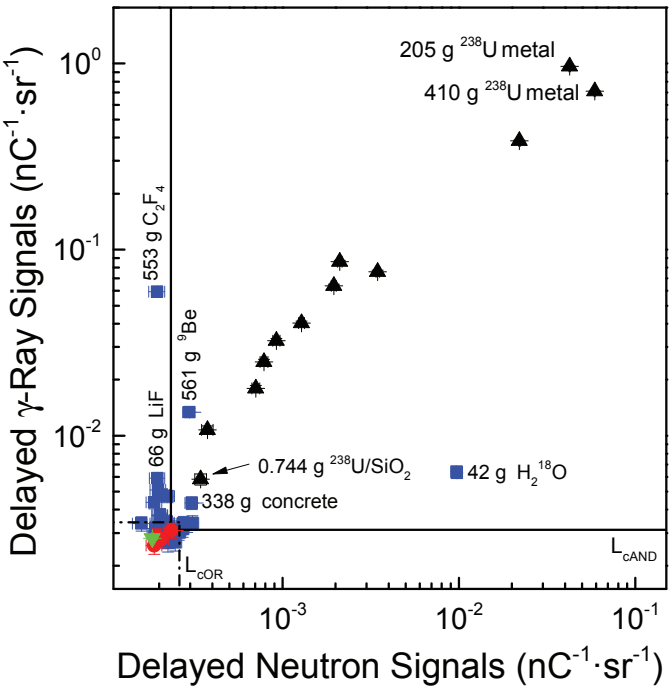

Figure 4.5: Dual signal phase space displaying targets irradiated with a 22.5 MeV endpoint energy bremsstrahlung beam pulsed at 15 Hz for an average of 9050 pulses. The average charge per pulse was 341 nC for all fission (▲), non-fission (■), and active no-target (●) samples. A passive no-target (▼) inspection is also shown and normalized to the active parameters averaged. Two-dimensional logical "Or" (dot-dashed) and "And" (solid) L_c limits are defined. In-beam masses for fission signals include only the fissioning isotope while the non-fission signals include the total mass of the compound or element.

crete γ-ray peaks that contribute direct interferences within the γ-ray signature at 6128.6 and 7115.2 keV. These peaks result from the decay of ^{16}N produced from the photodisintegration of ^{18}O. Two reactions result in the production of ^{16}N with ^{18}O as the parent. The (γ,d) reaction has an energy threshold of 19.6 MeV and the (γ,np) reaction has a threshold of 21.8 MeV making both reactions probable at 22.5 MeV [39]. Nitrogen-16 β^- decays with a half-life of 7.13 s with branching ratios from the 6128.6 keV and 7115.2 keV being 67% and 4.9% respectively [40, 41, 105]. While the peaks were detected in the 22.5 MeV data for the ^{18}O target, they were

more readily observed at a bremsstrahlung endpoint energy of 45 MeV, therefore, for ease of display the ^{18}O graph was constructed from 45 MeV data.

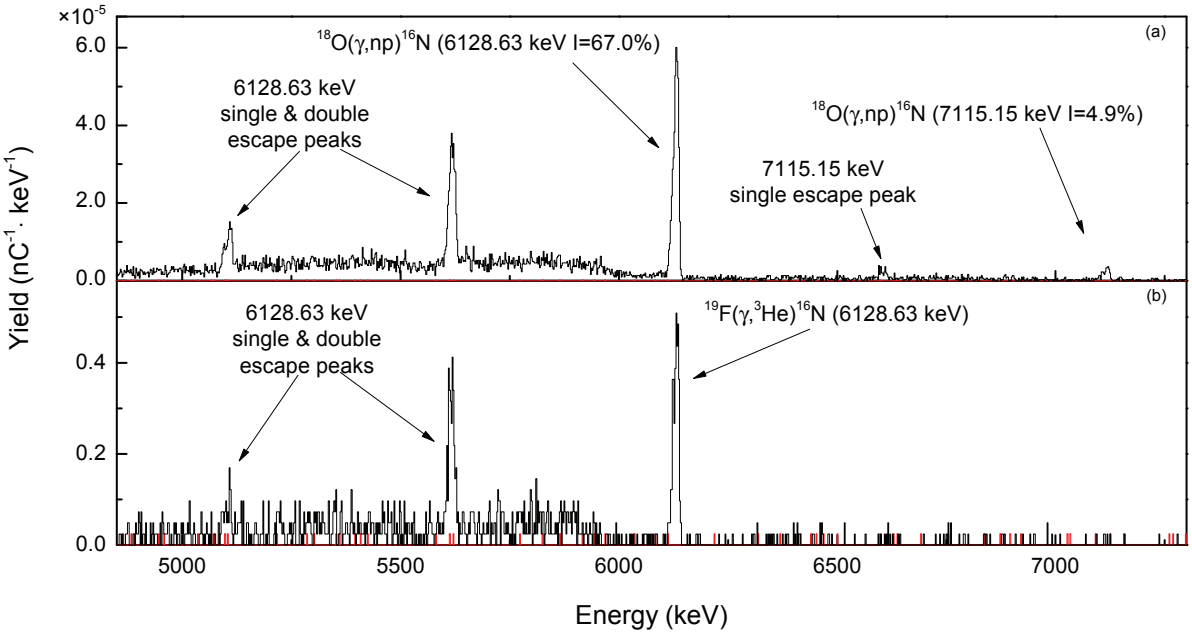

Figure 4.6: Energy spectra with 6128.6 keV and 7115.2 keV photopeaks from the decay of ^{16}N produced by ^{18}O (black) (a) and LiF (black) (b) samples. Both spectra are compared with a no-target (red) inspection. An irradiation endpoint energy of 45 MeV was produced by a 15 Hz pulsed bremsstrahlung beam with an average electron charge of 53 nC averaged over 33822 pulses. A HPGe detector was utilized to produce the spectra from in-beam masses of 42 and 66 g of ^{18}O and LiF respectively.

The elevated neutron yield in the oxygen containing targets results from delayed neutrons emitted following the β^- decay of ^{17}N (4.17 s half-life) produced from the ^{18}O(γ,p)^{17}N reaction [40, 41, 51, 91, 106, 107]. The 870.7 keV photopeak resulting from the β^- decay of ^{17}N, and displayed in Figure 4.7a, does not fall within the γ-ray signature region, however, it is an indication that the reaction has occurred [40, 108]. Further evidence of ^{17}N production and its subsequent delayed neutron emission is illustrated in Figure 4.7b. The figure shows that the yields for the no-target inspections irradiated at 15 and 19 MeV and for the ^{18}O target irradiated at 15 MeV are statistically equivalent to the natural passive background which is

consistent with a reaction that has a threshold of 15.9 MeV [39]. The yields for the ^{18}O-enriched water target irradiated at 19 and 45 MeV are increased, due to reaction activity, one order and three orders of magnitude respectively over the 15 MeV data. The data presented in the neutron time spectra of Figure 4.7b were obtained from experiments performed at different times (April and August 2012) and while care was taken to set up similar experimental conditions the data was scaled to account for slight differences in the passive backgrounds. Scaling was accomplished by subtracting the relative passive background from the gross yield leaving a net yield. An average passive background calculated from both experiments was then added back to the net yields to produce the displayed scaled gross yields.

In addition to the 870.7 keV peak shown in Figure 4.7a, an 834 keV decay peak was observed in both the no-target active and passive inspections. The observance of the peak in the passive inspection indicates activity from a relatively longer-lived radionuclide. The main experiment table is constructed from steel and also contains screws and bolts containing iron. Stable ^{55}Mn is a common alloy of iron and following a (γ,n) reaction, ^{54}Mn decays with a 312.3 d half-life [40, 41]. The ^{55}Mn(γ,n)^{54}Mn reaction has a 10.2 MeV energy threshold and is the probable cause of the 834 keV line, however, the production of ^{54}Mn likely occurred during a prior experiment [39]. An 843 keV decay peak was also observed in the ^{18}O graph and was noted in many, but not all of the targets irradiated. The peak was not observed in the no-target active or passive inspections and was strongest in the aluminium lump target. This suggests that the aluminum stand used to raise some of the targets to the correct height likely produced the reaction causing the 843 keV peak. The most probable reaction occurs in magnesium which is often an alloying component of aluminum. Magnesium-27 decays with a 9.5 m half-life and is produced by the ^{26}Mg(n,g)^{27}Mg reaction [40, 41].

Furthermore, both ^{16}N and ^{17}N decay via β-particles with their resulting interactions contributing to the γ-ray signatures. The β-particles with the largest endpoint energies are 10.4 (28% branching ratio) and 8.7 MeV (1.6% branching ratio) for ^{16}N and ^{17}N respectively [40, 41]. Despite the fact that ^{18}O has a low isotopic abundance (0.2%), the large percentage of oxygen in the earth's crust (46.6%), in sea water

(85.9%), and in the terrestrial atmosphere (21.0%) present a significant concern for interferences [50, 109–111]. Note that the ^{17}O(γ,p)^{16}N reaction has a threshold of 13.8 MeV, however, evidence of the reaction was not observed at 15 MeV. The low isotopic abundance, 3.8×10^{-2}%, of ^{17}O would make contributions from its decay to the γ-ray signal minimal.

Mitigation of interferences produced from oxygen containing targets would require implementing an algorithm to indicate the presence of the 6128.6 keV and 7115.2 keV decay peaks at the 22.5 MeV bremsstrahlung endpoint energy. If the targets containing oxygen were the only concern, implementing the procedure would be minimal. However, if interferences arising from additional decay products were also of interest, a database listing and testing for individual peaks would be required for mitigation.

The two remaining interferences in the "And" detection region are produced from ^{9}Be and Pb. The elevated γ-ray yield in the ^{9}Be target results from the ^{9}Be(γ,p)^{8}Li reaction that occurs at a threshold energy of 16.9 MeV [39, 52]. The ^{8}Li product β^- decays with a 0.838 s half-life and while it does not emit discrete γ-rays with energies within the signature region, a β-particle with an endpoint energy of 13.0 MeV is emitted [40, 41, 112, 113]. The β-particle loses energy through interactions within the target, surrounding environment, and the detector producing bremsstrahlung photons. Figure 4.8 shows a curve from the ^{9}Be target observed by the BGO detectors that is typical of a bremsstrahlung spectrum. At 22.5 MeV the bremsstrahlung distribution is evident, however, the curve is more appreciable in the 37.5 MeV data and is therefore displayed. While delayed neutrons are not a product of decay in the ^{9}Be target, some of the bremsstrahlung photons likely have energies large enough to produce ^{9}Be(γ,n)^{8}Be reactions (1664.7 keV threshold) increasing the neutron yield through secondary emissions [39]. The reactions responsible for the elevated signals in Pb are not readily apparent. All discrete energy peaks observed are below the 3 MeV signature region for γ-rays. The only observed peaks exclusive to Pb, 703.2 and 987.5 keV, result from the decay of ^{205m}Pb which has a 5.55 ms half-life [40, 41]. The ^{206}Pb(γ,n)^{205m}Pb reaction has a threshold of 8.1 MeV peaking at 13.5 MeV with a 0.63 b cross-section [39–41, 114]. No β-particles were noted with energies greater than 3 MeV.

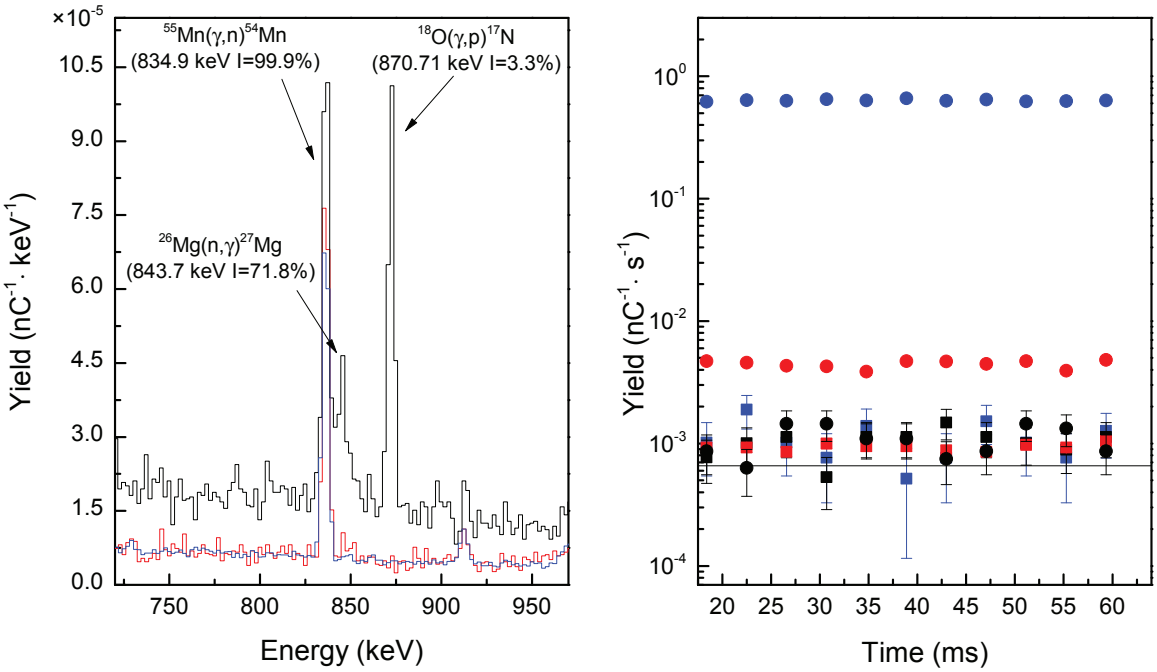

Figure 4.7: Photon energy (a) and neutron time (b) spectra resulting from the decay of ^{17}N following the ^{18}O(γ,p) reaction produced in the ^{18}O-enriched water target (42 g in-beam mass). The 870 keV ^{17}N photopeak (black) in (a) is compared with no-target active (red) and passive (blue) inspections where the active inspections were performed for ~32291 pulses at an average charge per pulse of 52 nC and a 45 MeV endpoint energy bremsstrahlung beam. The 16176 s passive sample was normalized to the active inspection parameters. The time spectra shows the ^{18}O (•) and no-target (■) inspections irradiated at bremsstrahlung endpoint energies of 45 (blue), 19 (red), and 15 MeV (black). Average charge and pulses for inspections were 218 nC and 23336 respectively. Inspections at 15 and 19 MeV, excluding ^{18}O, level to the natural passive background (black).

Although conditions free of ^{9}Be, Pb, and oxygen containing materials are not likely, the M_{min} was determined without interferences by taking the point of intersection between the "And" L_d and the mass parametrization line displayed in Figure 4.9. The detection system is assumed to have the same parameters noted in the 15 MeV data. The "And" M_{min} is $2.2 \times 10^{-1} \pm 2.3 \times 10^{-4}$ g, calculated without in-

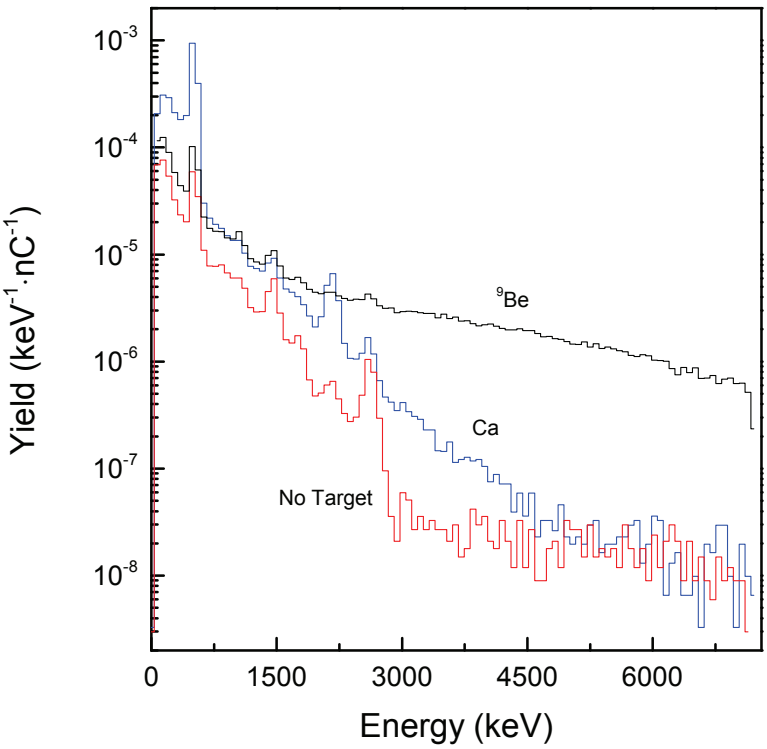

Figure 4.8: Energy spectra with ^{9}Be (black), Ca (blue), and no-target (red) inspections irradiated by a 37 MeV endpoint energy 15 Hz pulsed bremsstrahlung beam. The average charge per pulse was 173 nC averaged over 28931 pulses. The spectra was observed from the BGO detectors.

terfering signals. The two-dimensional L_d comes with a 45% loss in sensitivity from the one-dimensional γ-ray L_d, however, a gain of 40% is achieved over the neutron L_d. The addition of neutrons in the detection system comes with a significant loss in sensitivity. The loss in sensitivity is compounded not only by the lower quantity of delayed neutrons emitted per fission fragment, but also by the increase in neutron background activity as compared with the γ-ray background.

4.2.3 30 MeV Dual Phase Space

Reliability of fission signals drastically declines due to the presence of interferences at 30 MeV as illustrated in Figure 4.10. The fission signals again increase fairly linearly in order of increasing mass and equivalent isotope, however, the non-fissionable

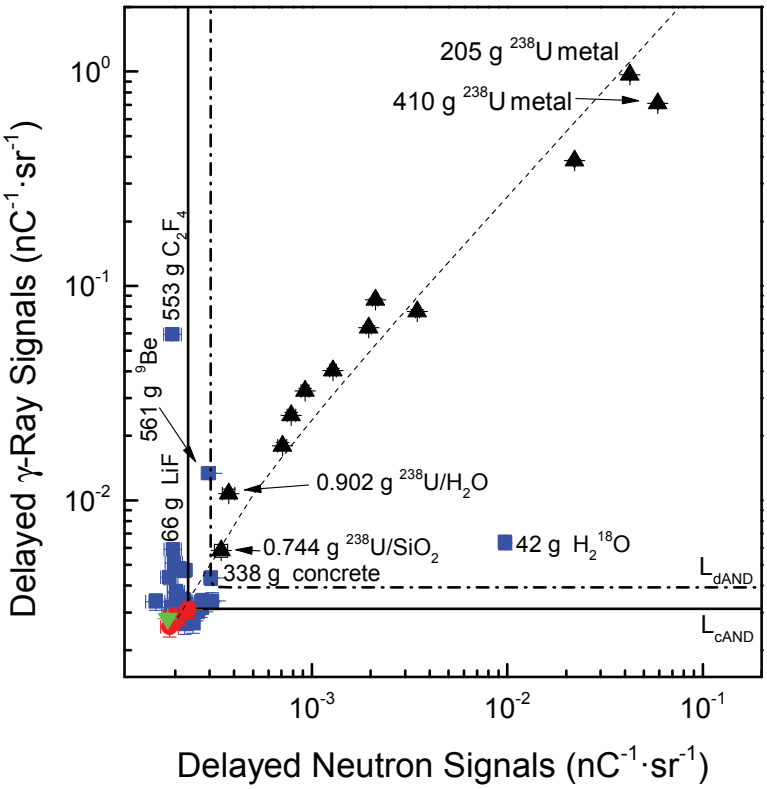

Figure 4.9: Dual signal phase space showing targets irradiated with a 22.5 MeV end-point energy bremsstrahlung beam pulsed at a 15 Hz repetition rate. All parameters are equivalent to those described in Figure 4.5. The mass parameter (dashed) and "And" L_d (dot-dashed) are also displayed.

and no-target inspections deviate significantly from the natural passive background. Environmental activation is apparent by the clear deviation of no-target samples from the passive inspection. The mean yield of the no-target inspections for neutrons and γ-rays increases to 1.4 and 1.1 times respectively over the passive background signifying background activity. The active background, determined from the no-target inspections, is included in the "Or" and "And" L_c calculations. The direct cause of the background activation is unclear. The no-target energy spectra does not contain discrete peaks or obvious β-particles within the γ-ray signature region, however, the experimental room does contain oxygen in the concrete and atmosphere which is likely contributing to the background activation. Unlike the signals measured at 15

and 22.5 MeV, 100% of the non-fissionable signals at 30 MeV lie in the "Or" and 50% lie in the "And" detection regions. Among the signals in the "And" detection region, those containing fluorine (LiF, C_2F_4, and KF) produce ^{16}N and ^{17}N reaction products with decay characteristics specified in the discussion for ^{18}O. The ^{19}F(γ,^{3}He)^{16}N, ^{19}F(γ,dp)^{16}N, ^{19}F(γ,n2p)^{16}N, and ^{19}F(γ,2p)^{17}N have reaction thresholds of 22.1, 27.6, 29.8, and 23.9 MeV respectively [39, 75]. Decay peaks from ^{16}N and ^{17}N are displayed in Figures 4.6, A.2.20, and A.2.33 respectively for LiF, KF, and C_2F_4. Discrete γ-rays from the decay of ^{17}N in the LiF target were not observed, however, the neutron yield does increase and is shown in Figure A.2.5. As mentioned, both ^{16}N and ^{17}N decay via β-particle emission. A typical bremsstrahlung curve is not obvious, however, energy spectra observed from the BGO detectors for the C_2F_4 and LiF targets are displayed in Figures A.2.34 and A.2.4 respectively. A bremsstrahlung curve for KF is not evident and hence not included.

4.2.4 37.5 MeV Dual Phase Space

The distribution between non-fission signals continues to widen as does their deviation from the natural passive background as the bremsstrahlung endpoint energy is increased to 37.5 MeV as shown in Figure 4.11. Yields from many non-fissionable materials cloud the fission signals. Neutrons from ^{18}O overwhelm all signals except the largest (409.8 g) ^{238}U target. The γ-ray signal from ^{18}O surpasses all but the largest three fission targets (409.8 g ^{238}U, 204.9 g ^{238}U, and 690.5 g ^{232}Th). The gap between the active and passive no-target inspections expands to ~2.0 times for neutrons and ~1.2 times for γ-rays. Background activation measured from the active no-target inspections is included in the L_c calculations for the "Or" and "And" detection regions shown. Oxygen-18 continues to contribute markedly in many of the oxygen containing targets such as deionized water, salt water, watermelon, beef, SiO_2, wood, and concrete with the 6128.6 keV photopeak from the decay of ^{16}N appearing in Figures A.2.6, A.2.10, A.2.11, A.2.12, A.2.13, A.2.15, and A.2.35 resptectively. Along with the oxygen reactions mentioned, the ^{16}O(γ,2n)^{14}O reaction with a 28.9 MeV threshold is observed in the concrete, SiO_2, salt and deionized water targets [39].

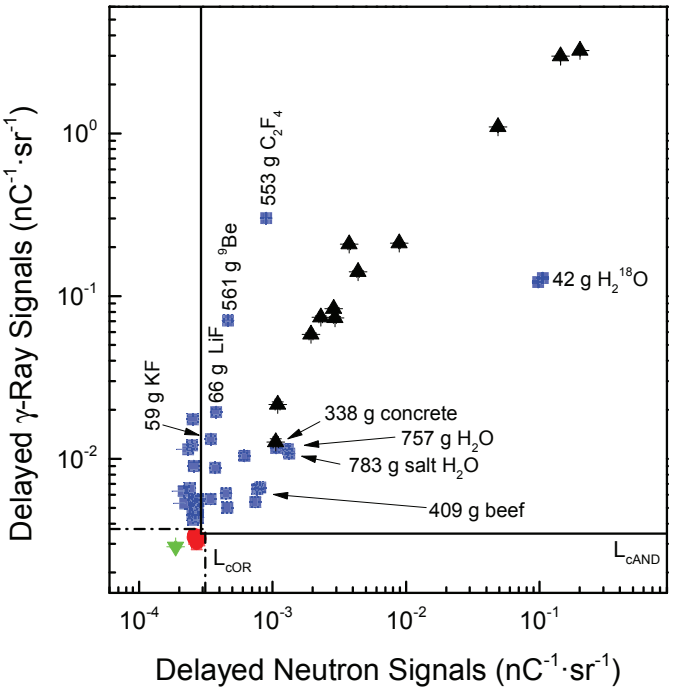

Figure 4.10: Dual signal phase space with fission (▲), non-fission (■), and no-target (●) inspections irradiated at a bremsstrahlung endpoint energy of 30 MeV. Active parameters were used to normalize the passive no-target (▼) which include a charge per pulse of 335 nC averaged over 9081 pulses. The two-dimensional "And" (solid) and "Or" (dot-dashed) critical decision levels define the undetectable regions. Masses listed are in-beam compound masses.

Energy deposited within the signature region is due to a 3947.5 keV γ-ray (intensity of 2.1×10^{-3}%) and bremsstrahlung photons produced following interactions with a 5143.0 keV endpoint energy β-particle (intensity of 0.6%) [39–41]. Evidence of reaction production is seen from the 2312.6 keV decay peak (99.4% intensity) illustrated in Figures A.2.7, A.2.10, A.2.14, and A.2.36.

In addition, the signals from materials containing NaCl are increased by a discrete γ-ray within the signature region with energy of 3304.0 keV (12.3% intensity) [40,41]. Emission of the γ-ray follows the β^+ decay of ^{34m}Cl (1920 s half-life) produced from the ^{35}Cl(γ,n) reaction (12.8 MeV threshold) [39–41]. The reaction also produces a 3150.1 keV β^+ particle (28.5% branching ratio) [40,41]. The signals increase as γ-rays

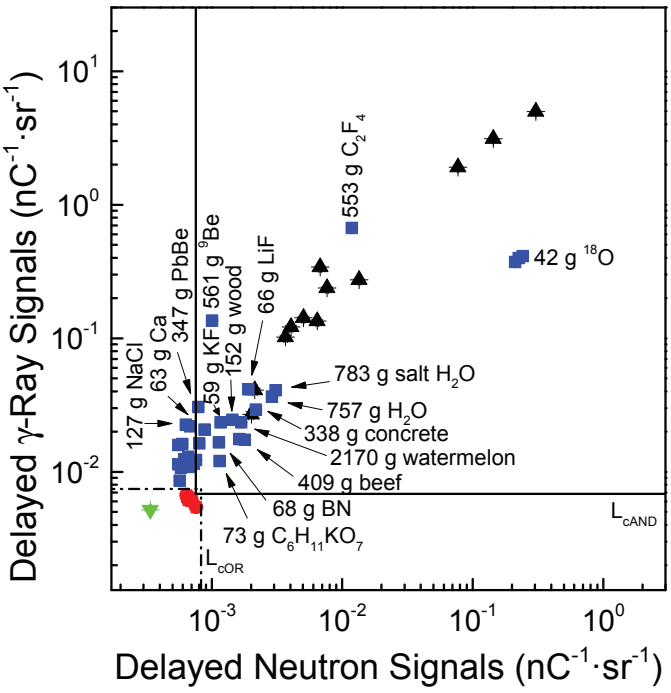

Figure 4.11: Dual signal phase space with fission (▲), non-fission (■), and no-target (●) samples irradiated at a bremsstrahlung endpoint energy of 37.5 MeV. A passive no-target (▼) is normalized to the active inspection parameters which include a charge per pulse of 185 nC averaged over 9047 pulses. All fission targets are within the L_c logical "AND" (solid) and "OR" (dot-dashed) detectable regions. Masses listed are in-beam compound masses.

are emitted following excitations that result from positron interactions with electrons occurring prior to annihilation. The 3304.0 keV photopeak produced in the salt water target appears in Figure A.2.9. The 3304.0 keV photopeak is also produced in the NaCl energy spectrum and shown in Figure 4.12 with the target irradiated at a bremsstrahlung endpoint energy of 45 MeV. Several additional peaks are also displayed in the energy spectrum: the 2127.5 keV photopeak, the 1176.6 keV photopeak, and related single escape peaks from the ^{35}Cl(γ,n) reaction. Furthermore, a 1634.0 keV photopeak resulting from the decay of ^{20}F following the photodisintegration of ^{23}Na is also observed [40, 41]. The ^{23}Na(γ,^{3}He)^{20}F reaction has an energy threshold of 24.5 MeV [39]. Fluorine-20 β^- decays (11.2 s half-life) adding energy to the signature

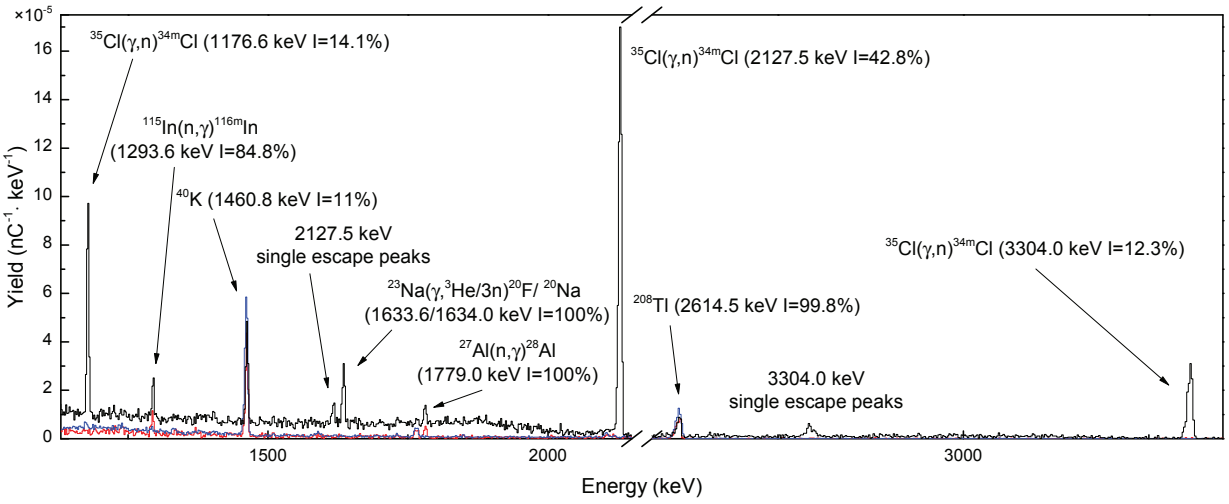

Figure 4.12: Energy spectrum with peaks from the decay of ^{34m}Cl and ^{20}F produced in 127 g (in-beam mass) of NaCl (black). No-target active (red) and passive (blue) spectra are normalized to a charge per pulse of 54 nC averaged over 38047 pulses produced by an accelerator operating at 45 MeV.

region from 3332.5 keV and 4965.9 keV γ-rays and bremsstrahlung photons created from β-particles with 5390.9 and 7024.3 keV endpoint energies and branching ratios of 8.2×10^{-3}, 5×10^{-5}, 100, and 5×10^{-4}% respectively [40,41]. As the energy increases beyond ~40 MeV the ^{23}Na(γ,3n)^{20}Na reaction is also probable and adds energy to the γ-ray signature largely from β^+ particles [39]. Sodium-20 has a 0.47 s half-life and the maximum endpoint energy β-particle (79.5% branching) has an endpoint energy of 12.3 MeV [74]. The total branching ratio above 3 MeV is 100% and 0.3% for β-particles and discrete γ-rays respectively [74].

Furthermore, the graph shows several environmental background peaks. The 1460.8 and 2614.5 keV peaks are observed in both the passive and active no-target samples. The 1460.8 keV peak results from the decay of ^{40}K originating from concrete in the walls of the experimental room and is commonly found in background spectra. Potassium-40 has a decay half-life of 1.3×10^9 years [40,41]. The 2614.5 keV peak (99.8% branching) results from the decay of ^{208}Tl. Thallium-208 (3.1 m half-life) is a decay product in the ^{232}Th decay chain [40,41]. Thorium-232 is found in dirt and concrete and the 2614.5 keV peak is also commonly found in background

spectra. Additionally, while not observed in the passive inspections, the 1293.6 keV and 1779.0 keV peaks are present in the active no-target inspections. The 1293.6 keV γ-rays are the product of the ^{115}In(γ,n)^{116m}In reaction produced in the HPGe detector. Indium is used for low temperature solders and in cryogenic applications. Additionally, aluminum was used frequently and inconsistently in the experiment as a platform to hold many of the targets. The platform remained during some of the active no-target inspections. Reactions from the decay of ^{28}Al resulting from ^{27}Al(n,γ) are likely the cause of the 1779.0 keV decay peak [40, 41]. The background peaks do not contribute energy to the signatures, but are included here for completeness.

The concrete target produces photonuclear reactions that contribute to the increase in the γ-ray signal. The ^{40}Ca(γ,np)$^{38/38m}$K (21.4/21.5 MeV threshold) reactions produced in concrete as well as in the calcium target contribute energy to the γ-ray signals following β^+ decay of the daughter product [39–41, 71]. Note that the ^{40}Ca(γ,d) reaction also produces both $^{38/38m}$K with the lowest threshold energy at 19.2 MeV [39]. The β-particles emitted with energies in the signature region from ^{38}K have endpoint energies of 3746.4 and 5913.9 keV with branching ratios of 99.9% and 0.05% respectively. A 6044.3 keV endpoint energy β-particle with a 100% branching ratio is produced from the decay of ^{38m}K. Evidence of the reaction is presented in Figures A.2.3 and A.2.36 for the calcium and concrete targets respectively. The 2167.5 keV peak, displayed in the figures, has a branching ratio of 99.9% and is therefore more easily observed than the 3935.6 keV γ-ray (branching ratio 0.14%) produced from the decay of ^{38}K [40, 41]. Furthermore, both the ^{40}Ca(γ,n)^{39}Ca and ^{40}Ca(γ,2n)^{38}Ca reactions result in the β^+ decay of $^{38/39}$Ca (half-life 440 ms/859.6 ms) producing several β-particles with energies in the γ-ray signature region [40, 41]. The branching ratio above 3 MeV equals 99.8% with the branching ratio from the largest energy β-particle (6611.9 keV) equalling 76.5% emitted from ^{38}Ca. Calcium-39 decays emitting a maximum endpoint energy β-particle of 6532.6 MeV with a 100% branching ratio [39]. The energy thresholds for the ^{40}Ca(γ,n) and ^{40}Ca(γ,2n) reactions are 15.6 MeV and 28.9 MeV respectively [39]. Moreover, ^{40}Ca is the most abundant isotope (96.9%) and calcium is the fifth most abundant element in the earth's crust [109, 110, 115]. Along with the reactions mentioned, four additional reactions

listed in Table 2.2 produce β-particles that likely contribute to the γ-ray signature. Figure 4.8 shows an increase in the γ-ray yield observed in the BGO detectors from the Ca target.

Reactions produced in concrete and other targets containing potassium are also evident at 37.5 MeV and appear in the energy spectra of Figures A.2.18, A.2.19, A.2.20, and A.2.36 for KBr, $C_6H_{11}KO_7$, KF, and concrete respectively. The β^+ decay of ^{38}K (458.2 s half-life) resulting from $^{39/40/41}$K(γ,n/2n/3n) reactions have reaction thresholds of 13.1, 20.9, and 31.0 MeV respectively. The likely increase the γ-ray target yields are due to β-particles emitted with energies of 3746.3 (99.8% branching ratio) and 5913.9 keV (0.05% branching ratio) [39–41, 75, 84]. Decay characteristics of ^{38}K are discussed perviously as are the background peaks observed in the KBr target and displayed in Figure A.2.18.

Other materials that emit energies observed in the signature region include argon, sulfur, and zirconium. The argon target produces the ^{40}Ar(γ,^{3}He)^{37}S reaction that has a 23.1 MeV threshold and emits a 3103.4 keV (94.0% branching ratio) γ-ray in the signature region [39–41]. Sulfur-37 decays via the β^- process and has a 5.1 m half-life also emitting a 4865.1 keV (5.6% branching ratio) β-particle [39–41, 75]. Figure A.2.2 shows the 3103.4 keV photopeak.

Sulfur-31 (2.6 s half-life) decays via the β^+ process following the $^{32/33/34}$S(γ,n/2n/3n)^{31}S reactions produced in the sulfur target [40, 41]. Two observed photopeaks indicate reaction activity and are displayed in Figures A.2.25 and A.2.26. Longer irradiation times were performed during an alternate experiment to those producing the dual signal phase space plots, therefore, the figures display the energy spectrum for sulfur irradiated at 39 MeV. The 1266.2 keV peak with a 1.2% branching ratio is presented in Figure A.2.25 [40, 41]. Several background peaks were also observed including a 1063.7 keV (88.3% branching ratio) peak most likely produced in Pb utilized as shielding during the experiment. The ^{208}Pb(γ,n) reaction is followed by the decay of ^{207m}Pb (806 ms half-life) which has a threshold of 5.7 MeV [39–41]. Additional peaks result from indium. As mentioned, indium is used for making thermal connections, in cryogenic applications, and in low temperature solders. The ^{115}In(n,γ)^{116m}In reaction (127.3 keV threshold) produces a 1293.6 keV photopeak from the decay of ^{116m}In and

is discussed above [39–41].

In addition, ^{31}S emits a 3134.1 keV γ-ray within the signature region 0.04% of the time [40,41]. The photopeak is displayed in Figure A.2.26a. The $^{32/33/34}$S(γ,n/2n/3n)^{31}S cross-sections, with reaction thresholds of 15.0, 23.7, and 35.1 MeV respectively, displayed in Figure A.2.26b were obtained from the ENDF/B-VII.1 Radioactive Decay Data File [39–41]. Cross-section integration to 39 MeV weighted to the isotopic abundances reveals that 99.99% of the peak yield is produced from the ^{32}S(γ,n)^{31}S reaction.

Emission of a 3576.0 keV γ-ray, with a 6.4% branching ratio, was observed in the Zr target and is displayed in the energy spectrum of Figure A.2.32. The β^- decay of ^{95}Y (10.3 m half-life) follows the ^{96}Zr(γ,p)^{95}Y reaction beyond an 11.5 MeV threshold energy. The β-decay process also results in several β-particles depositing energy into the signature region with the largest magnitude energy being 4450.0 keV emitted 64% of the time [39–41].

Table A.1, in the appendix, lists all observed reactions and page numbers referencing relevant graphs including several that were not discussed in this section. Reactions that were not discussed produce minor contributions to the signature regions. Graphs that display decay peaks below 3 MeV were included in cases where branching ratios for those above 3 MeV were insufficient to produce observable peaks in the time frame examined.

4.3 Measured Integral Yields

The previous section detailed reactions that produce interferences with the fission signals; the magnitude and number of these interferences increase with higher bremsstrahlung energy. The strength of an interference is not only dictated by the elemental abundance in the earth's crust and atmosphere, the isotopic abundance, the half-life of the decaying isotope, the branching ratio with energy above 3 MeV (γ-ray interference), but also by the probability of reaction occurrence which is measured by the production cross section. This section compares measured integral yields of several reactions, mentioned in the previous section, whose decay products produce

interfering signals with the fission signals. The measured integral yields are compared with simulated calculations to investigate the agreement or dissimilarity in signals. Evidence is gleaned on the challenges associated with modeling interfering signals as an alternative approach to performing experimental measurements. Measuring the production cross section is a difficult undertaking using bremsstrahlung photons as the probing mechanism, however the simulated bremsstrahlung weighted integral yields can be calculated easily using the equations outlined in section 2.6. The simulated integral yields utilize production cross sections obtained from experimental measurements available in the Experimental Nuclear Reaction Data (EXFOR) library, from evaluated data listed in the Evaluated Nuclear Data File (ENDF) version B-VII.1, and from modeled data obtained from the TALYS-based Evaluated Nuclear Data Library (TENDL) version 2014. Table A.1 lists 30 observed reactions from the 124 potential interference reactions identified in Tables 2.1, 2.2, and 2.3. Of the 30 reactions observed, 14 were measured experimentally and included in EXFOR with 22 of those listed in ENDF. All of the 30 reactions are listed in TENDL. Table 2.4 lists the libraries where the production cross sections can be found with TENDL listed if the cross section is not included in EXFOR or ENDF. The measured results in this section were observed with the HPGe detector.

4.3.1 The ^{18}O(γ,d)^{16}N/^{18}O(γ,np)^{16}N reactions

Figure 4.13 shows the measured integral yields and simulated bremsstrahlung weighted integral yields for the photodisintegration of ^{18}O to ^{16}N in 4.13a. Figure 4.13b shows the production cross sections available from K. G. McNeill et al., ENDF, and TENDL [40, 41, 75, 76, 91]. Oxygen is the third most abundant element in the universe and its abundance in the earth's crust, atmosphere, and bodies of water makes it a large concern for high energy detection applications [115, 116]. The reactions producing ^{16}N from ^{18}O, ^{18}O(γ,d)^{16}N and ^{18}O(γ,np)^{16}N, have thresholds of 19.6 and 21.8 MeV respectively; the thresholds are well below the maximum operating energy utilized [39]. The production cross section measured by K. G. McNeill includes unseparated (γ,pn), (γ,np), and (γ,d) reactions [91]. The measured integral yield

includes all counts observed from the 6128.3 keV (67% branching ratio) γ-ray photopeak and is calculated from the right-hand side of Equation 2.70 [40, 41]. The line on the graph along the bremsstrahlung weighted integral yields are a cubic B-spline interpolation. The measured integral yield increases monotonically with increasing energy from 24 to 45 MeV. A low count rate is responsible for the large error bars present at 24 MeV in the measured integral yield and those in the bremsstrahlung weighted integral yields are a reflection of the uncertainty in the production cross section by K. G. McNeill et al. At 24 MeV, the measured integral yield is statistically equivalent to the simulated integral yields that includes the McNeill production cross section. The measured integral yield is larger than both the TENDL and ENDF utilized bremsstrahlung yields, at 24 MeV, by 1.8 and 2.3 times respectively. At 29 MeV the measured integral yield is statistically equivalent to both the ENDF and McNeill utilized bremsstrahlung weighted integral yields, but is 2.1 times larger than the value calculated using the TENDL production cross section. For the data points beyond 29 MeV both simulated yields utilizing ENDF and McNeill are on average 2.0 and 1.4 times larger respectively than the measured integral yield. The bremsstrahlung weighted integral yields utilizing the TENDL production cross section oscillates in magnitude above and below the measured integral yield with an average difference of 0.9 times calculated from the three largest data points. At 45 MeV the measured integral yield is statistically equivalent to the bremsstrahlung weighted integral yields using the McNeill measured data. The strong agreement of the measured integral yield at 24, 29, and 45 MeV to the K. G. McNeill et al. bremsstrahlung weighted integral yield with only minor increases in the measured data at 34 and 39 MeV suggests inconsistencies in the measured data at those energies. The photon flux of Figure 3.4 shows that the flux monotonically increases from 24 to 30 MeV but drops at 39 MeV and then increases at 45 MeV. It is possible that the decreased rate of increase in the measured integral yield at 39 MeV is due to a drop in the flux. However, the photon flux does not account for the decreased rate of increase in the measured integral yields at 34 MeV. Inconsistencies in the photon flux may be due to beam alignment or gold foil alignment, however, the exact cause of the decreased flux is unknown. It is also possible that the measured data is simply closer in magnitude to the TENDL

bremsstrahlung weighted integral yields at those energies.

Furthermore, the ^{18}O sample has a purity of 99.9% with the remaining amount likely containing a small percentage of ^{17}O. The ^{17}O(γ,p)^{16}N (threshold 13.8 MeV) reaction may add to the integral yields, however, the low isotopic abundance of ^{17}O (0.04%) in conjunction with the small percentage of ^{17}O present in the sample (less than 0.1%) would lead to a minimal contribution [39,109]. This contribution was not considered in the integral yield calculations, however, it should also be noted that the 6128.3 keV photopeak was not observed in the measured data below 19 MeV in the time frame examined of ~30 minutes. Slight variations in the sample position, placed manually, may also account for deviations in the measured integral yield.

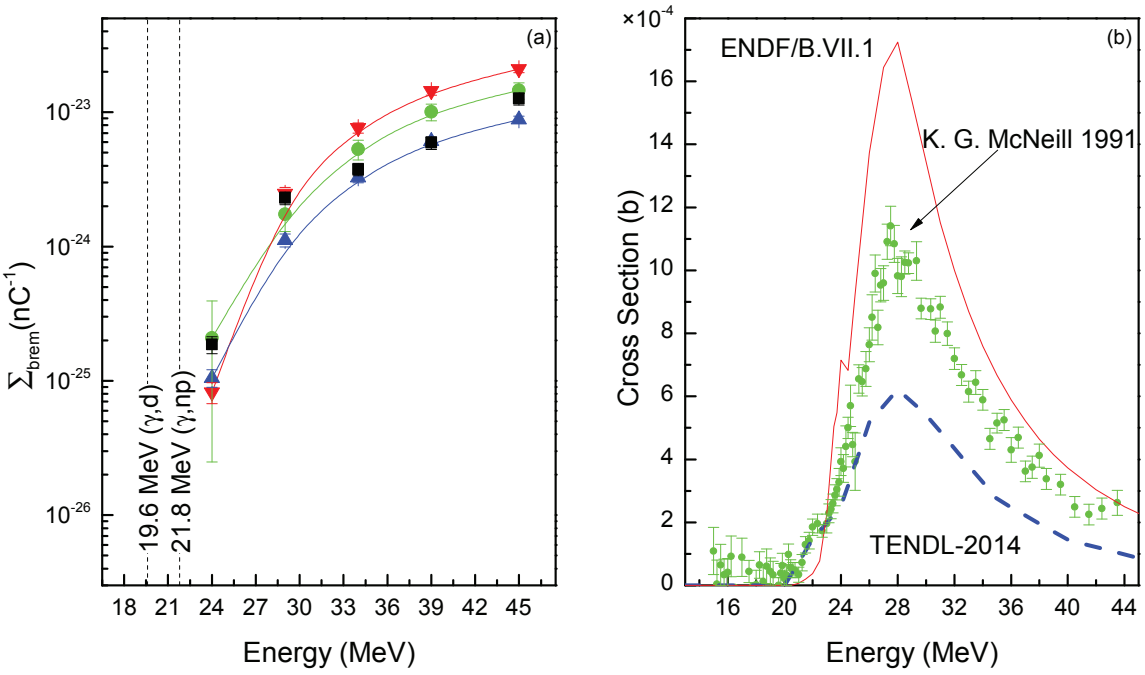

Figure 4.13: Integral yields (a) for the photodisintegration of ^{18}O to ^{16}N measured experimentally (■) and calculated with production cross sections listed in ENDF (▼), measured by K. G. McNeill et al. (●), and modeled in TENDL (▲). The production cross sections (b) from McNeill (●), ENDF (solid), and TENDL (dashed) are also shown. [40, 41, 75, 76, 91]

4.3.2 The $^{18}O(\gamma,p)^{17}N$ reaction

The integral yields for the $^{18}O(\gamma,p)^{17}N$ reaction (threshold 15.94 MeV) are presented in Figure 4.14a with the production cross sections measured by J. G. Woodworth et al. and those listed in ENDF and TENDL shown in 4.14b [40, 41, 51, 75, 76]. The measured integral yield utilizes counts observed from the 870.7 keV (3.3% branching ratio) photopeak [40,41]. At 19 MeV, the neutron yield was slightly elevated above the passive background, however, the 870.7 keV γ-ray peak was not observed. The measured integral yield is in good agreement with the bremsstrahlung weighted integral yield calculated with the ENDF production cross section at all energies analyzed. The measured integral yield is larger by 4.1 times at 24 MeV and increases to 7.4 times at 45 MeV compared with the simulated calculation utilizing the TENDL production cross section. The bremsstrahlung weighted integral yield utilizing the J. G. Woodworth production cross section is 1.8 times larger than the measured integral yield on average over all energies observed. Based on these results, any simulation utilizing the TENDL productions cross section would significantly underestimate the interference strength affecting both the γ-ray and neutron interference signals. The production cross section measured by J. G. Woodworth et al. would overestimate a simulated interference, however, adequate calculations could be provided by ENDF.

4.3.3 The $^{19}F(\gamma,^{3}He)^{16}N/^{19}F(\gamma,dp)^{16}N/^{19}F(\gamma,n2p)^{16}N$ reactions

Currently, the production cross section for the transmutation of ^{19}F to ^{16}N has not been experimentally measured and listed in EXFOR or evaluated in ENDF, however, it is available from TENDL. The $^{19}F(\gamma,^{3}He)$ (threshold of 22.1 MeV), $^{19}F(\gamma,dp)$ (threshold of 27.6 MeV), and $^{19}F(\gamma,n2p)$ (threshold of 29.8 MeV) reactions produce ^{16}N with the measured and bremsstrahlung weighted integral yields illustrated in Figure 4.15a [39]. The TENDL production cross section is displayed in Figure 4.15b [40, 75]. The 6128.3 keV photopeak was used to define the measured integral yield. The measured integral yield increases with increasing energy one order of magnitude from 24 to 45 MeV and is one order of magnitude larger than the bremsstrahlung weighted integral yield at all energies. Simulations utilizing the TENDL

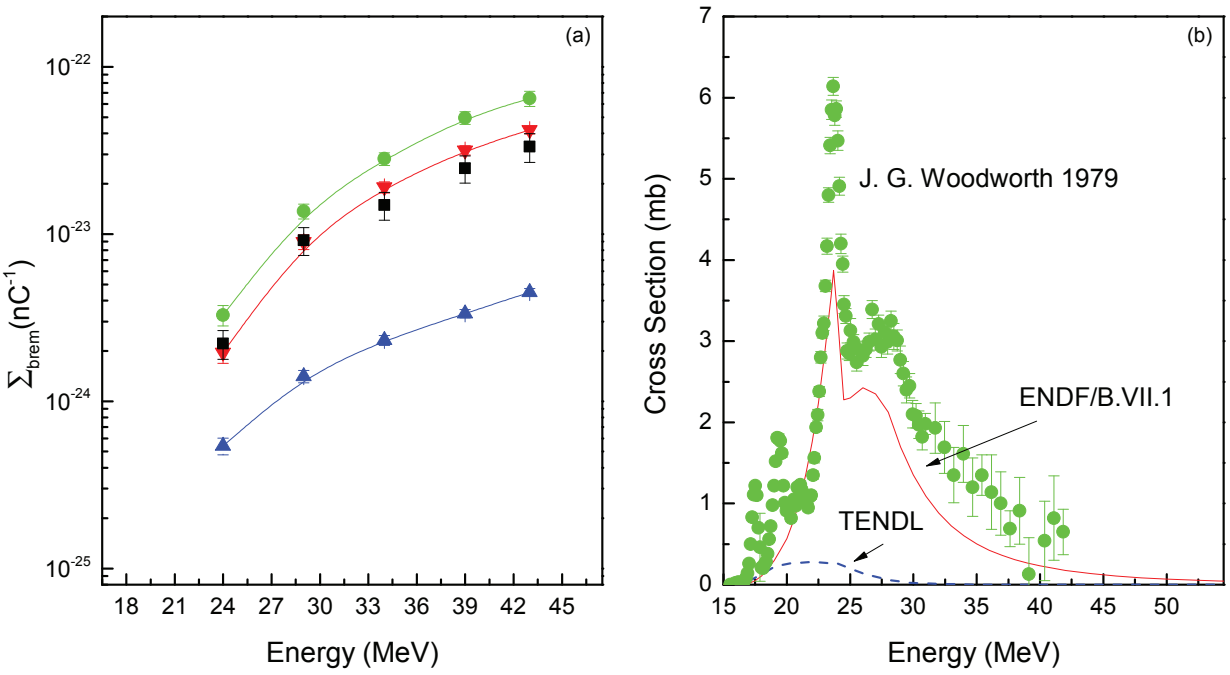

Figure 4.14: Integral yields resulting from the ^{18}O(γ,p)^{17}N reaction (a) measured experimentally (■), calculated with production cross sections listed in ENDF (▼), measured by J. G. Woodworth et al. (●), and obtained from TENDL (▲). The production cross sections (b) measured by J. G. Woodworth et al. (●), listed in ENDF (solid), and TENDL (dashed) are also shown. [40, 41, 51, 75, 76]

production cross section would again underestimate the strength of the interference.

4.3.4 The $^{35/37}$Cl(γ,n/3n)^{34m}Cl reactions

The 3304.0 keV discrete γ-ray from the decay of ^{34m}Cl (32.0 m half-life) directly interferes with the γ-ray signature [40, 41]. The γ-ray is most frequently emitted and has a branching ratio of 12.3% [40, 41]. The ^{34m}Cl isotope is produced by stable ^{35}Cl and ^{37}Cl as a result of ^{35}Cl(γ,n) (12.8 MeV threshold) and ^{37}Cl(γ,3n) (31.7 MeV threshold) reactions induced in the NaCl target. Chlorine is the third most abundant element in the earth's oceans [115]. The reactions are therefore of concern when detection is implemented near seawater. Figure 4.16a shows the measured compared to the bremsstrahlung weighted integral yields using the production cross sections avail-

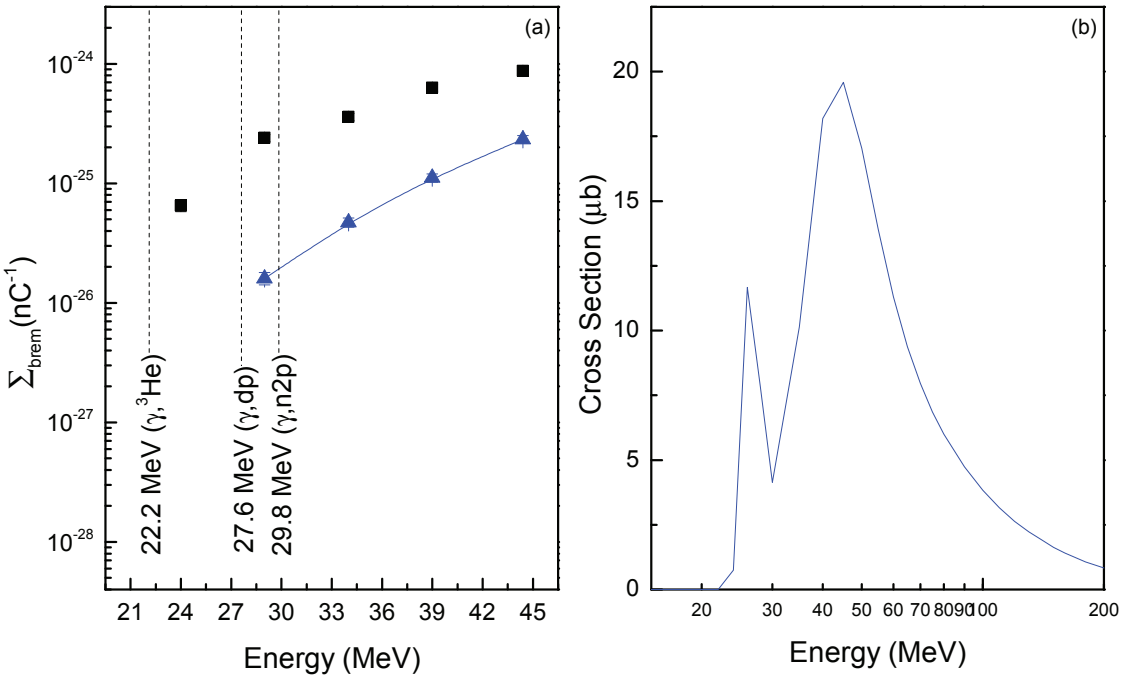

Figure 4.15: Integral yields (a) for the photodisintegration of ^{19}F to ^{16}N measured experimentally (■) and calculated with the production cross section listed in TENDL (▲). The production cross section (b) from TENDL (solid) is also shown. [40, 75]

able from TENDL displayed in 4.16b [40, 75]. The bremsstrahlung weighted integral yield is a sum of the two cross sections using both the ^{35}Cl and ^{37}Cl production cross sections which are weighted to the isotopic abundances as detailed in Equation 2.71. Both integral yields increase monotonically with increasing energy. The measured integral yield is 1.8 times smaller than the bremsstrahlung weighted integral yield averaged over the energies presented from 19 to 45 MeV. The NaCl (iodine free table salt) target contained calcium silicate used as an anticaking agent. A 1% decrease in the number of atoms in the beam was applied to account for the estimated amount of calcium silicate contained in the target. Due to the limited availability of production cross sections, applications that use the ^{35}Cl(γ,n)^{34m}Cl and ^{37}Cl(γ,3n)^{34m}Cl reactions would benefit from additional measurements. However, although the TENDL library was the only library of the three that had the $^{35/37}$Cl(γ,n/3n)^{34m}Cl production cross sections, the production cross sections for the $^{35/37}$Cl(γ,n/3n)^{34}Cl reactions were avail-

able in ENDF. The bremsstrahlung weighted integral yield utilizing ENDF presented in Figure 4.16a is one order of magnitude larger at all energies over the TENDL cross section [40, 41]. The ENDF production cross sections are displayed along with the TENDL cross sections in Figure 4.16b.

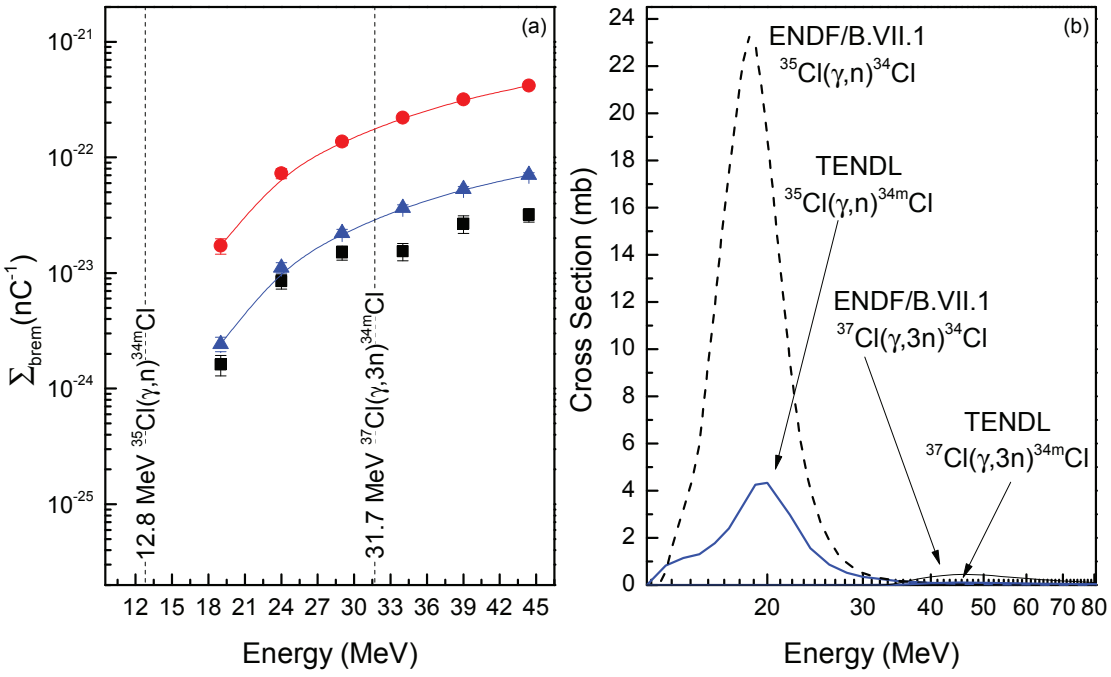

Figure 4.16: Integral yields (a) for the ^{35}Cl(γ,n)^{34m}Cl and ^{37}Cl(γ,3n)^{34m}Cl reactions measured experimentally (■) and calculated with the production cross section listed in TENDL (▲). The bremsstrahlung weighted integral yield (●) using the ENDF production cross sections from the $^{35/37}$Cl(γ,n/3n)^{34}Cl reactions are also displayed. The production cross sections (b) listed in TENDL and ENDF are also shown. [39, 40, 75]

4.3.5 The ^{23}Na(γ,n2p/3n)^{20}F/^{20}Na reactions

The ^{23}Na isotope transmutes to ^{20}F and ^{20}Na upon irradiation exceeding the reaction threshold energy in the NaCl target. Fluorine-20 is produced by three reactions from ^{23}Na: (γ,^{3}He) (24.5 MeV energy threshold), (γ,dp) (30.0 MeV energy threshold), and (γ,n2p) (32.2 MeV energy threshold) [39]. Sodium-20 results from the ^{23}Na(γ,3n)

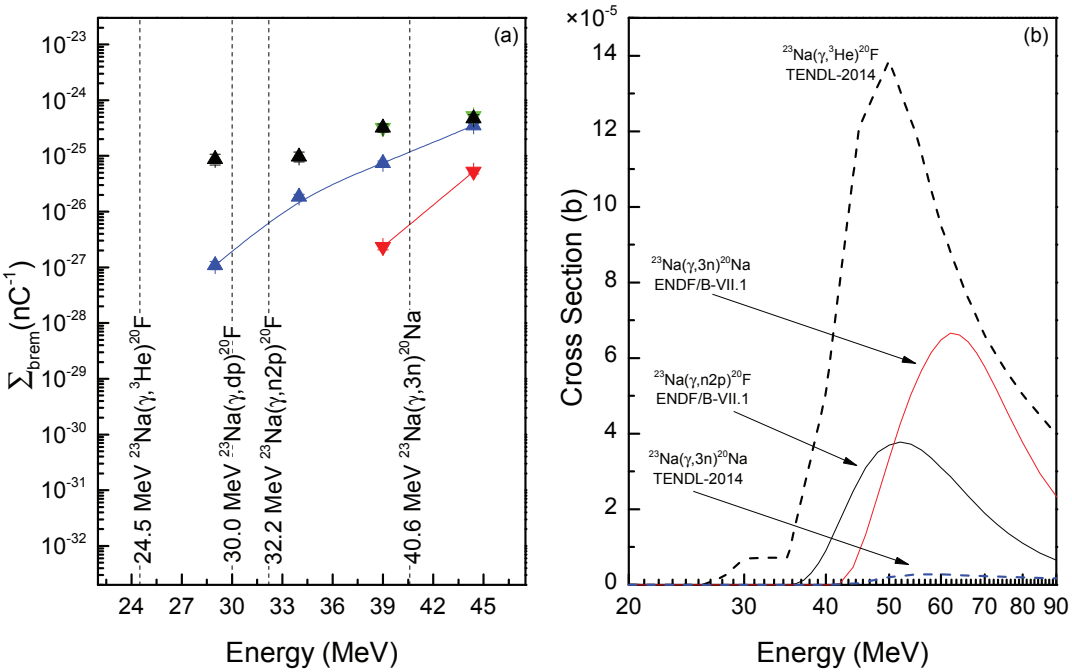

Figure 4.17: Integral yields (a) for the photodisintegration of ^{23}Na to ^{20}F and ^{20}Na measured experimentally with an ENDF (▼) and TENDL weight factor (▲), and calculated using the production cross sections listed in TENDL (▲) and ENDF (▼). The production cross sections (b) for ^{23}Na transmuted to ^{20}F available from TENDL (dashed) and ENDF (solid) and ^{23}Na transmuted to ^{20}Na available from TENDL (dashed) and ENDF (solid) are also displayed. [39–41, 75]

(40.6 MeV energy threshold) reaction [39]. Sodium is the 7th most abundant element in the earth's crust and the 4th most abundant in the earth's oceans which can make the potential for an interfering signal significant [115]. Fluorine-20 β^- decays and emits β-particles in the γ-ray signature region with endpoint energies of 5390.9 keV (branching ratio of 99.9%) and 7024.5 keV (branching ratio of 5×10^{-4}%) [40,41]. Discrete γ-rays with energy in the signature region are also emitted, however, the branching ratio above 3 MeV (8.3×10^{-3}%) is minimal [40, 41]. Several β-particles within the signature region (total branching ratio of 100%) follow the decay of ^{20}Na. The β-particle with the largest endpoint energy (12.3 MeV) also has the largest branching ratio of 79.5% [40, 74]. Several discrete γ-rays are also emitted with a total branching

ratio of 2.7×10^{-1}% above 3 MeV contributing minimal energy to the signature region [74]. The 1633.6 keV (branching ratio of 99.9%) and 1634.0 keV (branching ratio of 79.5%) γ-rays from the decay of ^{20}F and ^{20}Na respectively are most easily observed and provide evidence of reaction occurrence [41, 74]. The energy difference is smaller than the energy resolution of the HPGe detector (FWHM 2.00 keV at 1.33 MeV), therefore the individual peaks can not be resolved. Figure 4.17a shows the measured and bremsstrahlung weighted integral yields using the production cross sections available from ENDF and TENDL shown in 4.17b. Reaction events were not separated in the experimental data, rather, the total counts observed in the ~1634 keV photopeak were used to calculate the measured integral yield. There was no observable peak below 29 MeV. Half-lives and branching ratios for the decay of ^{20}F (11.2 s) and ^{20}Na (4.5×10^{-1} s) were included in the bremsstrahlung weighted integral yields. The figure shows two measured integral yields, one includes a weight factor that utilizes the ENDF production cross sections and the other the TENDL production cross sections. Weight factors are used in accordance with Equation 2.72 to account for integral yields that are produced from the same parent, but result in different daughter isotopes. The starting energy of the measured integral yield utilizing the ENDF weight factor corresponds to the starting energy at which tabulation of the production cross section begins.

The measured integral yield calculated with the TENDL weight factor is one order of magnitude larger than the bremsstrahlung weighted integral yield utilizing the TENDL production cross section at 29 MeV. The difference between the measured and TENDL integral yields at 34 and 39 MeV is ~5 and ~4 times respectively. The values are statistically equivalent at 45 MeV. The measured integral yield using the ENDF weight factor at 39 MeV is two orders of magnitude above the bremsstrahlung weighted integral yield utilizing the ENDF production cross section and one order of magnitude larger at 45 MeV. A simulated signal utilizing the ENDF production cross section would not produce an interference until 36 MeV which is a drastic difference to the experimental results. At 29 MeV the measured integral yield is statistically equivalent to the value at 34 MeV. The pattern of equal values in the measured integral yields at 29 and 34 MeV is identical to the measured curve for the

$^{35/37}$Cl(γ,n/3n)^{34m}Cl reaction using the same NaCl target shown in Figure 4.16. This indicates that the statistical equivalence at 29 and 34 MeV does not occur from the reaction, but rather results from the experiment. At increasing bremsstrahlung beam energies, the expected output would result in a monotonic increase with increasing energy. Possible outcomes that may lead to unexpected fluctuations in the yield are target misalignment, accelerator energies that do not match the energy expected, and photon flux variations throughout the range of energies. Figure 3.6 shows that the calculated photon flux through the NaCl target follows a similar trend to the measured integral yields with values at 29 and 34 MeV being statistically equivalent. The direct cause of inconsistencies in the photon flux is unknown, however, placement of the gold foil on the target or in the detector arrangement would lead to data fluctuations. Discrepancies in the integral yields highlight the challenges associated with simulating interferences.

4.3.6 The $^{40/42}$Ca(γ,np/p3n)^{38}K reactions

Calcium is the fifth most abundant element in the earth's crust and its ubiquity in many commercial products makes its occurrence likely in detection environments. Potassium-38 is produced through reactions that are probable under the maximum energy studied (45 MeV) by two stable isotopes of calcium, ^{40}Ca and ^{42}Ca. The ^{40}Ca(γ,d) and ^{40}Ca(γ,np) reactions are possible at lower threshold energies of 19.2 and 21.4 MeV respectively, while the ^{42}Ca(γ,d2n) and ^{42}Ca(γ,p3n) reactions have larger energy thresholds of 39.0 and 41.3 MeV respectively [39]. Potassium-38 decays with a 3935.6 keV (0.14% branching ratio) γ-ray and β^+ particles with endpoint energies of 3746.4 keV (99.9% branching ratio) and 5913.9 keV (0.05% branching ratio) within the signature region [40, 41]. It should be noted that these reactions can also produce the metastable state of ^{38}K and while ^{38m}K does decay with β-particles within the signature region, discrete γ-rays are not produced which restricts the integral yield measurements developed herein to ^{38}K. Figure 4.18a displays the measured integral yield and bremsstrahlung weighted integral yields utilizing the production cross sections measured by A. Veyssière et al., evaluated in ENDF, and modeled in

TENDL. The production cross sections are displayed in Figure 4.18b [40, 41, 75, 117]. The ENDF and TENDL production cross sections include data starting at an energy of 19.5 and 20.0 MeV respectively suggesting production cross section calculations for the ^{40}Ca(γ,d)^{38}K reaction, however, the literature does not mention which reactions were included in the measurement. The ENDF and TENDL production cross sections for the ^{42}Ca isotope start at 34 and 35 MeV respectively indicating energetics via the (γ,d2n)^{38}K reaction, however, it is unclear if events from the ^{42}Ca(γ,p3n)^{38}K reaction were also included in the data. The measured integral yield does not distinguish events into separate reactions, but utilizes all counts from the 2167.5 keV photopeak that has a 99.86% branching ratio [40, 41]. The 2167.5 keV photopeak was not observed in the experimental data below 24 MeV. Isotopic abundances were included in the bremsstrahlung weighted integral yields that were constructed using Equation 2.71. All integral yields increase monotonically from 24 to 45 MeV. The bremsstrahlung weighted integral yield utilizing A. Veyssière et al. is larger than the measured integral yield by three orders of magnitude decreasing to two orders at the higher energies presented. This large difference results from the inclusion of ^{40}Ca(γ,n)^{39}Ca events in the A. Veyssière et al. production cross section which has a threshold energy of 15.6 MeV [39–41]. The production cross section was listed as the ^{40}Ca(γ,np)^{38}K reaction, however, events from the individual reactions were not separated. The magnitude of the measured integral yield is on average smaller by a factor of 4.6 and 14.4 from the calculations using the TENDL and ENDF production cross sections respectively. The slight decrease in the rate of increase in the measured integral yield from 34 to 39 MeV can be attributed to a similar change in the photon flux at those energies displayed in Figure 3.7. The reported purity of the calcium sample (99.5% metals basis) has been accounted for, however, the true concentration may include non-metal impurities and is therefore unknown. Any unaccounted for non-metal impurities would increase the measured integral yield by reducing the number of atoms in the beam, however, the percentage would likely be minimal. Discrepancies in the production cross sections make modeling challenging with all bremsstrahlung weighted integral yields overestimating the interference strength in a simulated signal.

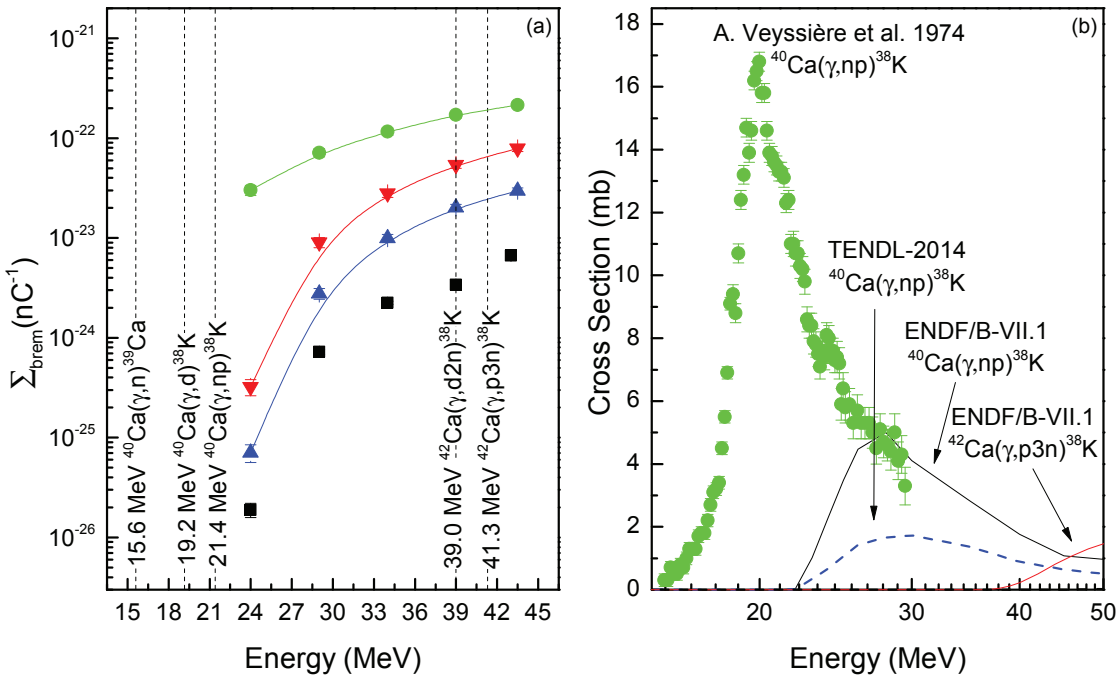

Figure 4.18: Integral yields for the photodisintegration of ^{40}Ca and ^{42}Ca to ^{38}K (a) measured experimentally (■), and calculated with the available production cross sections measured by A. Veyssière et al. (●), listed in ENDF (▼), and TENDL (▲). The ^{40}Ca(γ,np)^{38}K production cross sections listed in EXFOR (●), ENDF (solid), and TENDL (dashed) and for the ^{42}Ca(γ,p3n)^{38}K reaction from ENDF (solid) are displayed in (b). [40, 41, 75, 117]

4.3.7 The $^{39/40/41}$K(γ,n/2n/3n)^{38}K reactions

The integral yields shown in Figure 4.19 display the 2167.5 keV (99.9% branching ratio) peak resulting from the β^+ decay of ^{38}K (7.6 minute half-life) produced from the $^{39/40/41}$K(γ,n/2n/3n) reactions [40, 41, 75]. Potassium-38 decays with one discrete γ-ray within the signature region containing energy of 3935.6 keV emitted with a 1.4×10^{-1}% branching ratio. The larger concern comes from β-particles within the signature region with branching ratios of 99.9% and 5×10^{-2}% and endpoint energies of 3746.4 and 5913.9 MeV respectively [40, 41]. Potassium is quite common being the 8th and 7th most abundant element in the earth's crust and oceans respectively [115]. Applying Equation 2.71, the measured integral yield shown in Figure 4.19a includes

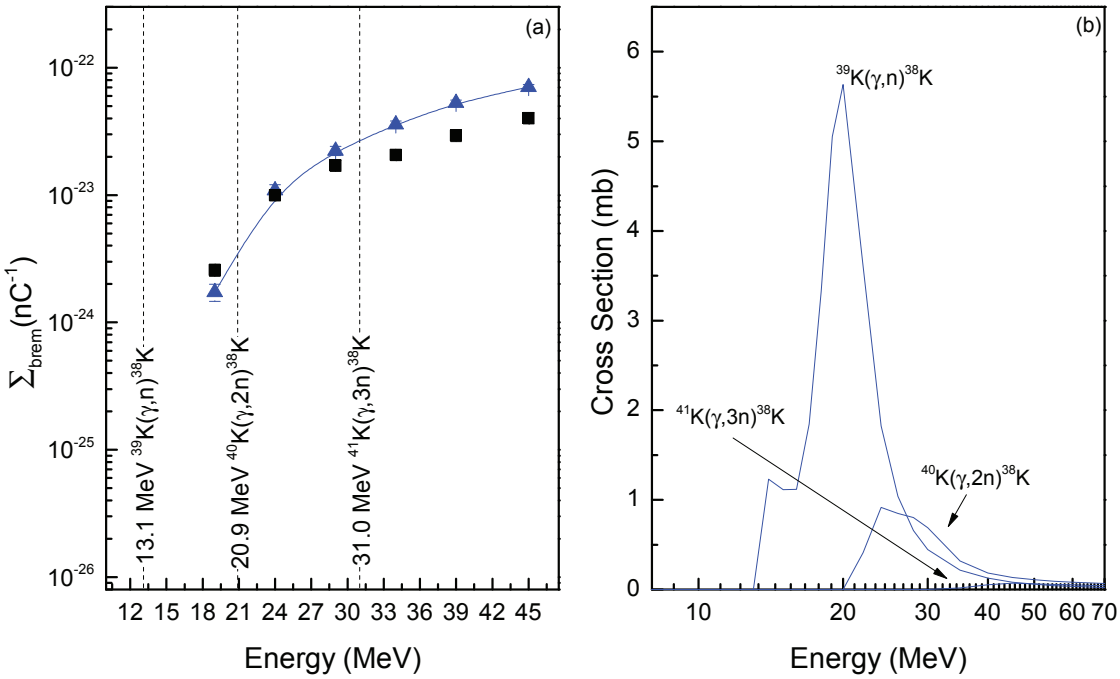

Figure 4.19: Measured (■) and bremsstrahlung weighted (▲) integral yields (a) for the $^{39/40/41}$K(γ,n/2n/3n)^{38}K reactions. The bremsstrahlung weighted integral yield, computed using the sum of the three production cross sections listed in TENDL (b), is adjusted to account for the isotopic abundance of each parent isotope. The accelerator operating energy increases from 19 to 45 MeV in 5 MeV increments. [40, 41, 75]

the total events observed in the 2167.5 keV peak while the bremsstrahlung weighted integral yield in Figure 4.19b sums the integral yields for the three reactions weighted by the individual isotopic abundances of ^{39}K, ^{40}K, and ^{41}K. The bremsstrahlung weighted integral yields account for the energy thresholds of 13.1, 20.9, and 31.0 MeV for the ^{39}K(γ,n), ^{40}K(γ,2n), and ^{41}K(γ,3n) reactions respectively. The measured integral yield is larger at 19 MeV and statistically equivalent at 24 MeV to the bremsstrahlung weighted integral yield that uses the TENDL production cross section. At 29 MeV the magnitudes flip with the bremsstrahlung weighted integral yield being larger than the measured integral yield. This difference continues for the remaining energies presented. The difference in magnitude between the measured integral yield and the bremsstrahlung weighted integral yield is 1.5 times over all energies

presented. The same statistical values were observed at 29 and 34 MeV for the measured integral yield. When examining the photon flux for KBr, displayed in Figure 3.8, statistically similar values were calculated for the 24 and 29 MeV data, however, the 34 MeV data is larger than those values, as expected. As a result it is unlikely that the similar values in the measured integral yield are a result of the photon flux as calculated. However, target misalignment may contribute to the decreased yield at 34 MeV. Furthermore, production cross sections were not measured experimentally or listed in ENDF. Although the ^{39}K(γ,n) reaction has an energy threshold of 13.1 MeV, the ^{38}K 2167.5 keV peak was not observed in the experimental data below 19 MeV. The measured integral yield does account for the potassium concentration using a 99.9% purity (metal basis).

Chapter 5

Conclusions

5.1 Reliability of fission signals at high bremsstrahlung endpoint energies

5.1.1 Signature Definitions

This experiment investigated the impact of interferences on fission signatures in active inspection environments utilizing bremsstrahlung beams with endpoint energies ranging from 15 to 45 MeV. Increasing the beam energy provided insight into the feasibility of stand-off fission detection. Forty-four targets were irradiated: 28 non-fissionable materials and five commercial products free of fissioning isotopes. The signature definitions were developed in prior experiments where a small number of targets were irradiated at bremsstrahlung beam energies up to 22 MeV. Using the method to construct signatures developed in prior experiments, signatures in the experiments presented here were composed of neutrons and γ-rays emitted 19 and 29 ms respectively following each beam pulse and to the next pulse. The time cut eliminated neutrons and γ-rays that resulted from (γ,n) and (n,γ) reactions. The γ-ray signatures included γ-rays restricted to energies from 3 MeV to 7.2 MeV. The energy limit decreased the likelihood of detecting γ-rays emitted from naturally occurring and commercially available radioisotopes. By using the time and energy cuts, the fission signatures were composed of delayed neutrons and delayed γ-rays emitted as

a result of β-decay processes following fission events.

5.1.2 Signal Interferences

Fission signals were examined in the dual phase space consisting of delayed neutrons and delayed γ-rays with targets irradiated with a bremsstrahlung beam at endpoint energies of 15, 22.5, 30, and 37.5 MeV. For all endpoint energies the beam was pulsed at a 15 Hz repetition rate with targets irradiated for a duration of ~10 minutes. The duration was chosen to match real-world detection times as closely as could be achieved while obtaining adequate statistics with errors totaling ~10% or less. Detectable fission signals were greater than the critical decision level (L_c); defined as the yield required to overcome the background and produce a detectable signal.

At the 15 MeV bremsstrahlung endpoint energy, the non-fissionable and no-target signals were statistically equivalent to the natural passive background. Therefore, the background signal included all non-fissionable and no-target inspections. A 1% false positive boundary was implemented and identical at all energies investigated. The magnitude of all non-fissionable signals fell below L_c. The fission signals, excluding the lowest mass target (0.7 g in-beam mass), were significantly above background and, therefore discernable from all non-fission samples. The detection limit, L_d, defined the magnitude of the yield required for a fissionable material to be detected in a detection system with planned inspection parameters and included a 1% false negative probability. The 1% probability was implemented at all energies examined. The planned inspection system included irradiation for 9000 pulses, an average charge per pulse of 150 nC, and a solid angle that matched the detectors of the existing system (0.012 sr for γ-rays and 0.159 sr for neutrons). Utilizing L_d, the minimal detectable mass was $3.14 \pm 1.31 \times 10^{-2}$ g following the "Or" two-dimensional detection algorithm. This increased the sensitivity over a one-dimensional γ-ray detection system by 1.6% and by 68% over a neutron only construction.

Targets were then examined at a bremsstrahlung endpoint energy of 22.5 MeV. Clear interferences were observed, however, due to the irradiation energy gap from 15 to 22.5 MeV, the exact energy of their emergence is unknown. Interferences were

defined by signal magnitudes greater than L_c. Eleven non-fissionable targets exceeded the "Or" L_c and 7 the "And" L_c. Neutron activity in the no-target samples necessitated the addition of an active component into the neutron L_c calculations, while the γ-ray targets were equivalent to the passive background. Five of the 7 interfering signals in the "And" detection region were from targets containing oxygen. The largest yield was observed from the 41 g (mass in-beam) ^{18}O sample. All oxygen containing samples had increased γ-ray yields due to the ^{18}O(γ,np)^{16}N and ^{18}O(γ,d)^{16}N reactions. Nitrogen-16 decays via the β^- process emitting 6128.6 keV and 7115.2 keV γ-rays as well as β-particles with a maximum endpoint energy of 10.4 MeV increasing the γ-ray yield [40, 41]. The neutron signals increased as a result of the ^{18}O(γ,p)^{17}N reaction. Nitrogen-17 emits a neutron upon its decay via the β^- process increasing the neutron yield. The γ-ray yield also increased as a result of β-particles emitted by ^{17}N with a maximum endpoint energy of 8.7 MeV [40, 41]. The ^{9}Be and Pb targets both had increased yields. The ^{9}Be γ-ray yield increased as a result of the ^{9}Be(γ,p)^{8}Li reaction that produced a β-particle with a maximum endpoint energy of 13.0 MeV upon the decay of ^{8}Li [40, 41]. The neutron yield was elevated by the ^{9}Be(γ,n)^{8}Be reaction that has a 1.7 MeV energy threshold [39]. The direct cause of the increased Pb γ-ray and neutron signals is unknown. All fission targets were above the "And" and "Or" L_c algorithms and in the detectable region. While the M_{min} is undeterminable in environments with interferences, the known interferences were removed from the calculations to illustrate the lowest mass that would be detectable at 22.5 MeV. Utilizing the "And" algorithm, the M_{min} was $2.2\times10^{-1}\pm2.3\times10^{-4}$ g. The two-dimensional "And" L_d came with a 45% loss in sensitivity from the one-dimensional γ-ray L_d and a gain of 40% was achieved over the neutron L_d. The loss in sensitivity from neutrons and gain from γ-rays corresponds with the larger number of delayed γ-rays emitted per fission event over delayed neutrons. This can be adjusted by increasing the size and/or number of neutron detectors in relation to γ-ray detectors.

Analysis continued with targets irradiated at a bremsstrahlung endpoint energy of 30 MeV. One hundred percent of the non-fissionable targets exceeded the "Or" L_c and 50% the "And" L_c leaving no apparent strategy to mitigate interferences. Due to elemental and isotopic abundances and in addition to the signals mentioned

in the 22.5 MeV data, the most concerning interferences were from NaCl, LiF, and Ca. The $^{35/37}$Cl(γ,n/3n)^{34m}Cl reactions directly increased the γ-ray yield from the 3304.0 keV γ-ray emitted as a result of the β^+ decay of ^{34m}Cl. The emission of a β-particle with maximum endpoint energy of 3150.1 keV is also probable (28.5% branching ratio) from the decay of ^{34m}Cl [40,41]. The NaCl sample also produces the ^{26}Na(γ,^{3}He/3n)^{20}F/^{20}Na reactions. Fluorine-20 β^- decays (11.2 s half-life) adding energy to the signature region from 3332.5 keV and 4965.9 keV discrete γ-rays and bremsstrahlung photons created from β-particles with 5390.9 keV and 7024.3 keV maximum endpoint energies [40, 41]. The ^{26}Na(γ,^{3}He)^{20}F has a reaction threshold of 24.5 MeV [39]. As the energy increases beyond ~40 MeV the ^{23}Na(γ,3n)^{20}Na reaction is probable and adds energy to the γ-ray signature largely from interactions with β-particles [39]. The branching ratio above 3 MeV is 100% and 0.3% for β-particles and discrete γ-rays respectively [74]. The LiF γ-ray and neutron signals increase from the decay of ^{16}N and ^{17}N following the ^{19}F(γ,^{3}He) (22.1 MeV threshold) and ^{19}F(γ,2p) (24.0 MeV threshold) reactions respectively [39]. Note that the ^{19}F(γ,dp)^{16}N (27.6 MeV threshold) and ^{19}F(γ,n2p)^{16}N (29.8 MeV threshold) reactions also contribute. Energy contributions to the γ-ray and neutron signals from ^{16}N and ^{17}N are discussed in the ^{18}O reactions. Several reactions contribute energy to the signals in targets containing calcium. The ^{40}Ca(γ,np)$^{38/38m}$K (~21.4 MeV threshold), ^{40}Ca(γ,n)^{39}Ca (15.6 MeV threshold), and ^{40}Ca(γ,2n)^{38}Ca (28.9 MeV threshold) reactions all contribute energy from β-particle interactions [39–41]. The large number of interferences make the M_{min} incalculable.

In the highest energy dual phase space, 37.5 MeV, all of the non-fissionable samples exceeded the "Or" L_c and 70% the "And" L_c. Without a clear approach to mitigate bremsstrahlung activity produced by β-particles or the neutrons resulting from (γ,n) reactions, the signals in the detectable region could not be unequivocally identified as fissionable.

The experiment indicates that irradiating targets with bremsstrahlung endpoint energies lower than ~22 MeV would lead to fission signals that are reliable. At higher energies, the observance of interferences would lead to false positives and eventually gross unreliability of the fission signals at the highest energies examined.

5.1.3 Integral Yields

Of the 30 observed interfering reactions listed in Table A.1, 22 were available in ENDF/B-VII.1 and only 14 were measured experimentally and found in EXFOR [40, 41, 76]. The limited availability of production cross sections led to an examination of bremsstrahlung weighted integral yields for 7 of the interfering reactions. Comparisons of measured integral yields with bremsstrahlung weighted integral yields would give some insight into the accuracy of simulated interferences.

The ^{18}O(γ,p)^{17}N and ^{18}O(γ,np)^{16}N reactions were initially examined because the production cross sections were available from EXFOR, ENDF, and TENDL making comparisons to the measured integral yield accessible with all 3 libraries. The measured integral yield for the ^{18}O(γ,np)^{16}N reaction using the 6128.3 keV discrete γ-ray was in good agreement with the bremsstrahlung weighted integral yield utilizing the production cross section measured by K. G. McNeill et al. at 24, 29, and 45 MeV, but dipped below the simulated yield at 34 and 39 MeV by 1.6 times averaged over both energies. At 34 and 39 MeV the measured integral yield was in good agreement with the bremsstrahlung weighted integral yield utilizing the TENDL production cross section. Inconsistencies in the photon flux are a probable cause for the fluctuation in the measured integral yield. The inconsistencies may have led to the decrease below the McNeill bremsstrahlung weighted integral yield at 34 and 39 MeV. Nonetheless, discrepancies in the production cross sections would make simulating a signal difficult.

The measured yield for the ^{18}O(γ,p)^{17}N reaction utilizing the 870.7 keV γ-ray was in good agreement with the bremsstrahlung weighted integral yield constructed from the ENDF production cross section for all energies examined. However, large discrepancies in the production cross sections would make simulating a signal difficult without the prior knowledge that the measured integral yield was in statistical agreement with the ENDF bremsstrahlung weighted integral yield.

The production cross section for the ^{19}F(γ,^{3}He)^{16}N reaction was only available in TENDL for comparison to the measured integral yield using the 6128.3 keV γ-ray. The measured yield was one order of magnitude larger than the bremsstrahlung weighted integral yield at all energies examined. A simulated signal using the TENDL produc-

tion cross section would grossly underestimated the magnitude of the interference.

The measured integral yield for the $^{35/37}$Cl(γ,n/3n)^{34m}Cl reactions was compared to the bremsstrahlung weighted integral yield using the TENDL production cross section. The 3304.0 keV γ-ray was utilized for its construction. Production cross sections for the reaction were not available in ENDF or EXFOR. The integral yields were in good agreement at 19, 24, and 29 MeV. At 34, 39, and 45 MeV the measured integral yield was 2.2 times lower on average than the bremsstrahlung weighted integral yield. Slight inconsistencies in the magnitude of the measured integral yield were attributed to the photon flux. Additional experimental measurements of the $^{35/37}$Cl(γ,n/3n)^{34m}Cl production cross sections would be useful.

The measured integral yield for the ^{23}Na(γ,^{3}He)^{20}F and ^{23}Na(γ,3n)^{20}Na reactions were also calculated from observations of the NaCl target. Production cross sections from TENDL and ENDF were available. The ~1634 keV photopeak was utilized for the measured integral yield and accounts for the 1633.6 keV γ-ray from the decay of ^{20}F and the 1634.0 keV γ-ray from the decay of ^{20}Na which could not be resolved by the detector [40, 41, 74]. The measured integral yield using the TENDL weight factor was two orders of magnitude larger than the bremsstrahlung weighted integral yield using the TENDL production cross section at 29 MeV. At 34 and 39 MeV the measured yield was one order of magnitude larger and was statistically equivalent to the bremsstrahlung weighted integral yield at 45 MeV. The measured integral yield using the ENDF weight factor was two orders of magnitude larger at 39 MeV and one order of magnitude larger at 45 MeV than the bremsstrahlung weighted integral yield utilizing the ENDF production cross section. In both cases, a simulated signal would underestimate the interference magnitude at energies lower than 45 MeV.

The 2167.5 keV γ-ray was utilized for calculation of the measured integral yield that included the ^{40}Ca(γ,np)^{38}K and ^{42}Ca(γ,p3n)^{38}K reactions. Production cross sections were available from EXFOR, ENDF, and TENDL, however, the data measured by A. Veyssière et al. included events from the decay of ^{39}Ca following the ^{40}Ca(γ,n) reaction. The inclusion of the ^{40}Ca(γ,n)^{39}Ca reaction led to differences between the measured and the bremsstrahlung weighted integral yield of three orders of magnitude at 24 MeV and two orders for the remaining energies examined. The measured

integral yield was in closest agreement to the bremsstrahlung weighted integral yield using the TENDL production cross section with a difference of 4.6 averaged over all energies examined. In this case, simulated signals would overestimate the interference magnitude.

Discrepancies in available production cross sections make simulating interfering signals challenging. The question becomes, which production cross section would provide data that would most closely match a true signal. Furthermore, in cases where a production cross section was available from only one library, the experiment generally found that a simulated signal would be either over or under estimated. These results indicate that the magnitude of a simulated signal would be unreliable and that the scientific community would benefit from additional measurements of production cross sections.

Bibliography

[1] J. L. Jones, W. Y. Yoon, Y. D. Harker, J. M. Hoggan, K. J. Haskell, and L. A. VanAusdeln. Proof-of-concept assessment of a photofission-based interrogation system for the detection of shielded nuclear material. Technical Report INEEL/EXT-2000-01523, Idaho National Engineering and Environmental Laboratory, Idaho Falls, ID 83415, 2000.

[2] J. L. Jones, W. Y. Yoon, K. J. Haskell, D. R. Norman, and J. M. Hoggan. Photofission-based, nuclear material detection: Technology demonstration. Technical Report INEEL/EXT-02-01406, Idaho National Engineering and Environmental Laboratory, Idaho Falls, ID 83415, 2002.

[3] D. Slaughter, M. Accatino, A. Bernstein, J. Candy, A. Dougan, J. Hall, A. Loshak, D. Manatt, A. Meyer, B. Pohl, S. Prussin, R. Walling, and S. Weirup. Detection of special nuclear material in cargo containers using neutron interrogation. Technical Report UCRL-ID-155315, Lawrence Livermore National Laboratory, 2003.

[4] E. B. Norman, S. G. Prussion, R. Larimer, H. Shugart, E. Browne, A. R. Smith, R. J. McDonald, H. Nitsche, P. Gupta, M. I. Frank, and T. B. Gosnell. Signatures of fissile materials: high-energy γ rays following fission. *Nuclear Instruments and Methods in Physics Research A*, 521:608, 2004.

[5] D. R. Slaughter, M. R. Accatino, A. Bernstein, J. A. Church, M. A. Descalle, T. B. Gosnell, J. M. Hall, A. Loshak, D. R. Manatt, G. J. Mauger, T. L. Moore, E. B. Norman, B. A. Pohl, J. A. Pruet, D. C. Petersen, R. S. Walling, D. L.

Weirup, S. G. Prussin, and M. McDowell. Preliminary results utilizing high-energy fission product γ-rays to detect fissionable material in cargo. *Nuclear Instruments and Methods in Physics Research B*, 241:777, 2005.

[6] M. Gmar, E. Berthoumieux, S. Boyer, F. Carrel, D. Doré, M. L. Giacri, F. Lainé, B. Poumarède, D. Ridikas, and A. V. Lauwe. Detection of nuclear material by photon activation inside cargo containers. In *Non-Intrusive Inspection Technologies*, page 62130F. SPIE-The International Society of Optical Engineering, May 30 2006.

[7] D. K. Wehe, H. Yang, and M. H. Jones. Observation of ^{238}U photofission products. *IEEE Transactions on Nuclear Science*, 53(3), June 2006.

[8] B. W. Blackburn, J. L. Jones, C. E. Moss, J. T. Mihalczo, A. W. Hunt, F. Harmon, S. M. Watson, and J. T. Johnson. Utilization of actively-induced, prompt radiation emission for nonproliferation applications. *Nuclear Instruments and Methods in Physics Research B*, 261:341, 2007.

[9] J. M. Hall, S. Asztalos, P. Biltoft, J. Church, M. A. Descalle, T. Luu, D. Manatt, G. Mauger, E. Norman, D. Petersen, J. Pruet, S. Prussin, and D. Slaughter. The nuclear car wash: Neutron interrogation of cargo containers to detect hidden SNM. *Nuclear Instruments and Methods in Physics Research B*, 261:337, 2007.

[10] T. Gozani. Fission signatures for nuclear material detection. In *IEEE Transactions on Nuclear Science*, volume 56, page 736. IEEE, 2009.

[11] D. D. Hinshelwood, R. J. Allen, J. P. Apruzese, R. J Commisso, G. Cooperstein, S. L Jackson, D. Mosher, D. P. Murphy, P. F. Ottinger, J. W. Schumer, S. B. Swanekampo, B. V. Weber, F. C. Young, J. C. Zier, A. W Hunt, Z. M. Larsen, E. S. Cárdneas, and A. N. Caruso. High-power, pulsed bremsstrahlung source for inducing photofission. In *Pulsed Power Conference (PPC), 2011 IEEE*, page 1428. IEEE, 2011.

[12] R. C. Runkle, D. L. Chichester, and S. J. Thompson. Rattling nucleons: New

developments in active interrogation of special nuclear material. *Nuclear Instruments and Methods in Physics Research A*, 663:75, 2012.

[13] A. Sari, F. Carrel, F. Lainé, and A. Lyoussi. Neutron interrogation of actinides with a 17 MeV electron accelerator and first results from photon and neutron interrogation non-simultaneous measurements combination. *Nuclear Instruments and Methods in Physics Research B*, 312:30, 2013.

[14] M. T. Andrews, E. C. Corcoran, J. T. Goorley, and D. G. Kelly. A system for the measurement of delayed neutrons and gammas from special nuclear materials. *Journal of Radioanalytical and Nuclear Chemistry*, 303:2431, 2015.

[15] E. T. E. Reedy, S. J. Thompson, and A. W. Hunt. The detection of delayed gamma-rays between intense bremsstrahlung pulses for discriminating fissionable from non-fissionable materials. *Nuclear Instruments and Methods in Physics Research A*, 606:811, 2009.

[16] M. T. Kinlaw and A. W. Hunt. Time dependence of delayed neutron emission for fissionable isotope identification. *Applied Physics Letters*, 86:254104, 2005.

[17] E. S. Cárdenas. Detection of delayed gamma rays using $Bi_4Ge_3O_{12}$ and NaI(Tl) detectors for the identification of fissionable materials. Master's thesis, Idaho State University, 2009.

[18] E. S. Cárdenas, E. T. E Reedy, H. A. Seipel, B. H. Failor, and A. W. Hunt. Comparison of fission signatures from β^- delayed γ-ray and neutron emissions. *Nuclear Instruments and Methods in Physics Research Section A*, 792:67, 2015.

[19] T. Gozani. Active nondestructive assay of nuclear materials principles and applications. Technical report, United Sates Nuclear Regulatory Commission, NUREG/CR-0602, 1981.

[20] J. A. Mullens, J. S. Neal, P. A. Hausladen, S. A. Pozzi, and J. T. Mihalczo. Fast coincidence counting with active inspection systems. *Nuclear Instruments and Methods in Physics Research B*, 241:804, 2005.

[21] J. Stevenson, T. Gozani, M. Elsalim, C. Condron, and C. Brown. Linac based photofission inspection system employing novel detection concepts. *Nuclear Instruments and Methods in Physics Research A*, 652:124, 2011.

[22] C. E. Moss, C. A. Goulding, C. L. Hollas, and W. L. Myers. Neutron detectors for active interrogation of highly enriched uranium. *IEEE Transactions on Nuclear Science*, 51(4):1677, 2004.

[23] E. T. E. Reedy. *Isotopic Analysis of Fissile Materials Using Delayed γ-rays from Neutron Induced Fission.* PhD thesis, Idaho State University, 2015.

[24] M. T. Kinlaw. *Delayed Neutron Group Parameters from Photofission.* PhD thesis, Idaho State University, 2007.

[25] B. N. Satterwhite. Optimal shielding for NaI γ-ray detectors in standoff applications. Master's thesis, Idaho State University, 2013.

[26] D. Dietrich, C. Hagmann, P. Kerr, L. Nakae, et al. A kinematically beamed, low energy pulsed neutron source for active interrogation. *Nuclear Instruments and Methods in Physics Research B*, 241:826, 2005.

[27] D. L. Chichester, J. D. Simpson, and M. Lemchak. Advanced compact accelerator neutron generator technology for active neutron interrogation field work. *Journal of Radioanalytical and Nuclear Chemistry*, 271:629, 2007.

[28] D. Cester, G. Nebbia, L. Stevanato, et al. Special nuclear material detection with a mobile multi-detector system. *Nuclear Instruments and Methods in Physics Research A*, 663:55, 2012.

[29] J. F. Harmon, D. P. Wells, and A. W. Hunt. Neutrons and photons in nondestructive detection. *Reviews of Accelerator Science and Technology*, 4:83, 2011.

[30] R. C. Lanza and T. Antaya. High energy protons for remote standoff detection of special nuclear materials. In *Applications of Nuclear Techniques, AIP Conf. Proc. 1412*, page 153. American Institute of Physics, June 12-18 2011.

[31] J. O'Malley, A. Jones, J. Threadgold, K. Omar, P. Adsley, S. Quillin, S. Robertson, et al. Advanced active interrogation sources for remote detection of special nuclear material. In *IEEE Conference on Technologies for Homeland Security, 2009. HST '09.*, page 278. IEEE, May 11-12 2009.

[32] C. Hill, J. O'Malley, P. Martin, K. Marshall, R. Maddock, J. Threadgold, R. Commisso, S. L. Jackson, J. Schumer, B. Phlips, P. Ottinger, et al. Active detection of special nuclear material - recommendations for interrogation source approach for UK prototype active detection system. In *Nuclear Science Symposium and Medical Imaging Conference (NSS/MIC), 2012 IEEE*, page 732. IEEE, October 27 2012.

[33] M. Gmar and J. M. Capdevila. Use of delayed gamma spectra for detection of actinides (U,Pu) by photofission. *Nuclear Instruments and Methods in Physics Research A*, 422:841, 1999.

[34] X. Wen, J. G. Kavouras, D. R. Nakazawa, and H. Yang. Simulation and measurement of delayed γ-rays after photon-induced fission. *Nuclear Instruments and Methods in Physics Research A*, 729:781, 2013.

[35] A. Lyoussi, J. Romeyer-Dherbey, F. Jallu, et al. Transuranic waste detection by photon interrogation and on-line delayed neutron counting. *Nuclear Instruments and Methods in Physics Research B*, 160:280, 2000.

[36] J. L. Jones, B. W. Blackburn, D. R. Norman, S. M. Watson, K. J. Haskell, J. T. Johnson, A. W. Hunt, F. Harmon, and C. Moss. Status of the prototype pulsed photonuclear assessment (ppa) inspection system. *Nuclear Instruments and Methods in Physics Research*, A 579:353, 2007.

[37] M. Ankrah. *Sensitivity Measurements for Cargo Scanning Applications Using Photon Interrogation and Neutron Signature Counting Techniques*. PhD thesis, Idaho State University, 2011.

[38] S. G. Swanekamp, J. P. Apruzese, R. J. Commisso, D. Mosher, and J. W. Schumer. An analysis of intense pulsed active detection (IPAD) for the detection

of special nuclear materials. In *Nuclear Science Symposium Conference Record (NSS/MIC), 2010 IEEE*, page 881. IEEE, 2010.

[39] Data produced by the code QCALC, written by T. W. Burrows, National Nuclear Data Center, Brookhaven National Laboratory, and based on the Audi-Wapstra Atomic Mass Tables, G. Audi and A. H. Wapstra. The 1995 update to the atomic mass evaluation. *Nuclear Physics A*, 595:409, 1995.

[40] N. Soppera, M. Bossant, and E. Dupont. JANIS 4: An improved version of the NEA Java-based nuclear data information system. *Nuclear Data Sheets*, 120:294.

[41] M. B. Chadwick, M. Herman, P. Oblozinsky, et al. ENDF/B-VII.1: Nuclear data for science and technology: Cross sections, covariances, fission product yields and decay data. *Nuclear Data Sheets*, 112:2887, 2011.

[42] J. Madalia. *Detection of Nuclear Weapons and Materials: Science, Technologies, Observations.* Diane Publishing Co., June 4 2010. Congressional Research Service R40154.

[43] E. Johnson, B. W. Blackburn, P. Hausladen, and M. Hynes. Optimizing inspection parameters for long stand-off detection of SNM. In *Applications of Nuclear Techniques*, number 1412, page 145. 2011 American Institute of Physics, 2011.

[44] E. A. Wulf, A. L. Hutcheson, B. F. Phlips, L. J. Mitchell, and B. E. Leas. Stand-off detection with an active interrogation photon beam. In *Nuclear Science Symposium and Medical Imaging Conference (NSS/MIC), 2011 IEEE*, page 315. IEEE, 2011.

[45] H. W. Koch and J. W. Motz. Bremsstrahlung cross-section formulas and related data. *Reviews of Modern Physics*, 31(4):920, 1959.

[46] L. I. Schiff. Energy-angle distribution of thin target bremsstrahlung. *Physical Review*, 83(2):252, 1951.

[47] J. D Jackson. *Classical Electrodynamics*. John Wiley & Sons, Inc., third edition, 1999.

[48] M. J. Berger and S. M. Seltzer. Bremsstrahlung and photoneutrons from thick tungsten and tantalum targets. *Physical Review C*, 2(2):621, 1970.

[49] T. Goorley, M. James, T. E. Booth, and T. Zukaitis. Initial MCNP6 release overview. *Nuclear Technology*, 180:298, 2012.

[50] R. J. Mcconn Jr., C. J. Gesh, R. T. Pagh, R. A. Rucker, and R. G. Williams III. Compendium of material composition data for radiation transport modeling. Technical Report PNNL-15870 Rev. 1, Pacific Northwest National Laboratory, 2011.

[51] J. G. Woodworth, K. G. McNeill, J. W. Jury, R. A. Alvarez, B. L. Berman, D. D. Faul, and P. Meyer. Photonuclear cross sections for ^{18}O. *Physical Review C*, 19(5):1667, 1979.

[52] F. M. Clikeman, A. J. Bureau, and M. G. Stewart. Photoproton reaction in Be^9. *Physical Review*, 126(5):1822, 1962.

[53] M. Goldhaber and E. Teller. On nuclear dipole vibrations. *Physical Review*, 74:1046, 1948.

[54] B. L. Berman and S. C. Fultz. Measurements of the giant dipole resonance with monoenergetic photons. *Reviews of Modern Physics*, 47(3):713, 1975.

[55] W. D. Myers, W. J. Swiatecki, T. Kodama, L. J. El-Jaick, and E. R. Hilf. Droplet model of the giant dipole resonance. *Physical Review C*, 15(6):2032, 1977.

[56] K. A. Snover. Giant resonances in excited nuclei. *Annual Review of Nuclear and Particle Science*, 36:545, 1986.

[57] Reinhard Stock, editor. *Encyclopedia of Nuclear Physics and its Applications*. Wiley-VCH, 2009.

[58] S. S. M. Wong. *Introductory Nuclear Physics.* John Wiley & Sons, Inc., 2 edition, 1998.

[59] A. V. Varlamov, V. V. Varlamov, D. S. Rudenko, and M. E. Stepanov. Atlas of giant dipole resonances. Technical Report INDC(NDS)-394, International Atomic Energy Agency International Nuclear Data Committee, 1999.

[60] A. Kamal. *Nuclear physics.* Springer-Verlag Berlin Heidelberg, 2014.

[61] J. T. Caldwell, E. J. Dowdy, and G. M. Worth. Prompt and delayed neutron yields from low energy photofission of ^{232}Th, ^{235}U, ^{238}U, and ^{239}Pu. Technical Report LA-UR-73-968, Los Alamos Sceintific Laboratory of the University of California, 1973.

[62] R. B. Walton, R. E. Sund, E. Haddad, and J. C. Young. Delayed gamma rays from photofission of U^{238}, U^{235}, and Th^{232}. *Physical Review*, 134(4B):B824, 1964.

[63] P. C. Fisher and L. B. Engle. Delayed gammas from fast-neutron fission of Th^{232}, U^{233}, U^{235}, U^{238}, and Pu^{239}. *Physical Review*, 134(4B):B796, 1964.

[64] L. Tomlinson. Theory of delayed-neutron physics. *Nuclear Technology*, 13:42, 1972.

[65] R. W. Waldo, R. A. Karam, and R. A. Meyer. Delayed neutron yields: Time dependent measurements and a predictive model. *Physical Review C*, 23(3):1113, 1981.

[66] G. R. Keepin, T. F. Wimett, and R. K. Zeigler. Delayed neutrons from fissionable isotopes of uranium, plutonium, and thorium. *Physical Review*, 107(4):1044, 1957.

[67] J. T. Caldwell and E. J. Dowdy. Experimental determination of photofission neutron multiplicities for ^{235}U, ^{236}U, ^{238}U, and ^{232}Th using monoenergetic photons. *Nuclear Science and Engineering*, 73:153, 1980.

[68] Edited by: D. Reilly, N. Ensslin, H. Smith, and S. Kreiner. Passive nondestructive assay of nuclear materials principles and applications. Technical report, National Technical Information Service, U.S. Department of Commerce, Washington DC, NUREG/CR-5550, 1991.

[69] H. Maier-Leibnitz et al. Prompt and delayed gamma-rays from fission. *Proceedings of a Symposium on the Physics and Chemistry of Fission*, 2:113, 1965.

[70] D. B. Pelowitz et al. MCNPX 2.7.0 extensions. Technical Report LA-UR-11-02295, Los Alamos National Laboratory, 2011.

[71] A. Veyssière, H. Beil, R. Bergère, P. Carlos, and A. Leprêtre and A. De Miniac. A study of the photoneutron contribution to the giant dipole resonance of the s-d shell nuclei. *Nuclear Physics A*, 227:513, 1974.

[72] R. B. Firestone. *Table of Isotopes.* John Wiley & Sons, Inc., eigth edition, 1999.

[73] J. K. Tuli. Evaluated nuclear structure data file. Technical Report BNL-NCS-51655-01/02-Rev, Bookhaven National Laboratory, Upton, New York, U.S.A., 2001.

[74] J. Blachot, W. Assal, P. Blaise, J-C. Bosq, S. Cathalau, P. J. Finck, et al. The Jef-2.2 nuclear data library. Technical report, Nuclear Energy Agency Organisaton for Economic Co-Operation and Development, April 2000.

[75] A. J. Koning and D. Rochman. Modern nuclear data evaluation with the TALYS code system. *Nuclear Data Sheets*, 113:2841.

[76] N. Otuka, E. Dupont, V. Semkova, B. Pritychenko, A. I. Blokhin, M. Aikawa, S. Babykina, et al. Towards a more complete and accurate experimental nuclear reaction data library (EXFOR): International collaboration between nuclear reaction data centres (NRDC). *Nuclear Data Sheets*, 120:272.

[77] A. P. Komar and Eu. D. Makhnovsky. Photodisintegration of Be^9. *Nuclear Physics*, 65:662, 1965.

[78] V. S. Bohinyuk, V. I. Zhaba, A. M. Parlag, and L. O. Shabalina. Research of excitation of the isomers states in (gamma, n)-reactions. *Naukovny Visnyk Uzhgorods'kogo Univ., Ser. Fiz.*, 32:39, 2012.

[79] D. Zubanov, R. A. Sutton, and M. N. Thompson. ^{13}C(γ,p) cross section. *Physical Review C*, 27(5):1957, 1983.

[80] C. Plaisir F. Hanachi, F. Govet, M. Tarisien, et al. Measurement of the ^{85}Rb(γ,n)^{84m}Rb cross-section in the energy range 10-19 MeV with bremsstrahlung photons. *The European Physical Journal A*, 48:68, 2012.

[81] O. A. Bezshyyko et al. Isomer ratios for ^{52}Mg-product of photonuclear reaction ^{54}Fe(γ,np)^{52m,g}Mg. *4 Int. Conf. Cur. Prob. in Nucl. Phys. Atom. Ene., Kyiv*, 2012:132, 2013.

[82] S. S. Borodina et al. ^{54,56}Fe and ^{58,60}Ni(γ,n),(γ,p),(γ,np), and (γ,2n) cross sections evaluation using the model of GDR decay channel competition phenomenological description. *Moscow State Univ. Inst. of Nucl. Phys. Reports*, (200-6/610), 2000.

[83] P. Carlos et al. A study of the photneutron contribution to the giant dipole resonance of nuclei in the 64 $\leqq$ A $\leqq$ 86 mass region. *Nuclear Physics A*, 258:365, 1976.

[84] D. V. Webb, E. G. Muirhead, and B. M. Spicer. The ^{39}K photoneutron cross-section to the ^{38}K isomeric state. *Nuclear Physics A*, 171:324, 1971.

[85] L. A. KulĆhitskiy, Yu. M. Volkov, and V. P. Denisov. The Li-7 levels in it's photodisintegration. *Izv. Rossiiskoi Akademii Nauk, Ser. Fiz.*, 27:1412, 1963.

[86] S. C. Fultz et al. Photoneutron cross sections for ^{24}Mg, ^{26}Mg and natural magnesium. *Physical Review C*, 4(1):149, 1971.

[87] B. S. Ishkhanov. Decay channels of the giant dipole resonance in ^{26}Mg. *Nuclear Pphysics A*, 313:317, 1979.

[88] M. G. Davydov, V. G. Magera, and A. V. Trukhov. The isomeric ratio of the photonuclear reactions yields (cross sections). *Atomnaya Energiya*, 62:236, 1987.

[89] S. C. Fultz et al. Photoneutron cross sections of ^{58}Ni and ^{60}Ni. *Physical Review C*, 10(2):608, 1974.

[90] P. Carlos et al. Photoneutron cross sections for oxygen from 24-133 MeV. *Nuclear Physics A*, 378:317, 1982.

[91] K. G. McNeill, J. W. Jury, M. N. Thompson, B. L. Berman, and R. E. Pywell. ^{18}O(γ,pn + np) cross section. *Physical Review C*, 43(2):489.

[92] D. W. Anderson et al. Photoneutron cross sections for ^{32}S. *Nuclear Physics A*, 156:74, 1970.

[93] R. E. Pywell. Photoneutron cross sections for the silicon isotopes. *Physical Review C*, 27(3):960, 1983.

[94] T. E. Rodrigues, J. D. T. Arruda-Neto, Z. Carvalheiro, J. Mesa, A. Deppman, V. P. Likhachev, and M. N. Martins. Statistical and direct aspects of ^{64}Zn (γ,n) and (γ,np) decay channels in the giant dipole resonance and quasideuteron energy regions. *Physical Review C*, 68:014618–1, 2003.

[95] V. V. Varlamov et al. New data on cross sections for partial and total photoneutron reactions on the isotopes ^{91,94}Zr. *Yadernaya Fizika*, 78:634, 2015.

[96] L. A. Currie. Limits for qualitative detection and quantitative determination. *Application to Radiochemistry*, 40:586, 1968.

[97] G. Audi and A. H. Wapstra. The 1993 atomic mass evaluation: (i) atomic mass table. *Nuclear Physics A*, 565:1, 1993.

[98] G. Audi and A. H. Wapstra. The 1995 update to the atomic mass evaluation. *Nuclear Physics A*, 595:409, 1995.

[99] Berkeley Nucleonics Corp. *575 Series Pulse Generator Operating Manual*, 5.6 edition.

[100] ORTEC. *Model 672 Spectroscopy Amplifier Operating and Service Manual.*

[101] ORTEC. *Model 113 Scintillation Preamplifier Operating and Service Manual.*

[102] ORTEC. *Model 855 Dual Spectroscopy Amplifier Operating and Service Manual.*

[103] H. Naik, G. N. Kim, R. Schwengner, K. Kim, M. Zaman, et al. Photo-neutron reaction cross-sections for ^{nat}Zr in the bremsstrahlung end-point energies of 12-16 and 45-70 MeV. *The European Physical Journal A*, 50(83), 2014.

[104] M. Zaman et al. Flux-weighted average cross-sections of ^{nat}Ag(γ, xn)$^{103-106}$Ag reactions with end-point bremsstrahlung energies of 45-60 MeV. *The European Physical Journal A*, 1(5), 2014.

[105] D. E. Alburger and G. A. P. Engelbertink. Half-lives of Be^{11}, C^{15}, N^{16}, O^{19}, and Al^{28}. *Physical Review C*, 2(5):1594, 1970.

[106] M. G. Silbert and J. C. Hopkins. Beta decay of N^{17} to bound states in O^{17}. *Physical Review*, 134(1B):B16, 1964.

[107] D. E. Alburger. Half-lives of ^{17}N and ^{17}F. *Physical Review C*, 6(6):2019, 1972.

[108] A. R. Poletti and J. G. Pronko. Beta decay of ^{17}N. *Physical Review C*, 8(4):1285, 1973.

[109] P. De Bièvre and P. D. P. Taylor. Table of the isotopic compositions of the elements. *International Journal of Mass Spectrometry and Ion Processes*, 123:149, 1993.

[110] Michael Fleischer. Recent estimates of the abundances of the elements in the earth's crust. Number 285 in Circular. U.S. Geological Survey, 1953.

[111] T. J. Ahrens. *Global Earth Physics:A Handbook of Physical Constants.* American Geophysical Union, 1995.

[112] K. E. Sale, T-F. Wang, R. N. Boyd, G. J. Mathews, D. W. Heikkinen, and M. L. Roberts. Measurement of the half-life of ^{8}Li. *Physical Review C*, 41(5):2418, 1990.

[113] G. Audi, O. Bersillon, J. Blachot, and A. H. Wapstra. The NUBASE evaluation of nuclear and decay properties. *Nuclear Physics A*, 729:3, 2003.

[114] R. R. Harvey, J. T. Caldwell, R. L. Bramblett, and S. C. Fultz. Photoneutron cross sections of Pb^{206}, Pb^{207}, Pb^{208}, and Bi^{209}. *Physical Review*, 136(1B):B126, 1964.

[115] P. A. Cox. *The Elements: Their Origin, Abundance and Distribution.* Oxford University Press, 1989.

[116] J. Emsley. Nature's building blocks: An A-Z guide to the elements. 2003.

[117] A. Veyssière, H. Beil, R. Bergere, P. Carlos, A. Lepretre, and A. De Miniac. A study of the photoneutron contribution to the giant dipole resonance of the s-d shell nuclei. *Nuclear Physics Section A*, 227:513, 1974.

[118] Thomas Jefferson National Accelerator Facility Office of Science Education. *It's Elemental*, 2013 (accessed June 29, 2015). `http://education.jlab.org/itselemental/`.

Appendix A

Observed Reactions

A.1 List of Observed Reactions

Table A.1: Observed Reactions

Sample	Parent	Reaction	Product	Signature	Mass[c] (g)	Peak Eng. (keV) †,[o,*]	Page
Aluminum lump	^{27}Al	(γ,^{3}He)	^{24}Na	β, γ	128	1368.6	143
Aluminum lump	^{27}Al	(γ,^{3}He)	^{24}Na	β, γ	128	2754	144
Aluminum lump	^{27}Al	(γ,2p)	^{25}Na	β	128	974.7, 1611.7	143
Argon	^{40}Ar	(γ,p)	^{39}Cl	β	380	1267.185	117
Argon	^{40}Ar	(γ,p)	^{39}Cl	β	380	1517.508	117
Argon	^{40}Ar	(γ,np)	^{38}Cl	β	380	1642.714	117
Argon	^{40}Ar	(γ,np)	^{38}Cl	β	380	2167.405	117
Argon	^{40}Ar	(γ,^{3}He)	^{37}S	β, γ	380	3103.36	118
Borax	^{10}B	(γ,2p)	^{8}Li	β	105	12965.0	140
Borax	^{11}B	(γ,2p)	^{9}Li	β, n	105	13.606	140
BN					67		139
Beryllium block	^{9}Be	(γ,p)	^{8}Li	β	561	12965.0	71
KBr	^{79}Br	(γ,n)	^{78}Br	β, γ	176	613.68	133
Calcium shots	^{40}Ca	(γ,np)	^{38}K	β, γ	63	2167.5	119,71
Concrete brick					338		152
Salt (iodide free)	^{35}Cl	(γ,n)	^{34m}Cl	β, γ	127	3304.039	76
Salt water					783		125
Salt (iodide free)	^{35}Cl	(γ,n)	^{34m}Cl	β, γ	127	2127.492	76
Salt (iodide free)	^{35}Cl	(γ,n)	^{34m}Cl	β, γ	127	1176.626	76

Continued on next page.

†The energy listed is the endpoint energy of the β-particle when no decay peak is observed.

[c]The in-beam mass is calculated from the sample.

[o] [40],[*] [41],[b] [74]

Table A.1 Observed Reactions Continued

Sample	Parent	Reaction	Product	Signature	Mass[c] (g)	Peak Eng. (keV) †,o,*	Page
Copper brick	^{63}Cu	(γ,n)	^{62}Cu	β, γ	767	1172.9, 2301.8	145
LiF	^{19}F	(γ,^{3}He)	^{16}N	β, γ	66	6128.630	67
KF				γ	59		137
C_2F_4				γ	553		149, 150
LiF	^{19}F	(γ,2p)	^{17}N	β, γ, n	66		121
Iron granules	^{54}Fe	(γ,np)	^{52m}Mn	β, γ	396	1434.06	132
Iron granules	^{57}Fe	(γ,p)	^{56}Mn	γ	396	1810.72, 2113.05	132
Iron granules	^{58}Fe	(γ,np)	^{56}Mn	γ	396	1810.72, 2113.05	132
Concrete brick	$^{39/40/41}$K	(γ,n/2n/3n)	^{38}K	β, γ	338	2167.5	152
KBr	$^{39/40/41}$K	(γ,n/2n/3n)	^{38}K	β, γ	176	2167.5	134
K D-gluconate	$^{39/40/41}$K	(γ,n/2n/3n)	^{38}K	β, γ	73	2167.5	135
KF	$^{39/40/41}$K	(γ,n/2n/3n)	^{38}K	β, γ	59	2167.5	136
BN	^{15}N	(γ,2p)	^{13}B	β, γ, n	67	13437.2	139
Salt (iodide free)	^{23}Na	(γ,^{3}He)	^{20}F	β, γ	127	1633.6	76
Nickel plate	^{58}Ni	(γ,n)	^{57}Ni	γ	96	1377.6, 1757.6, 1919.5	146
Nickel plate	^{64}Ni	(γ,np)	^{62}Co	β, γ	96	1172.9	146
Water (deionized)	^{16}O	(γ,2n)	^{14}O	β, γ	757	2312.6	123
Salt water					783		126
SiO_2					148		130
Concrete brick					338		152
O-18 water	^{18}O	(γ,np)	^{16}N	β, γ	50	6128.630	67,120
Water (deionized)					757		122
Salt water					783		126
Watermelon					217		127
Beef					409		128
SiO_2					148		129
Wood					152		131
Concrete brick					338		151
^{18}O water	^{18}O	(γ,np)	^{16}N	β, γ	50	7115.150	67,120
^{18}O water	^{18}O	(γ,p)	^{17}N	β, γ, n	50	870.71	70
S	$^{32/33/34}$S	(γ,n/2n/3n)	^{31}S	β, γ	88	1266.2	141
S	$^{32/33/34}$S	(γ,n/2n/3n)	^{31}S	β, γ	88	3134.1	142
SiN	^{28}Si	(γ,n)	^{27}Si	β	63	2210.5	138
SiO_2					148		130
Concrete brick					338		152
Zinc shots	^{64}Zn	(γ,n)	^{63}Zn	β, γ	316	669.6, 962.1, 1412.1	147
Zirconium plate	^{96}Zr	(γ,p)	^{95}Y	β, γ	165	3576.0	148

A.2 Observed Peaks, Bremsstrahlung Curves, and Neutron Yields

Reaction activity is indicated in the graphs presented in this section. Graphs with decay peaks below 3 MeV were included in cases where branching ratios for γ-rays with energy above 3 MeV were insufficient to produce observable peaks in the time frame examined. Graphs with decay peaks below 3 MeV were also presented when γ-rays with energies below the signature region were observed, however, β-particles with energies above 3 MeV contributed to the increased yields. Isotopic abundances, half-lives, and reaction thresholds are listed in Tables B.1, 2.1, 2.2, and 2.3. Discrete peaks were observed from the HPGe detector with bremsstrahlung and neutron curves generated from the BGO and ^{3}He proportional counters respectively.

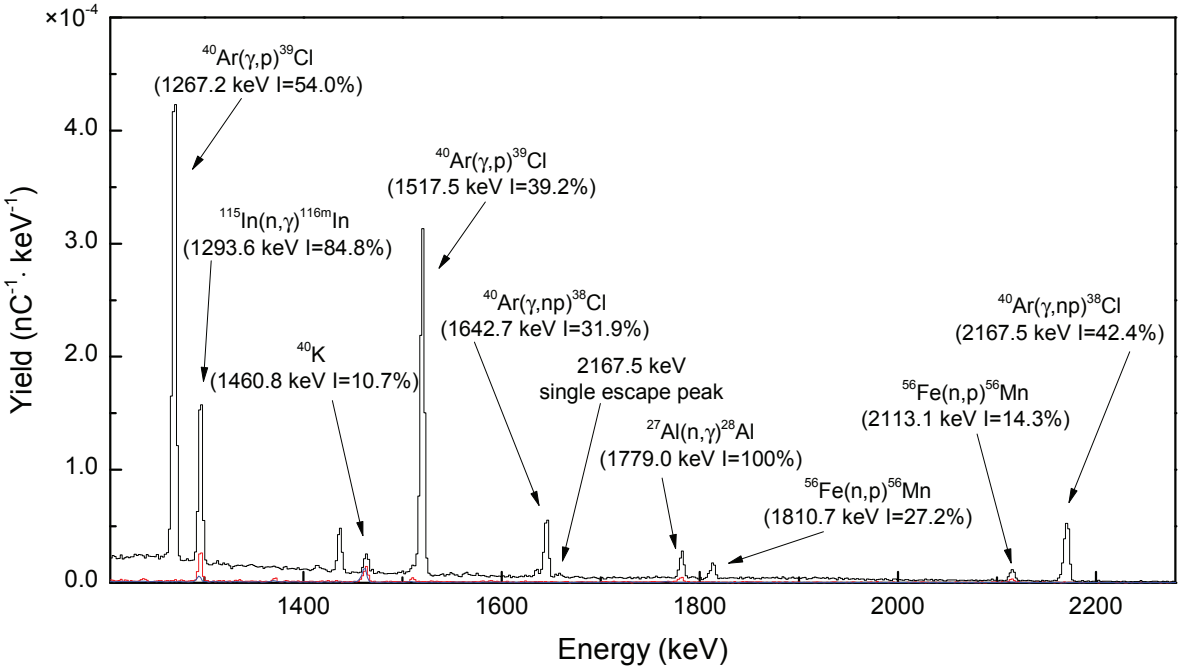

Figure A.2.1: Argon (black) energy spectrum with several peaks from the decay of ^{38}Cl and ^{39}Cl displayed. The reactions producing peaks result from the photodisintegration of ^{40}Ar. Active (red) and passive (blue) no-target inspections are shown for comparison. A 0.88 g in-beam mass of argon was irradiated at a bremsstrahlung endpoint energy of 37 MeV produced from electrons having an average charge per pulse of 169.1 nC over 33760 pulses and both active inspections. The 1810.7 and 2113.1 keV photopeaks result from the decay of ^{56}Mn produced in the carbon steel canister holding the argon. Concrete in the building and indium near the detector produce reactions that result in the other peaks shown.

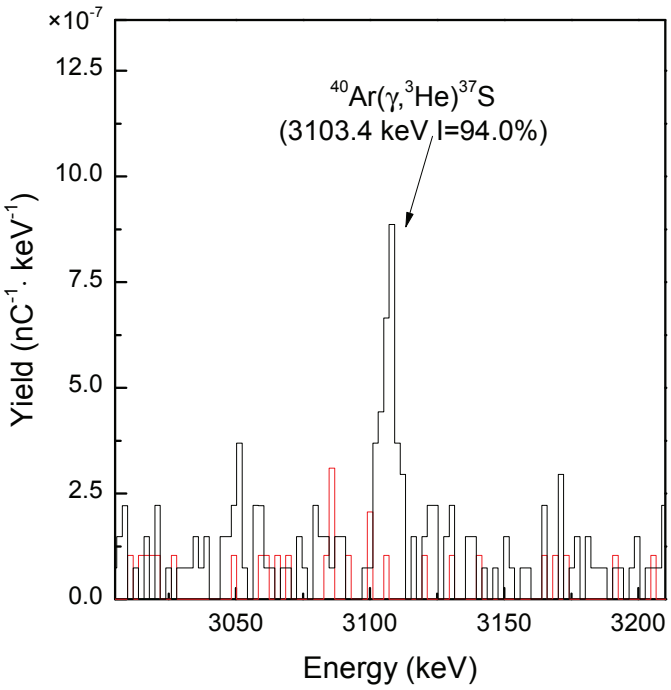

Figure A.2.2: Argon (black) energy spectrum displaying the 3103.4 keV peak resulting from the decay of ^{37}S following its transmutation from ^{40}Ar. Active (red) and passive (blue) no-target inspections are also shown with experimental parameters equal to those described in Figure A.2.1.

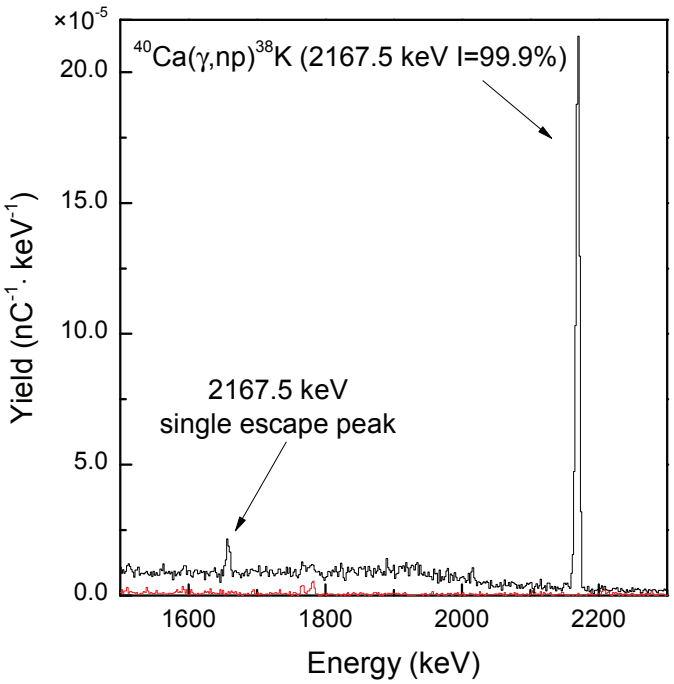

Figure A.2.3: Calcium (black) energy spectrum showing 2167.5 keV and single escape peaks from the decay of ^{38}K following the photodisintegration of ^{40}Ca. The no-target inspection (red) is shown for comparison to the calcium curve that is produced from an in-beam mass of 62.5 g. An average charge per pulse of 55.2 nC, averaged over both inspections and 33420 pulses, characterizes electrons producing a 45 MeV endpoint energy bremsstrahlung beam.

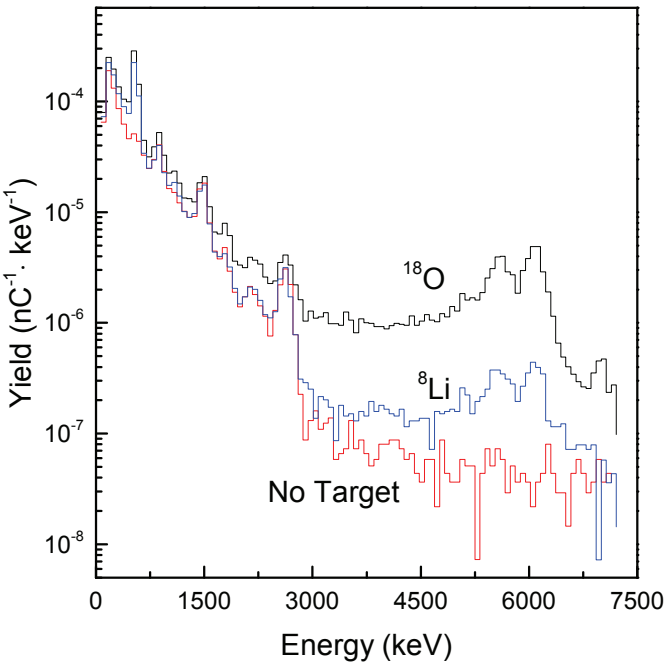

Figure A.2.4: Energy spectra displaying ^{16}N 6128.6 keV photo and single escape decay peaks produced in ^{18}O (black) and LiF (blue) with a no-target inspection (red) also shown. Targets were irradiated with a 45 MeV endpoint energy pulsed bremsstrahlung beam. The charge per pulse of 53.2 nC was averaged over the targets displayed and 33822 pulses. The in-beam masses of the ^{18}O and LiF samples were 42 and 66 g respectively. The bremsstrahlung curve is generated by high-energy β-particles interacting with nuclei in the targets.

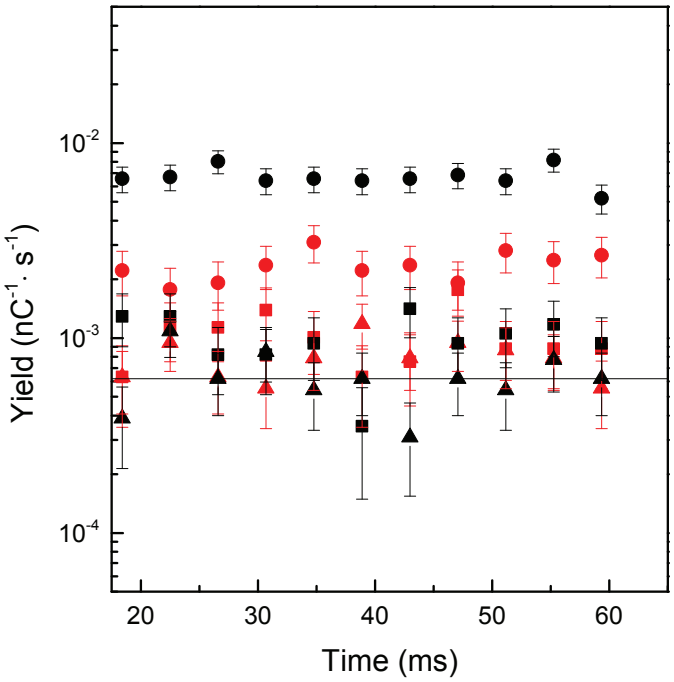

Figure A.2.5: Neutron time spectrum for the LiF (black) sample and an active no-target inspection (red) with both targets irradiated at 15 (■), 22.5 (▲), and 37.5 MeV (•). The charge per pulse averaged over all energies and 9162 pulses for both activated samples was 246.8 nC. The passive no-target inspections (solid) is normalized to the average active charge.

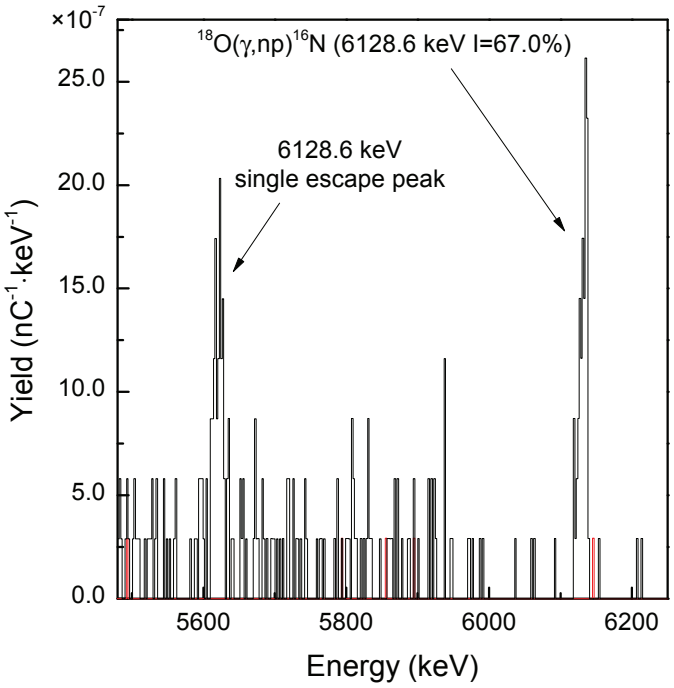

Figure A.2.6: Deionized water (black) energy spectrum with ^{16}N 6128.6 keV decay and single escape peaks resulting from the photodisintegration of ^{18}O shown and compared with active (red) and passive (blue) no-target inspections. An average charge per pulse of 184.0 nC averaged over both active inspections and 9073 pulses produce the bremsstrahlung beam with an endpoint energy of 37.5 MeV.

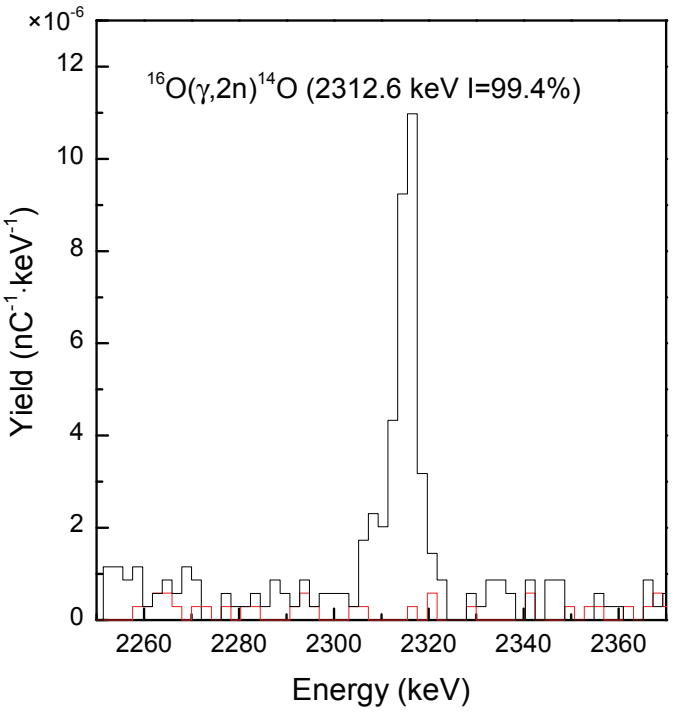

Figure A.2.7: Deionized water energy spectrum (black) displaying the ^{14}O 2312.6 keV decay peak resulting from ^{16}O(γ,2n) reactions. No-target active (red) and passive (blue) spectra are shown for comparison. Accelerator parameters match those described in Figure A.2.6.

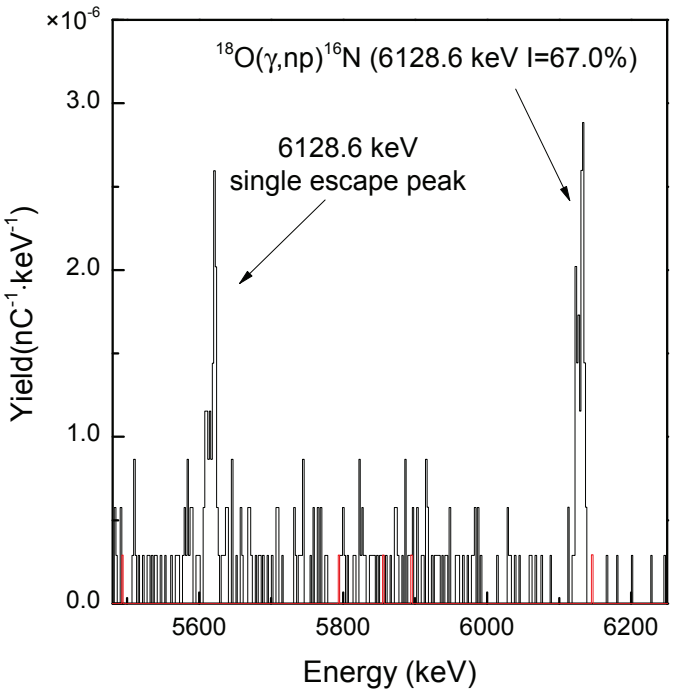

Figure A.2.8: Salt water (black) energy spectrum showing 6128.6 keV decay and single escape peaks from the decay of ^{16}N transmuted from ^{18}O. The active no-target inspection (red) is shown for comparison to the saltwater curve that is produced from an in-beam mass of 783 g. Accelerator parameters include a charge of 185.0 nC averaged over both samples and 9056 pulses and a bremsstrahlung beam with endpoint energy of 37.5 MeV.

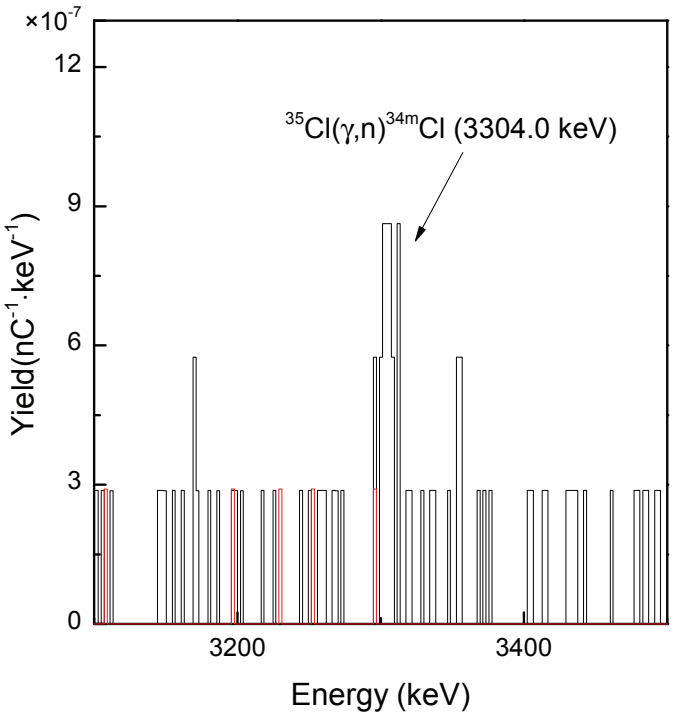

Figure A.2.9: Salt water (black) energy spectrum showing 3304.0 keV ^{34m}Cl decay peak from ^{35}Cl(γ,n) reactions. The active no-target (red) is shown for comparison with inspection characteristics identical to those described in Figure A.2.8.

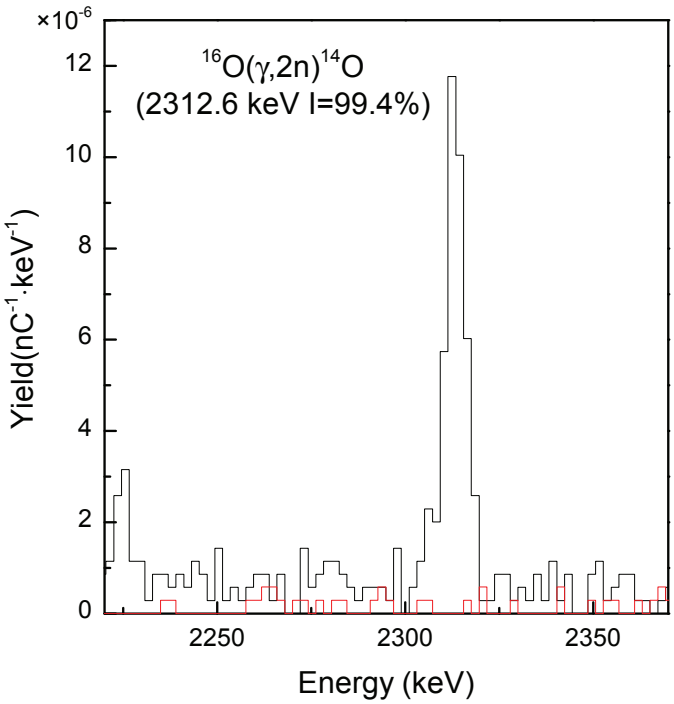

Figure A.2.10: Salt water (black) energy spectrum showing 2312.6 keV decay peak from the $^{16}O(\gamma,2n)^{14}O$ reaction. The active no-target (red) is shown for comparison with inspection characteristics identical to those described in Figure A.2.8.

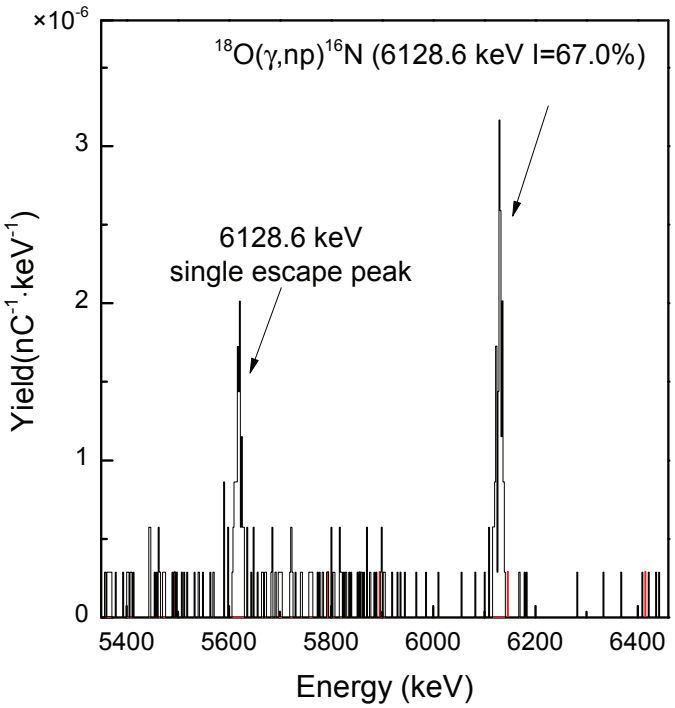

Figure A.2.11: Watermelon (black) energy spectrum displaying 6128.6 keV photo and single escape peaks resulting from the decay of ^{16}N followed by the photodisintegration of ^{18}O. The watermelon in-beam mass measured 217 g. The active no-target (red) is displayed for comparison. The electron charge per pulse is 184.0 nC averaged over both activated targets and 9041 pulses producing the 37.5 MeV endpoint energy bremsstrahlung beam.

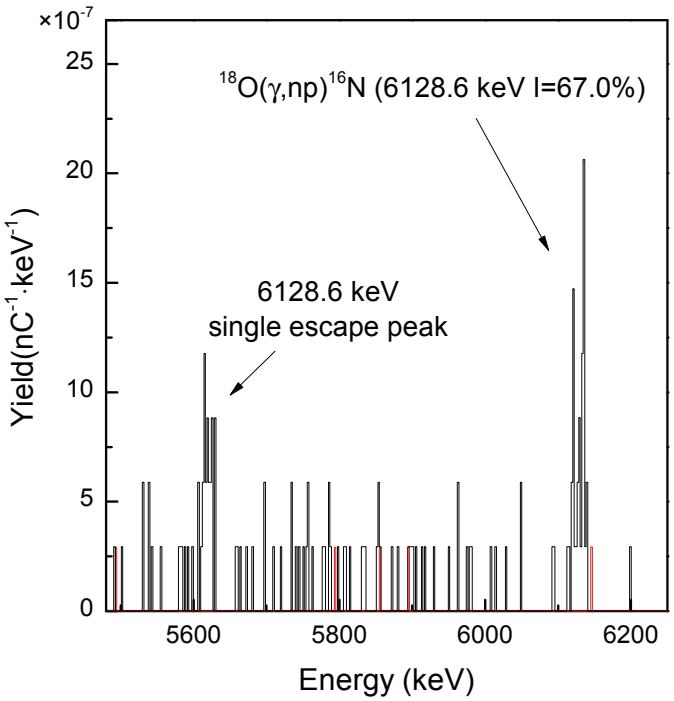

Figure A.2.12: Beef (black) energy spectrum produced from the decay of ^{16}N following the photodisintegration of ^{18}O. The 6128.6 keV photo and single escape peaks are produced from a 409 g in-beam mass of beef. An active no-target inspection (red) is also shown. The accelerator produced an average charge of 183.0 nC over both samples and 9036 pulses generating a bremsstrahlung beam with endpoint energy of 37.5 MeV.

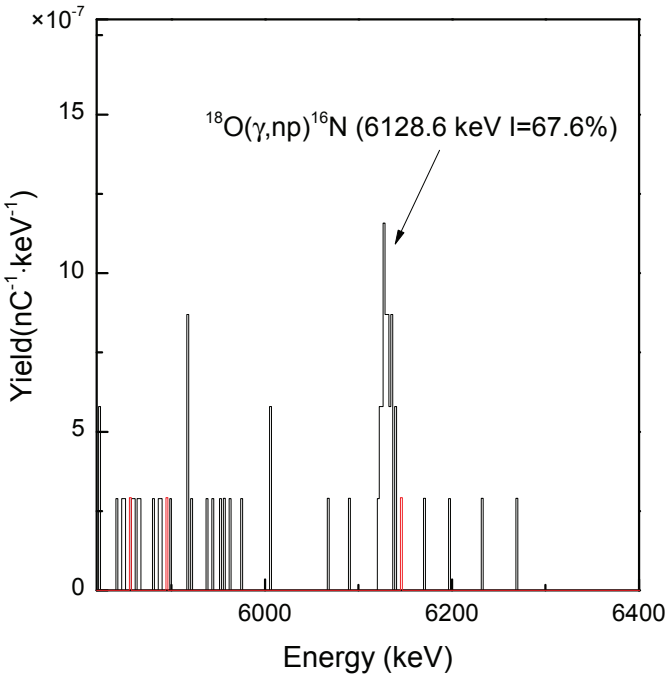

Figure A.2.13: SiO_2 (black) energy spectrum showing the 6128.6 keV decay peak produced from ^{16}N transmuted from ^{18}O. An in-beam mass of 148 g was irradiated as well as a no-target (red) displayed for comparison. Utilizing a 37.5 MeV endpoint energy bremsstrahlung beam, the average charge per pulse was 185.0 nC averaged over both samples and 9033 pulses.

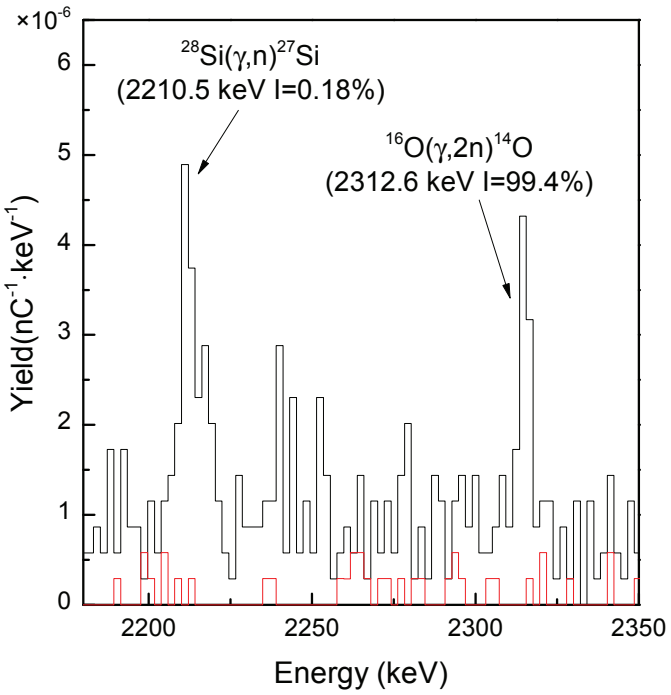

Figure A.2.14: SiO_2 (black) energy spectra displaying $^{16}O(\gamma,2n)^{14}O$ and $^{28}Si(\gamma,n)^{27}Si$ 2312.6 keV and 2210.5 keV reaction product decay peaks respectively. An active no-target inspection (red) is also displayed. Accelerator parameters are identical to those mentioned in Figure A.2.13.

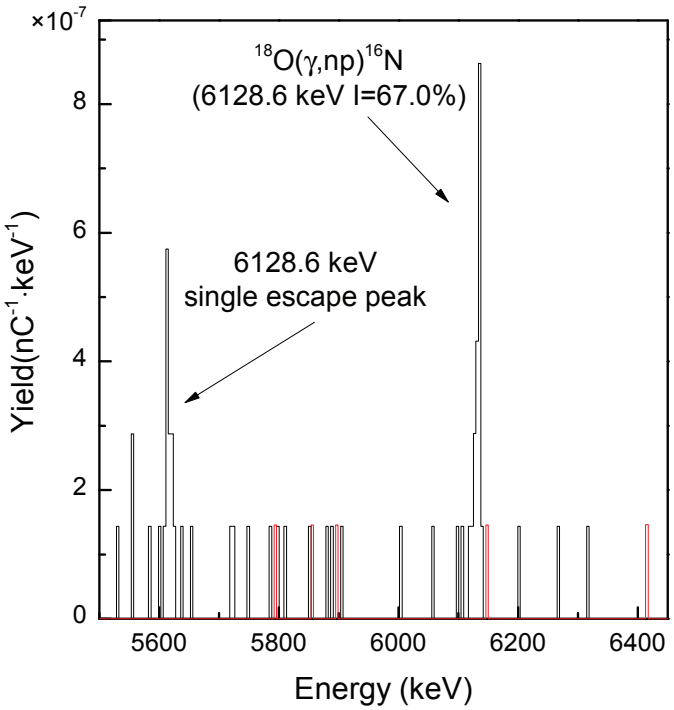

Figure A.2.15: Wood (black) energy spectrum with the 6128.6 keV ^{16}N decay peak resulting from the photodisintegration of ^{18}O displayed. An in-beam wood mass of 152 g produces the spectrum that is compared to an active no-target inspection (red). The 184.7 nC mean charge per pulse and 9086 pulses were averaged over both targets that were irradiated with a 37.5 MeV endpoint energy bremsstrahlung beam.

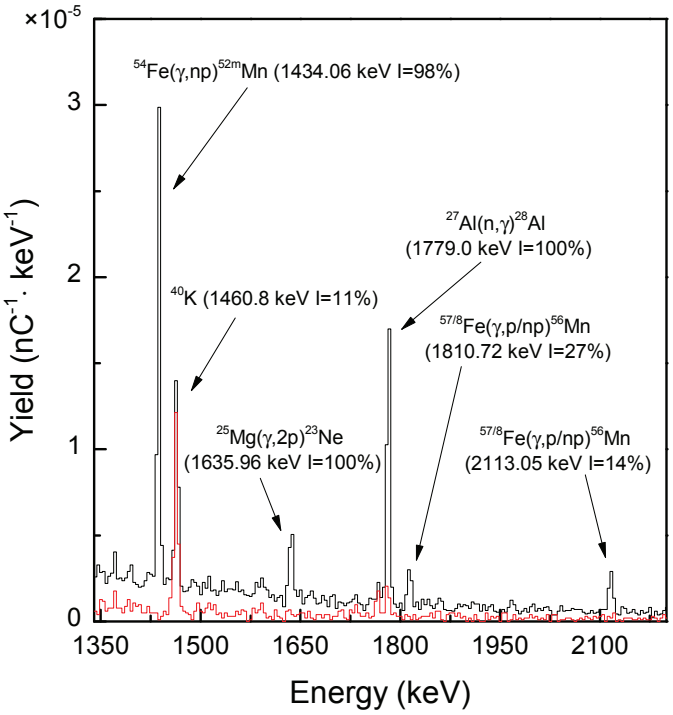

Figure A.2.16: Iron (black) energy spectrum with a no-target (red) shown for comparison. Decay peaks from ^{52m}Mn and ^{56}Mn are observed and are evidence of the photodisintegration of ^{54}Fe and ^{58}Fe respectively. Reactions resulting from the decay of ^{56}Mn following ^{57}Fe(γ,p) processes are also observed. The bremsstrahlung endpoint energy of 39 MeV was generated from electrons with a mean charge per pulse of 183.2 nC averaged over the two targets and 18790 pulses.

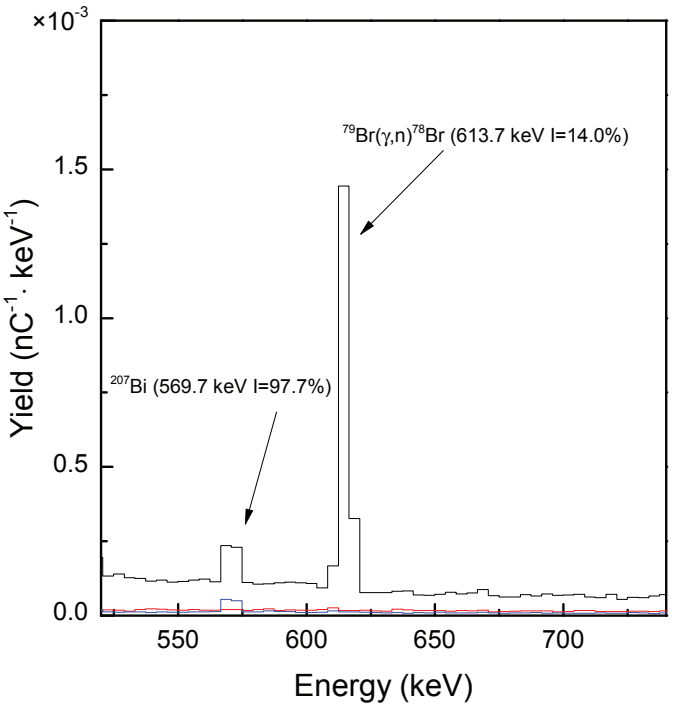

Figure A.2.17: KBr (black) energy spectrum along with no-target active (red) and passive (blue) inspections displayed. The 613.7 keV peak is from the decay of ^{78}Br produced from the ^{79}Br(γ,n) reaction. The electron charge per pulse was 52.0 nC averaged over the active inspections and 21611 pulses. Peaks resulting from the decay of ^{207}Bi were likely produced in the environment from prior experiments. Bismuth-207 is a long lived radionuclide that has a half-live of 31.55 years [40, 41].

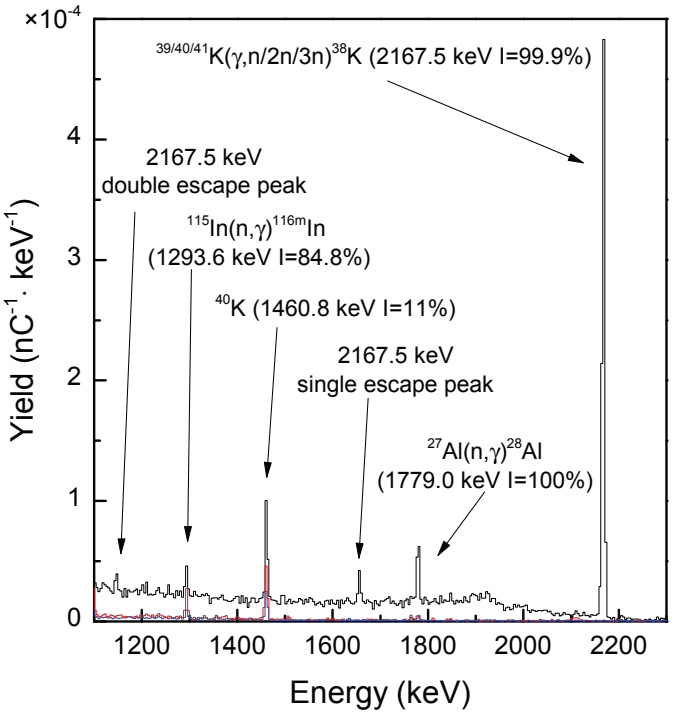

Figure A.2.18: KBr (black) energy spectrum with no-target active (red) and passive (blue) inspections displayed. Decay photo, single, and double escape 2167.5 keV peaks from ^{38}K are created by the $^{39/40/41}$K(γ,n/2n/3n) reactions. Accelerator parameters match those in Figure A.2.17. Additional peaks shown result from activity in the experimental environment and are described in the NaCl graph of Figure 4.12.

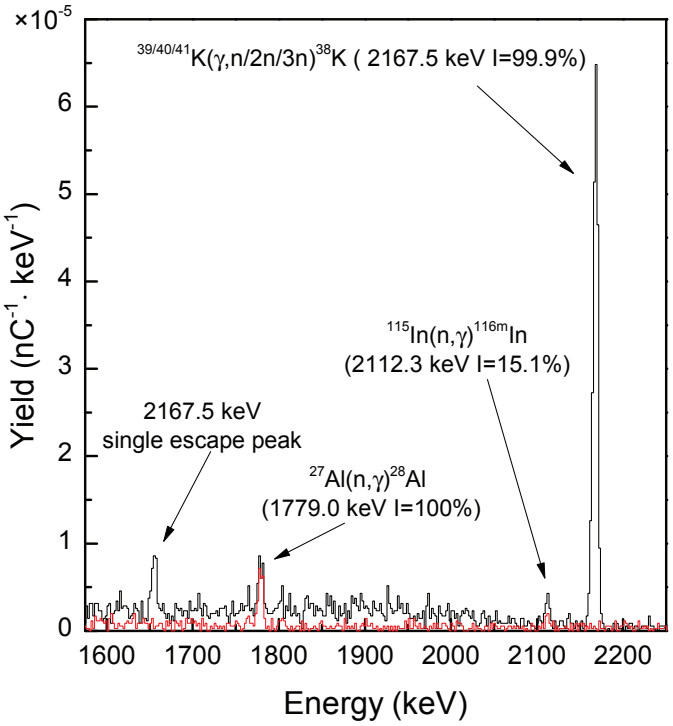

Figure A.2.19: Potassium D-gluconate (black) energy spectrum with a no-target inspection (red) displayed for comparison. The 2167.5 keV photo and single escape peaks result from the decay of ^{38}K that is generated by the $^{39/40/41}$K(γ,n/2n/3n) reactions. The bremsstrahlung endpoint energy was 37.5 MeV initiated by electrons with a charge per pulse of 186.0 nC averaged over both targets and 9055 pulses. Additional background peaks are described in Figures A.2.1 and 4.12.

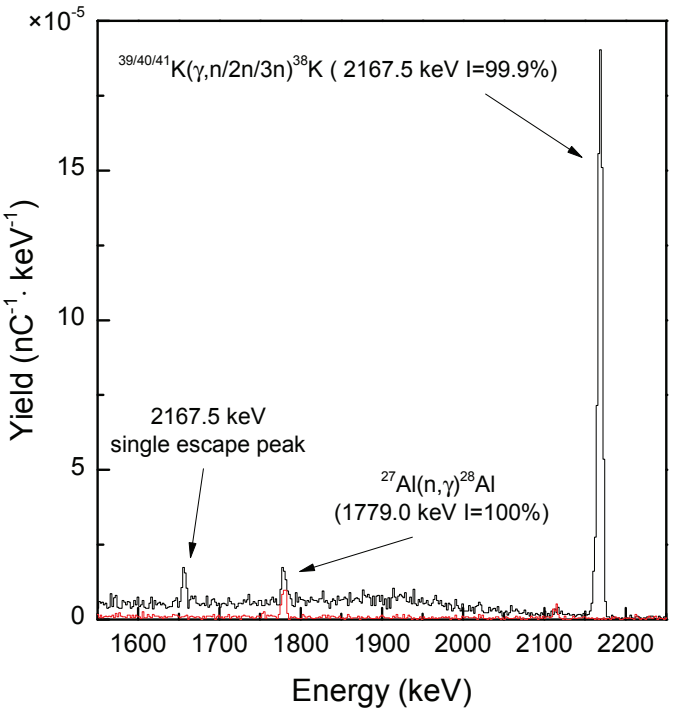

Figure A.2.20: Energy spectra showing KF (black) and a no-target inspection (red). The decay of ^{38}K resulting from the $^{39/40/41}$K(γ,n/2n/3n) reactions is shown in the 2167.5 keV and 1656.5 keV photo and single escape peaks respectively. The KF sample measures 60 g (in-beam). Electrons generated a target average charge per pulse of 185.0 nC and a 37.5 MeV endpoint energy bremsstrahlung beam that operated for ~ 9028 pulses.

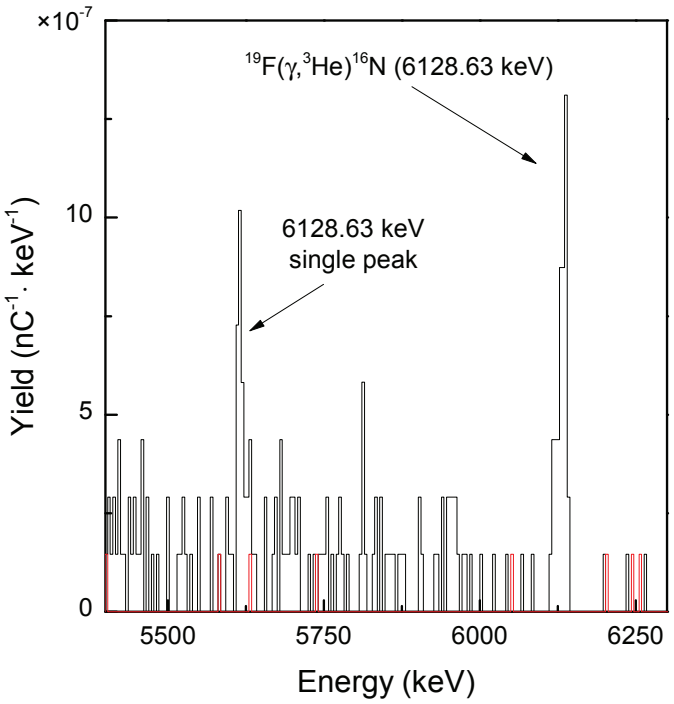

Figure A.2.21: Potassium fluoride (black) and no-target (red) energy spectra focused around the 6128.6 keV photo and single escape peaks resulting from the decay of ^{16}N. Reactions were initiated from ^{19}F. Accelerator parameters matched those described in A.2.20.

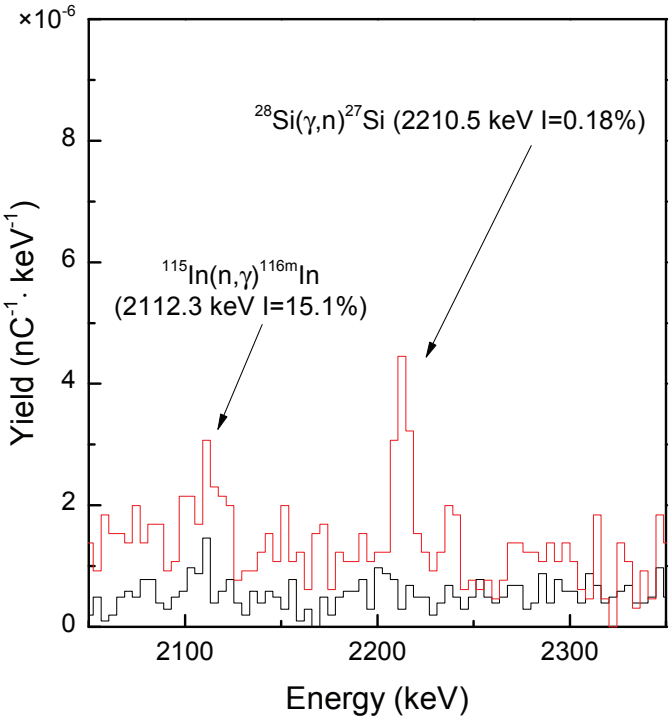

Figure A.2.22: Silicon Nitride (black) and no-target (red) energy spectra. The 2210.5 keV decay peak is observed following the ^{28}Si(γ,n)^{27}Si reaction. Accelerator parameters include a bremsstrahlung beam generated by an electron energy of 44.75 MeV and a charge averaged over both targets and 37221 pulses of 55.4 nC.

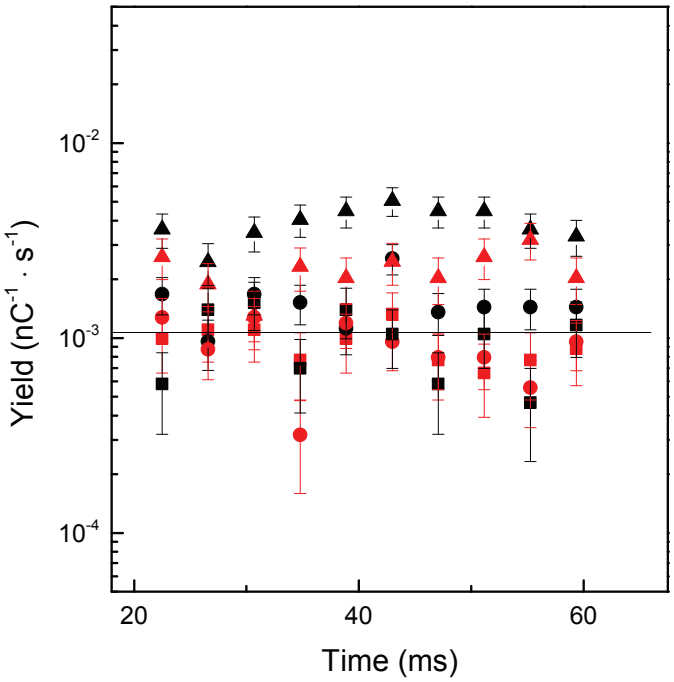

Figure A.2.23: Time spectrum showing boron nitride (black) and a no-target inspection (red) irradiated at bremsstrahlung endpoint energies of 15 (■), 30 (•), and 37.5 MeV (▲). A no-target passive (solid) inspection is included for comparison. Neutrons are emitted following the decay of the reaction product from both the ^{11}B(γ,2p)^{9}Li and ^{15}N(γ,2p)^{13}B reactions beyond threshold energies of 30.9 and 31.0 MeV respectively.

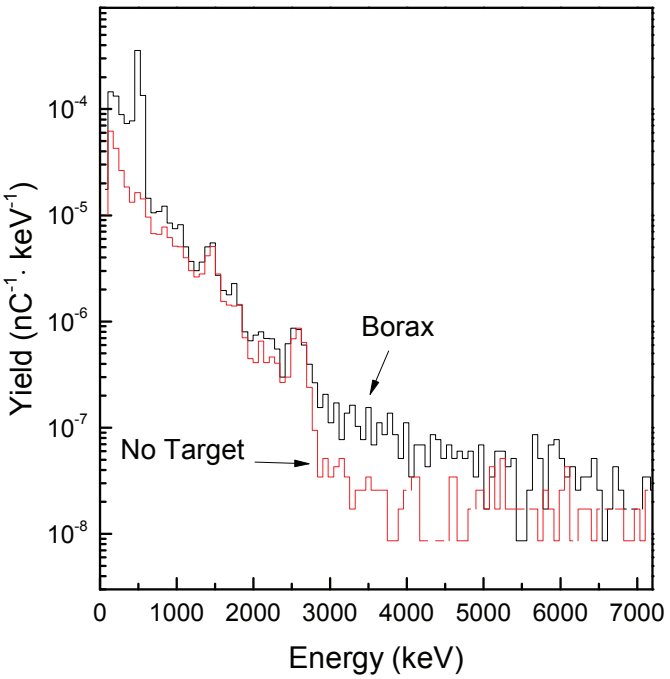

Figure A.2.24: Borax (black) and no-target (red) energy spectra observed with the BGO detectors and the accelerator operating at 37.5 MeV. Electrons produced an average charge of 183.8 nC per pulse over both targets and 9063 pulses. The emission of β-particles follow the decay of ^{9}Li produced from the ^{11}B(γ,2p) reaction.

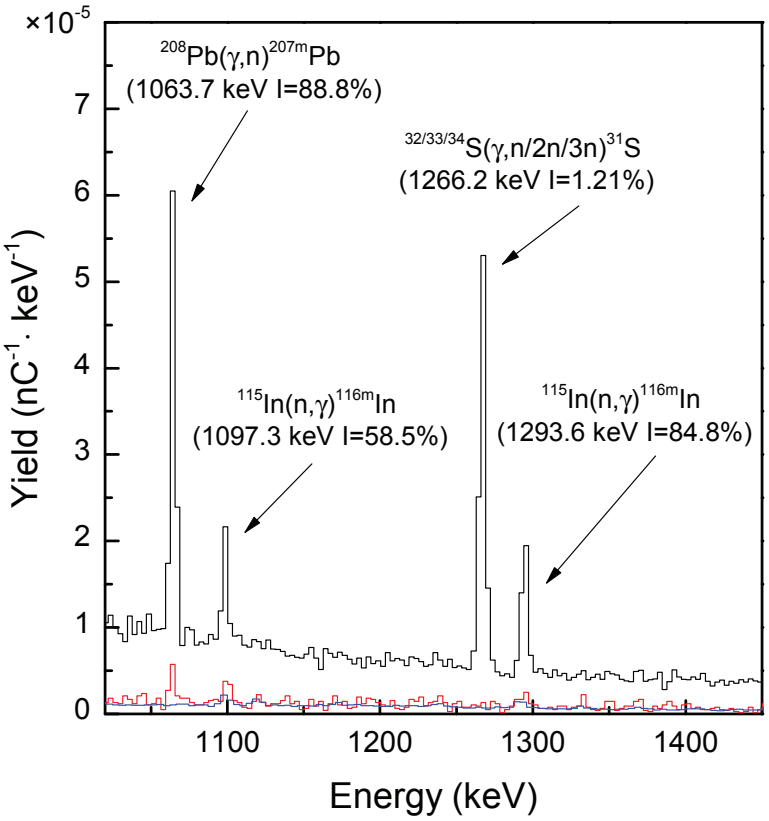

Figure A.2.25: Sulfur (black) energy spectrum showing ^{31}S 1266.2 keV decay peak resulting from $^{32/33/34}$S(γ,n/2n/3n) reactions. No-target active (red) and passive (blue) inspections are displayed for comparison. Electrons produced a mean charge per pulse of 183.2 nC averaged over 21897 pulses. A 39 MeV endpoint energy bremsstrahlung beam was utilized.

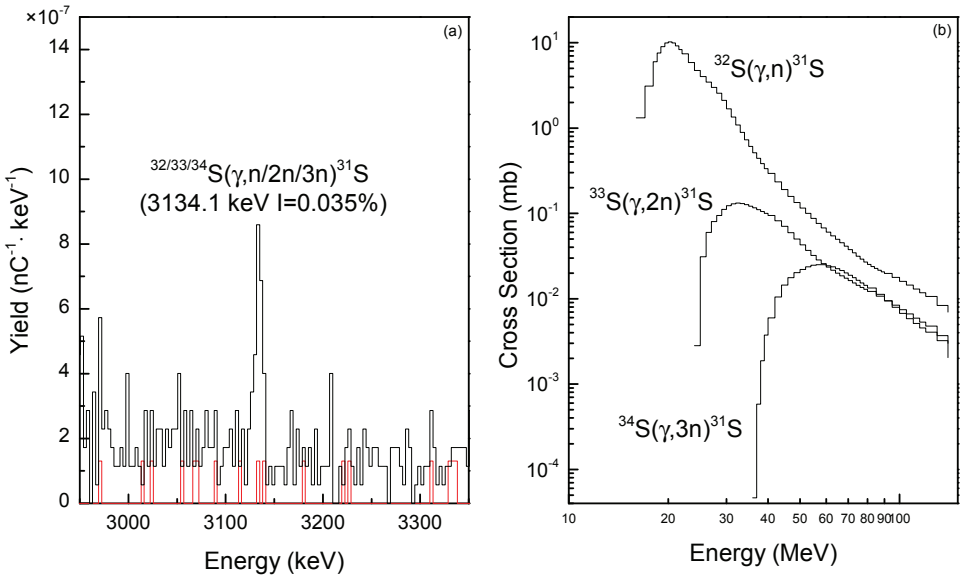

Figure A.2.26: Sulfur (black) energy spectrum with 3134.1 keV photopeak from the decay of ^{31}S observed (a). A no-target inspection (red) is included for comparison. All other parameters match those described in Figure A.2.25. Production cross sections (b) are available from ENDF/B-VII.1 [41].

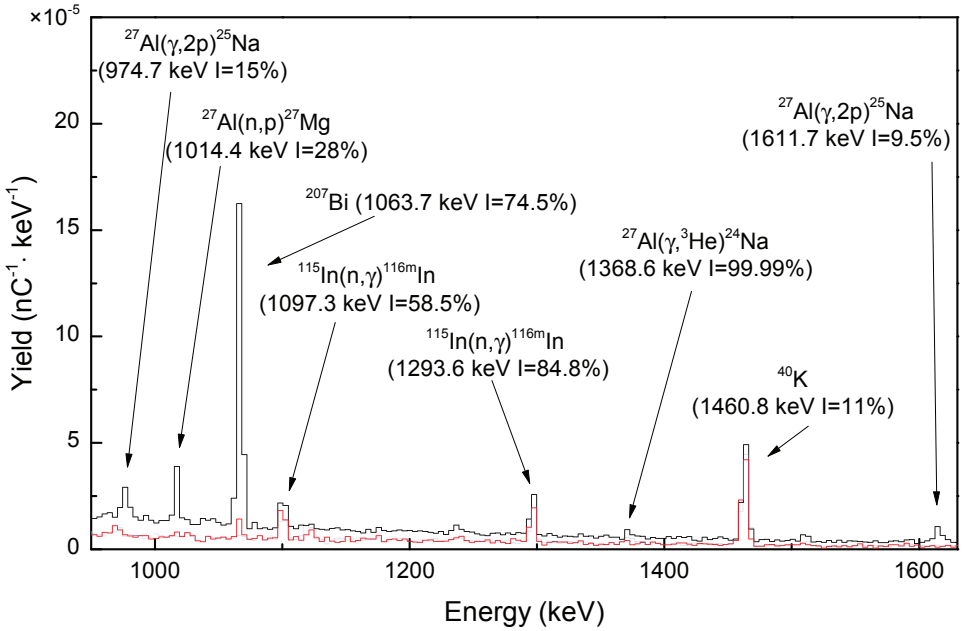

Figure A.2.27: Aluminum (black) energy spectrum showing various decay peaks from ^{24}Na and ^{25}Na. Spectra from no-target active (red) and passive (blue) inspections are also displayed. The charge averaged over both active inspections and 67514 pulses is 46.9 nC produced by electrons generating the 44.75 MeV endpoint energy bremsstrahlung beam. The background peaks shown have been described in various figures throughout this section.

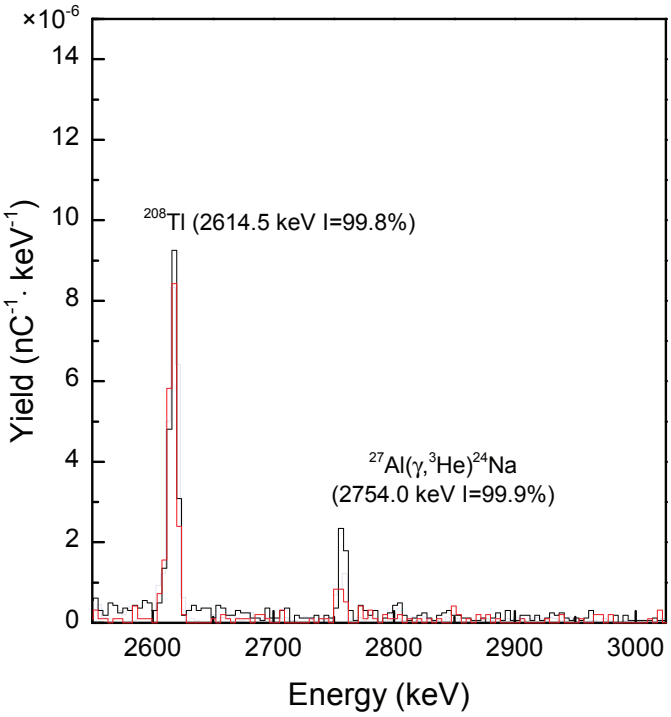

Figure A.2.28: Aluminum (black) energy spectrum with the same accelerator parameters as that described in A.2.27. The spectrum focuses on a higher energy region to show the 2754.0 keV ^{24}Na decay peak resulting from the photodisintegration of ^{27}Al.

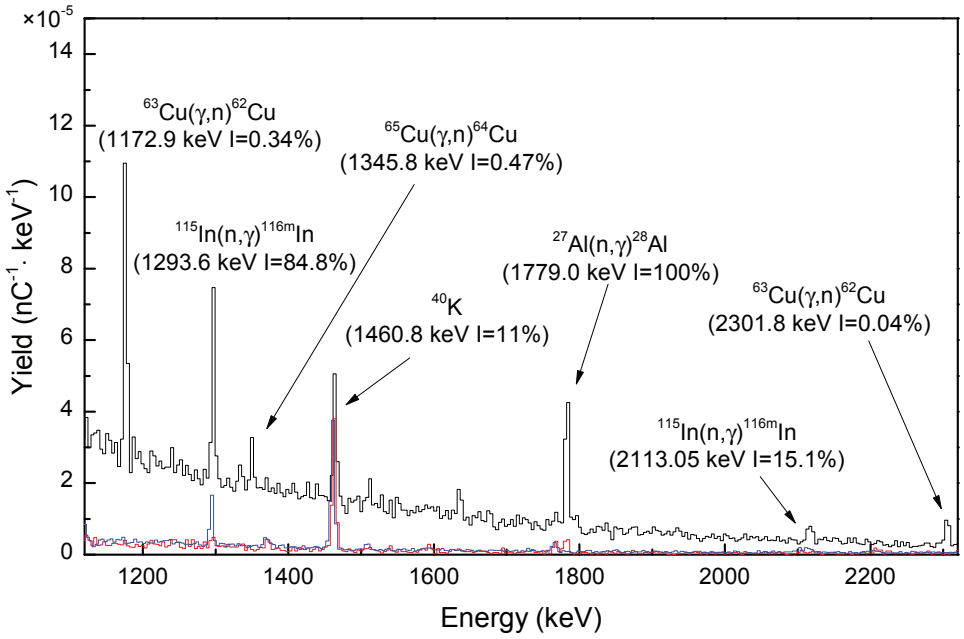

Figure A.2.29: Copper (black), no-target active (red) and passive (blue) energy spectra showing 1172.9 and 2301.8 keV decay peaks from ^{62}Cu initiated by the ^{63}Cu(γ,n) reaction. Accelerator parameters include a charge of 55.9 nC averaged over both active inspections and 29426 pulses. The endpoint energy of the bremsstrahlung beam was 44.75 MeV.

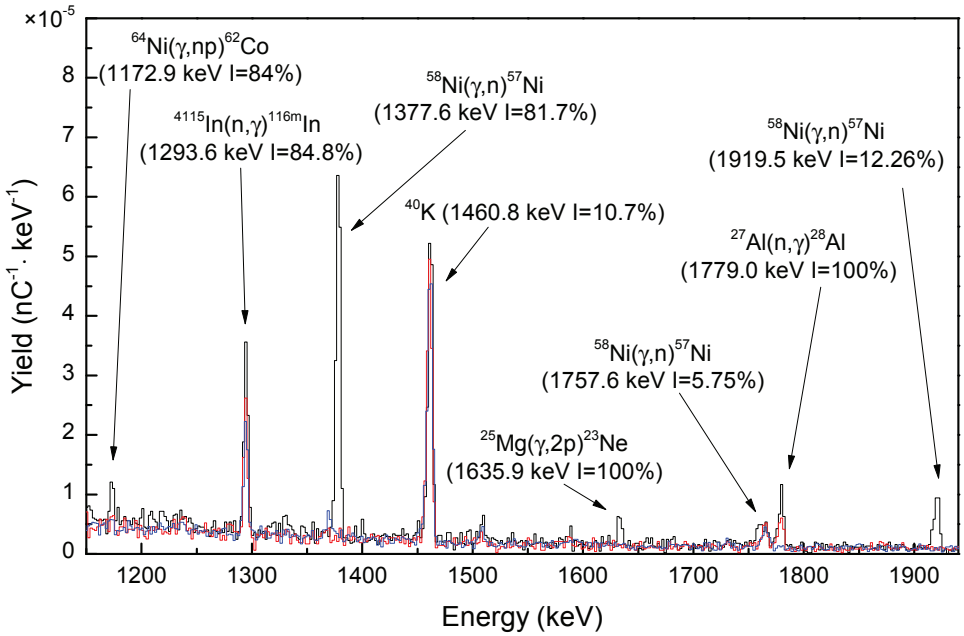

Figure A.2.30: Nickel (black) energy spectrum with 1172.9 keV ^{62}Co decay peak resulting from the photodisintegration of ^{64}Ni. The 1377.6, 1757.6, and 1919.5 keV peaks result from the decay of ^{57}Ni produced from the ^{58}Ni(γ,n) reaction. No-target active (red) and passive (blue) energy spectra are also shown. The accelerator operated at 44.75 MeV producing electrons with an average charge per pulse of 46.8 nC for the active inspections. Objects were irradiated with 48776 pulses. The background peaks shown have been described in various figures throughout this section.

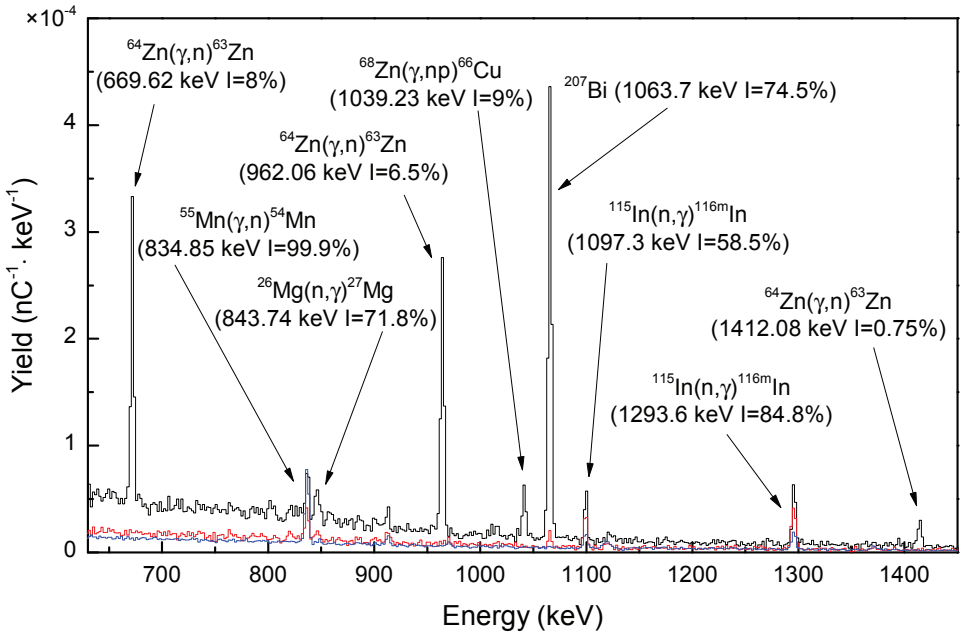

Figure A.2.31: Zinc (black), no-target active (red) and passive (blue) energy spectra displaying 669.6, 962.1, and 1412.1 keV decay peaks from ^{63}Zn generated by the ^{64}Zn(γ,n) reaction. Electrons produced an average charge of 54.6 nC. The accelerator operated at a bremsstrahlung endpoint energy of 44.75 MeV for 22590 pulses. The background peaks shown have been described in various figures throughout this section.

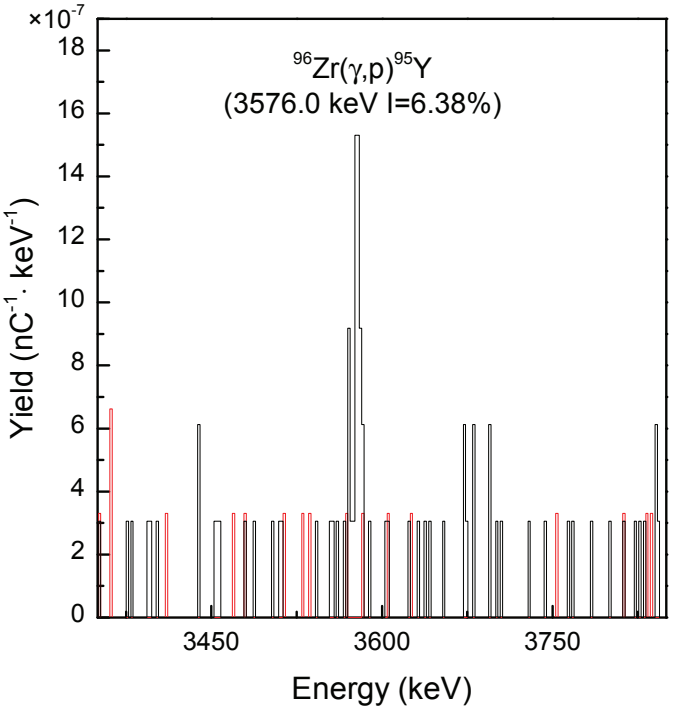

Figure A.2.32: Zirconium (black) energy spectrum with the ^{95}Y 3576.0 keV decay peak shown. Yttrium is produced by the ^{96}Zr(γ,p) reaction. A no-target inspection (red) is shown for comparison. The accelerator operated at 44.75 MeV producing a mean charge per pulse of 55.6 nC averaged over 27870 pulses and both targets.

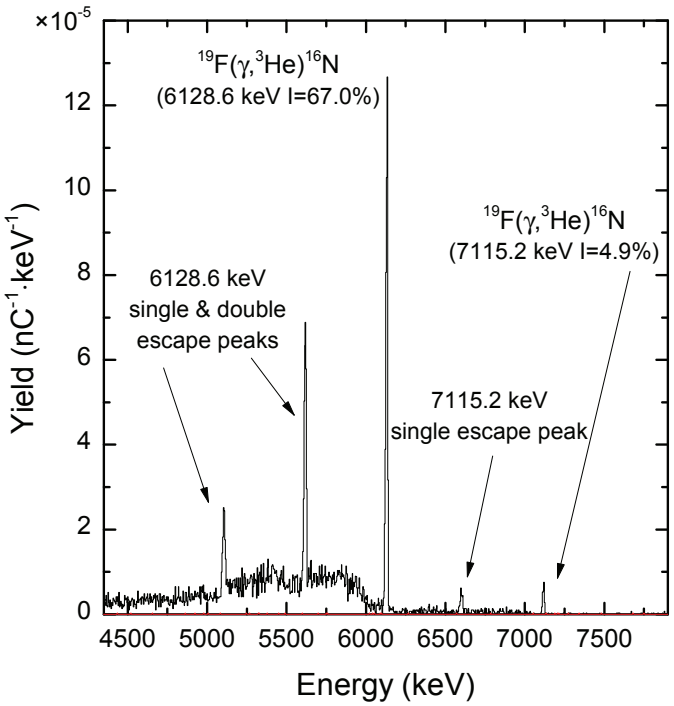

Figure A.2.33: Teflon (black) energy spectrum in comparison to a no-target inspection (red). The decay of ^{16}N from the photodisintegration of ^{19}F evidenced by the 6128.6 and 7115.2 keV photo and escape peaks are shown. Accelerator parameters include a bremsstrahlung endpoint energy of 43 MeV and an average charge per pulse of 71.4 nC averaged over both targets and 10104 pulses.

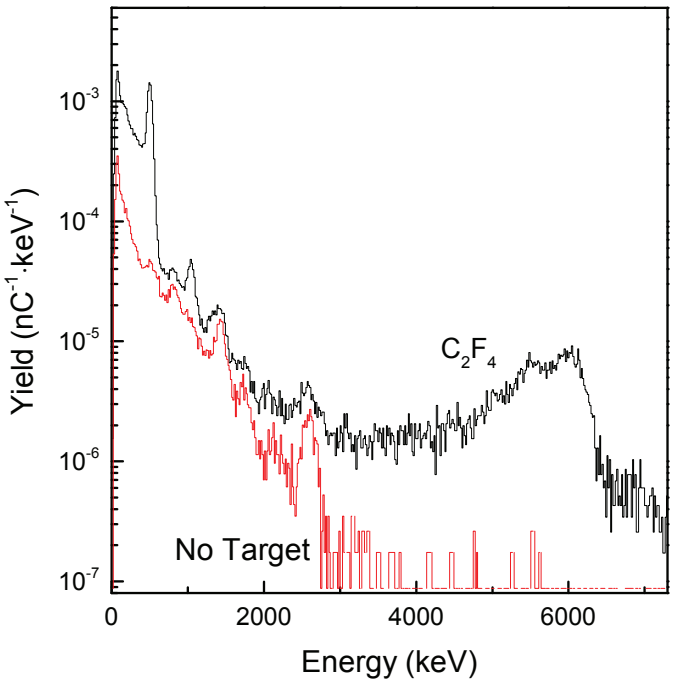

Figure A.2.34: Teflon (black) energy spectrum with a no-target inspection (red) shown for comparison. Accelerator parameters match those described in A.2.33.

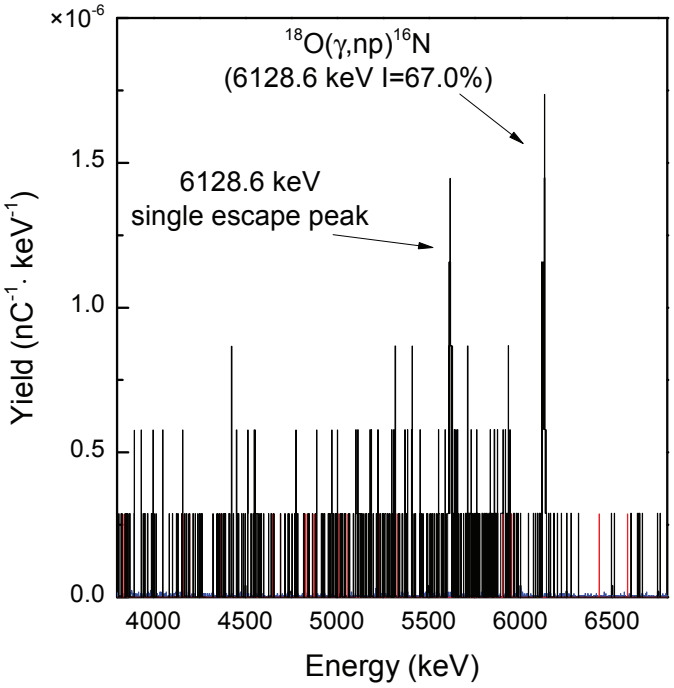

Figure A.2.35: Concrete (black) energy spectrum showing ^{16}N decay peaks resulting from the photodisintegration of ^{18}O. No-target active (red) and passive (blue) energy spectra are also displayed. The accelerator operated at 37.5 MeV producing a mean charge per pulse of 186.1 nC averaged over both active targets and 9053 pulses.

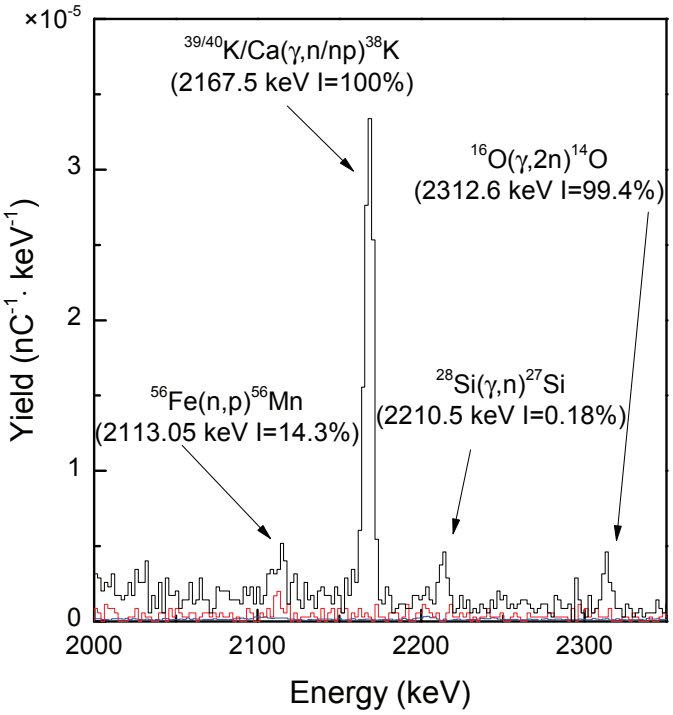

Figure A.2.36: Concrete (black), no-target active (red) and passive (blue) energy spectra displayed. Decay peaks from reactions produced in concrete include ^{39}K(γ,n)^{38}K, ^{40}Ca(γ,np)^{38}K, ^{28}Si(γ,n)^{27}Si, and ^{16}O(γ,2n)^{14}O. Accelerator parameters match those described in A.2.35.

Appendix B

Target Uses

Table B.1: Isotopic Characteristics and Material Uses/Orgins

Parent	**Elem. Abund. Earth's Crust†** (%)	**Elem. Abund. Atmosphere††** (%)	**Isotope Abundance‡** (%)	**Origins/Uses^o**
^{27}Al	8.13	0.00	100	Third most abundant element in earth's crust. Found in cans, foils, kitchen utensils, airplanes, etc.
^{36}Ar	0.00	0.934	0.337	Third most abundant atmospheric gas.
^{38}Ar	0.00	0.934	0.063	Used in arc welding.
^{40}Ar	0.00	0.934	99.6	
^{75}As	0.0005	0.934	100	Used to make poison and insecticides. Also used in transistors.
^{10}B	0.0003	0.00	19.9	Used in pyrotechnics, rockets, nuclear
^{11}B	0.0003	0.00	80.1	reactors, fiberglass, insulation, borax, etc.
^{9}Be	0.0006	0.00	100	Can be used as a neutron source. Used in components of space shuttles.
^{79}Br	0.00016	0.00	50.69	Added to leaded gasolines, used in pho-
		0.00		tography, fumigants, and to purify water.
^{13}C	0.032	0.040	1.10	Sixth most abundant element in universe. Used to make inks, paints, dry cell batteries, in steel production, pencils, jewelry, etc.
^{40}Ca	3.63	0.00	96.941	Fifth most abundant element in earth's
^{46}Ca	3.63	0.00	0.004	crust. Alloyed with other metals.
^{48}Ca	3.63	0.00	0.187	Found in chalk, marble, and limestone. Used in paint, toothpaste antacids, dry wall fertilizer, bones, and teeth.

Continued on next page. † [110],†† [111],‡ [109],^{o} [115, 118]

Table B.1 Observed Reactions Continued

Parent	**Elem. Abund. Earth's Crust†** (%)	**Elem. Abund. Atmosphere††** (%)	**Isotope Abundance‡** (%)	**Origins/Uses^o**
^{35}Cl	0.0314	0.00	75.77	Used as an antiseptic and in industrial
^{37}Cl	0.0314	0.00	24.23	processes. Used to make table salt. Found in seawater.
^{53}Cr	0.020	0.00	9.501	Forms ninth most abundant compound in
^{54}Cr	0.020	0.00	2.365	earth's crust. Plated with other metals. Used as a steel alloy, to fire bricks, etc.
^{63}Cu	0.007	0.00	69.17	Used to make wire, coins, jewelry, etc.
^{19}F	0.030	0.00	100	Used for tooth decay prevention added in water and toothpaste. Used to etch glass, make lenses, etc.
^{54}Fe	5.00	0.00	5.8	Used to make steel. Found in chlorophyll
^{57}Fe	5.00	0.00	2.2	and hemoglobin.
^{58}Fe	5.00	0.00	0.28	
^{69}Ga	0.0015	0.00	60.108	Used as an alloy with other metals, semi-conductor doping, transistors, and lasers.
^{70}Ge	0.0007	0.00	20.84	Used in transistors and electronic devices.
^{73}Ge	0.0007	0.00	7.73	Used in fluorescent lamps and detectors.
^{76}Ge	0.0007	0.00	7.61	
^{39}K	2.59	0.00	93.2581	8th most abundant element in the
^{40}K	2.59	0.00	0.0117	earth's continental crust and 5th
^{41}K	2.59	0.00	6.7302	most abundant in the oceans. Used in fertilizers, soaps, and detergents. Used to make glass.
^{78}Kr	0.00	0.000114	0.65	Found in earth's atmosphere. Used in
^{80}Kr	0.00	0.000114	2.28	high speed photography, fluorescent
^{86}Kr	0.00	0.000114	17.30	light bulbs, and luminous signs.
^{7}Li	0.0065	0.00	92.5	Used in special glasses and ceramics, in metals aircrafts, and in drugs to treat depression.
^{24}Mg	2.09	0.00	78.99	Forms second most abundant compound
^{25}Mg	2.09	0.00	10.00	in earth's crust. Used in antacids,
^{26}Mg	2.09	0.00	11.01	insulating materials, cements, Epsom salt, paints, etc.
^{92}Mo	0.0015	0.00	14.84	Used to make electrical filaments, aircraft
^{94}Mo	0.0015	0.00	9.25	parts, refining petroleum, and for making steel.
^{14}N	0.0046	78.08	99.634	Fifth most abundant element in the
^{15}N	0.0046	78.08	0.366	universe. Used in fertilizers, explosives, in welding, etc.
^{23}Na	2.83	0.00	100	Used in street lights and as a compound in table salt, baking soda, borax, etc.

Continued on next page. † [110],†† [111],‡ [109],^{o} [115, 118]

Table B.1 Observed Reactions Continued

Parent	**Elem. Abund. Earth's Crust†** (%)	**Elem. Abund. Atmosphere††** (%)	**Isotope Abundance‡** (%)	**Origins/Uses^o**
^{21}Ne	0.00	0.001818	0.27	Used in advertising signs, to make lasers,
^{22}Ne	0.00	0.001818	9.25	as a cryogenic refrigerant, etc.
^{58}Ni	0.008	0.00	68.0769	Used as an alloy with other metals. Used
^{64}Ni	0.008	0.00	0.9256	to make coins, batteries, machine parts,
				pipes, magnets, etc.
^{16}O	46.60	20.95	99.762	Third most abundant element in the
^{17}O	46.60	20.95	0.038	universe. Makes 9/10ths the mass of
^{18}O	46.60	20.95	0.2	water. Used in steel production, welding,
				rocket fuel, etc.
^{31}P	0.118	0.00	100	Used to make fireworks, smoke bombs,
				pesticides, and soft drinks.
^{207}Pb	0.0016	0.00	22.1	Used to shield against γ-ray radiation.
				Used in the production of batteries.
^{102}Pd	1E-6	0.00	1.02	Used in watches, surgical instruments,
				electrical contacts, and carbon monoxide
				detectors. Found in paint.
^{85}Rb	0.031	0.00	72.17	Used in vacuum tubes and the
				manufacture of photocells and glasses.
^{96}Ru	1E-9	0.00	5.54	Used as an alloying agent as well as
				in jewelry and electrical contacts.
^{32}S	0.052	0.00	94.93	Used to make fertilizer, batteries, in
^{33}S	0.052	0.00	0.76	insecticides, to manufacture gunpowder,
^{34}S	0.052	0.00	4.29	etc.
^{36}S	0.052	0.00	0.02	
^{45}Sc	0.0005	0.00	100	Used in baseball bats, bicycle frames, and
				high intensity lights.
^{74}Se	9E-6	0.00	0.89	Found in electric eyes, photo cells,
^{80}Se	9E-6	0.00	49.61	cameras and copiers, glasses, and as an
^{82}Se	9E-6	0.00	8.73	additive to stainless steel.
^{29}Si-	27.72	0.00	4.67	Most abundant compound (SiO_2) in
				earth's crust. Used in solid-state
				electronic devices.
^{84}Sr	0.030	0.00	0.56	Used to manufacture TV tubes, to make
				magnets, and refine zinc. It is a
				product of nuclear explosions.
^{46}Ti	0.44	0.00	8.25	Used to make airplanes, missiles, rockets,
				biological implants, smoke screens, etc.
^{89}Y	0.0028	0.00	100	Used in color televisions, microwave filters,
				jewelry, etc.
^{64}Zn	0.0132	0.00	48.63	Used in alloys such as brass, in coins,
				musical instruments, hardware, pipes,

Continued on next page. † [110],†† [111],‡ [109],^{o} [115, 118]

Table B.1 Observed Reactions Continued

Parent	**Elem. Abund. Earth's Crust†** (%)	**Elem. Abund. Atmosphere††** (%)	**Isotope Abundance‡** (%)	**Origins/Uses**^{o}
				cosmetics, plastics, etc.
^{94}Zr	0.022	0.00	17.38	Used in nuclear reactors, jewelry, high
^{96}Zr	0.022	0.00	2.80	temperature furnaces, and lotions.